ANTIMONIDE NANOWIRES FOR MULTISPECTRAL INFRARED PHOTODETECTION

ANTIMONIDE NANOWIRES FOR MULTISPECTRAL INFRARED PHOTODETECTION

By MITCHELL THOMAS ROBSON, B.Eng.

A Thesis Submitted to the School of Graduate Studies in Partial Fulfillment of the Requirements for the Degree Doctor of Philosophy

McMaster University

© Copyright by Mitchell Thomas Robson, October 2018

DOCTOR OF PHILOSOPHY (2018) McMaster University

(Engineering Physics) Hamilton, Ontario

TITLE: Antimonide Nanowires for Multispectral Infrared Photodetection

AUTHOR: Mitchell Thomas Robson, B.Eng. (Carleton University)

SUPERVISOR: Dr. R.R. LaPierre

NUMBER OF PAGES: xx, 196

Abstract

Multispectral capabilities of nanowires (NWs) were explored for InAs and InAsSb NWs on Si(111) substrates. NWs were grown with the vapour-solid (VS) growth mode in a molecular beam epitaxy (MBE) system using an oxide template to control positions and diameters. Early attempts to integrate InSb NWs and silicon substrates proved unsuccessful. Instead studies of InAs NWs on silicon, and eventually InAsSb/InAs NWs on silicon were completed to achieve large-diameter, infrared (IR) sensitive photodetectors.

InAs NWs were grown on silicon substrates to study their morphology characteristics and vertical NW yield. The five different growth modes explored were (1) Au-assisted vapour-liquid-solid (VLS), (2) positioned Au-assisted, (3) vapour solid, (4) positioned Au-assisted VLS using a patterned oxide mask (VLS-SAE), and (5) selective area epitaxy (SAE) using a patterned oxide mask. Optimal temperature and V/III flux ratios for achieving a high vertical yield were found for the SAE growth mode.

Further understanding of the InAs SAE growth mode was gained through modeling of various oxide hole filling scenarios. Each scenario was defined by the arrival rates of the group III and group V materials to the holes. A parameter space is discussed for the growth of high yield InAs NWs, dependent on the V/III flux ratio and temperature of growth.

Large diameter InAsSb NWs for IR absorptance were grown on silicon using a high yield InAs stem. Several NW array diameters were grown simultaneously on the same substrate to measure multispectral photodetection. Diameters were controlled by NW spacing. Fourier transform IR (FTIR) spectroscopy was used to measure absorptance in the NWs. NW diameters spanned 440 – 520 nm which resulted in enhanced absorptance in the short-wave IR region. Simulations of the HE_{11} resonances of the NW arrays were performed and compared with the FTIR measurements. Initial electrical measurements demonstrated a diameter-dependent photocurrent.

Acknowledgments

First, I would like to express my sincere gratitude to my supervisor Dr. Ray LaPierre, who's unending support and knowledge helped me understand what it means to be a good researcher, leader, and person. His early and continued trust in my capabilities was beyond encouraging. I would also like to thank my committee members, Dr. Kitai, Dr. Preston, and Dr. Thompson for their guidance and challenging questions throughout my degree.

I am grateful to all the members of the LaPierre group, past and present, who helped me with my research. In the beginning Andrew Chia, Chris Haapamaki, and Sandra Gibson taught me all the skills I needed to start a successful research project. I especially want to thank Jonathan Boulanger and Paul Kuyanov for the many hours of training, discussions, and TEM work that helped move my research forward. I would also like to thank Aziz Rahman, Brendan Wood, Paige Wilson, Simon McNamee, and Nebile Isik for all the helpful discussions.

This work would not have been possible without help from some outstanding technical staff. In the CEDT, I would like to thank Shahram Tavakoli and Doris Stevanovic for all their training and help with our instrumentation. I am thankful for their patience with my initial learning curve and their trust later in my degree. In the CCEM, I would like to thank Chris Butcher, and Travis Casagrande for characterization help. I am also grateful to Alex Tsukernik of the Toronto Nanofabrication Centre for his kindness in helping me design, and redesign EBL

patterns. Thanks to Marcia Reid of the Faculty of Health Sciences for expertly performing ultramicrotome on unusually difficult (and valuable!) samples. I would also like to thank the members of the Department of Engineering Physics: Marilyn, Nicole, Alexa, and Robert.

Several collaborators have also supported my research. I would like to acknowledge Jonathan Baugh, Simon Watkins, Vladimir Dubrovskii, and each of their research groups. I am also thankful to all the funding agencies that found my research interesting. Specifically, the Department of Engineering Physics, the Ontario Graduate Scholarships, the Natural Science and Engineering Research Council of Canada, Lockheed Martin Canada, and Teledyne DALSA Inc.

Finally, I would like to thank my family and friends who have each provided unwavering support over these years. I am especially grateful to my parents who have always been behind me in whatever I chose to do. Even in the most difficult situations, they have provided me a positive perspective and good advice. And a special thanks to Sabrina for being there for me through all the highs and the lows of research. This thesis would not be possible without her support.

I dedicate this work to my family and friends

Table of Contents

Abstract......iii

Acknowledgments......v

List of Figures......xiii

List of Tables......xx

1 Background......1

1.1 Introduction......1

1.2 Nanowire Growth......3

1.2.1 Fundamentals of Growth......3

1.2.2 Vapour-Solid (VS)......10

1.2.3 Selected Area Epitaxy (SAE)......12

1.2.4 Vapour-Liquid-Solid (VLS)......14

1.2.5 Crystal Structure......16

1.2.6 Antimony (Sb) Growth Considerations......20

1.3 Nanowire Absorption......21

1.3.1 Radial Resonance......22

1.3.2 Evanescent Coupling......26

1.3.3 Absorptance in the NW......27

1.4 Nanowire Infrared Detectors......28

1.4.1 Mercury Cadmium Telluride (MCT) Detectors......30

1.4.2 InSb Detectors 32

1.4.3 Microbolometers 33

1.4.4 InAs(Sb) Nanowire photodetectors 34

1.5 Thesis Overview 38

2 Characterization Methods 40

2.1 Electron Microscopy 40

2.1.1 Principles 40

2.1.2 Scanning Electron Microscopy (SEM) 42

2.1.3 Transmission Electron Microscopy (TEM) 44

2.1.4 TEM Sample Preparation 46

2.2 Atomic Force Microscopy (AFM) 49

2.3 Variable Angle Spectroscopic Ellipsometry (VASE) 53

2.4 Fourier Transform Infrared Spectroscopy (FTIR) 56

2.5 Raman Spectroscopy 61

2.6 Current-Voltage (I-V) Characterization 63

3 Fabrication Methods 65

3.1 Pre-growth Preparation 65

3.1.1 Chemical Vapour Deposition (CVD) 66

3.1.2 Electron Beam Lithography (EBL) 66

3.1.3 Reactive Ion Etching (RIE) 70

3.1.4 Buffered Hydrofluoric Acid (BHF) 74

3.2 Growth in Gas Source Molecular Beam Epitaxy (GS-MBE) 74

3.3 Post-growth Device Fabrication 77

3.3.1 Polymer Spin-coat 78

3.3.2 RIE Etchback 79

3.3.3 Photolithography 79

3.3.4 Sputter Deposition 80

3.3.5 Electron Beam Evaporation 81

3.3.6 Rapid Thermal Annealing (RTA) 81

3.4 RIE Etchback Roughness 81

4 InAs Growth Modes on Silicon 87

4.1 Summary 87

4.2 Introduction 88

4.3 Experimental Details 90

4.4 Results and Discussion 94

4.4.1 Au-Assisted VLS Growth 94

4.4.2 Positioned-Au-Assisted VLS Growth 98

4.4.3 Catalyst-Free VS Growth 99

4.4.4 Au-Assisted-VLS-SAE 104

4.4.5 SAE Growth 108

4.5 Conclusions 115

5 Conditions for High Yield of InAs NWs on Silicon 117

5.1 Summary 117

5.2 Introduction 117

5.3 Experimental Details 119

5.4 Results 120

5.5 Model and Discussion 123

5.6 Conclusion 131

6 Multispectral Absorptance in InAsSb Arrays 132

6.1 Summary 132

6.2 Introduction 133

6.3 Experimental Details 135

6.4 Results and Discussion 139

6.4.1 Fractional Flux Study 139

6.4.2 Core-Shell Growths 147

6.4.3 Absorptance 154

6.4.4 Current-Voltage 159

6.5 Conclusions 166

7 Conclusions and Future Work 168

7.1 Thesis Summary 168

7.2 Future Work 171

8 References 176

9 Appendix 192

9.1 VASE BCB Model 192

9.2 FF Calculations 192

List of Figures

Figure 1.1: Process of material deposition in MBE. Vapour phase atoms adsorb, diffuse, and then nucleate to grow layers, or else desorb. 4

Figure 1.2: One-dimensional surface diffusion processes beginning with adsorption and ending with either desorption or incorporation. Incorporation occurs when an empty lattice site is filled with a diffusing adatom. Black spheres indicate original lattice atoms. Blue spheres indicate diffusing or new lattice atoms. 5

Figure 1.3: Nucleation of clusters. a) Adatoms contribute to a cluster that has surpassed its critical radius. b) Surface energies of a cluster in cross-section. γ, γi, γs and χ are the surface energies of the top surface of the cluster, the interface between the cluster and the growth surface, the growth surface itself, and the formation energy of the edge. 8

Figure 1.4: Three main crystal growth modes in MBE. Layer-by-layer: each layer is completed before nucleating the next. Island: three-dimensional islands are formed leaving the surface mostly uncovered. Stranski-Krastanov (SK): combined layer-by-layer and subsequent island growth. 9

Figure 1.5: VS growth progression showing a) Nucleation of multi-facetted nucleus, b) extinction of high index facets, and c) simultaneous axial and radial growth of primary facets depending on growth parameters. Parasitic film growth is also indicated. 11

Figure 1.6: SAE growth progression. a) Growth impeding mask controls the nucleation position of NWs either by diffusion or desorption of growth species. b) NWs nucleate epitaxially in holes in the mask. c) Growth continues as VS. Shadowing becomes important as NWs grow taller. 13

Figure 1.7: VLS growth progression. a) Seed particles are deposited onto a substrate using various in-situ and ex-situ methods. b) Growth species are supplied to the substrate surface and are adsorbed by the seed particles. c) Supersaturation of the seed particle occurs, and a solid phase is formed beneath the liquid droplet. Repetition of this process creates a long, thin crystal (NW). 15

Figure 1.8: Atomic stacking in the wurtzite (WZ) and zincblende (ZB) crystal phases for III-Vs. a) Side profile with indicated A, B, and C layers. Dotted lines are a guide for the eye. b) Top down view in the [-1-1-1] direction with indicated lateral positions of the A, B, C layers. Grey triangles in b) highlight the position of the lattice drawn in a). 18

Figure 1.9: Electric field patterns of cylindrical waveguiding modes in cross-section as compared to a polarized incident plane wave. a) Incident plane wave propagating in the z direction. b) Geometric and optical parameters of the waveguide. Radial mode resonance electric field patterns for c) HE_{11}, d) HE_{12}, e) TE_{01}, and f) TM_{01}. 24

Figure 1.10: Dual band MCT photodetector architectures. a) bias-selectable n-p-n and b) simultaneous homojunction structure [6]. Metal interconnects and indium bump bonds are shown in black. Electrical isolation is shown in yellow. Long-wave (LW) and short-wave (SW) absorption regions are indicated.. 31

Figure 1.11: Simulated absorptance of InSb NWs with indicated diameter (D), period (P), and length (L). Dimensions were chosen for ~80% absorptance. Thin film of InSb is shown for comparison. Adapted from [46]. 35

Figure 2.1: Interactions of a high energy beam of electrons within a semiconductor sample. Interactions below the sample only occur when it is sufficiently thin (TEM). Interactions above mostly pertain to bulk samples in SEM. 42

Figure 2.2: Process for creating a NW array cross-section using a focussed ion beam system. a) Area of interest is selected, b) a conformal carbon layer is deposited in situ, c) a platinum capping layer is deposited in situ, d) trenches are milled around the NWs, e) the lamella is attached to a TEM post using a platinum weld, f) the lamella is thinned to ~100 nm for TEM analysis. Images taken by Travis Casagrande from the CCEM. 48

Figure 2.3: Ultramicrotome horizontal cross-section of NWs in BF TEM. a) View including most of a NW array with an evident angular cut. b) Close up of single NW. 49

Figure 2.4: AFM tapping mode operation. Laser is aligned through a prism to the back of the cantilever. Reflected laser spot is captured in an aligned photodiode.. 52

Figure 2.5: Ellipsometer with a rotating analyzer. Incident light is monochromatic and linearly polarized with a component in both the s- and p-planes. Reflected light is generally elliptically polarized. 55

Figure 2.6: FTIR Michelson interferometer beam path with broadband source. Interferogram incident on the sample is converted to a spectrum with a Fourier transform. Mirror position is measured directly with HeNe laser. 58

Figure 2.7: Hyperion 3000 beam path for measuring reflectance and transmittance. IR input from the interferometer in a Vertex 70v

system. IR reflectance and transmittance paths are indicated by R and T respectively. Alternative mirror positions are indicated with dotted lines. 60

Figure 2.8: Renishaw confocal micro-Raman spectrometer setup. Excitation (laser) beam path is indicated in red and detection (Raman) beam path is in green. 63

Figure 3.1: Process flow for NW growth preparation. Beginning with an epi-ready wafer (grey), a) a CVD oxide (blue) is grown on top of the wafer, and b) an EBL pattern (red) defines the NW positions. c) RIE etches partway through the oxide in the EBL holes. d) Resist is lifted off and remaining oxide in the holes is removed with BHF... 66

Figure 3.2: Top view of the EBL pattern used in this thesis. Items in black represent real features in the design. Red indicates annotations. Grey represents the cleaved pie piece with a thin CVD oxide. Black squares are NW pads with triangular arrays of patterned dots (Top inset). A magnified view of the compressed region is shown in the bottom inset with indicated diameter and period. 69

Figure 3.3: Cross-sectional view of RIE reactions. a) Physical sputtering, b) chemical etching, c) ion enhanced chemical etching, and d) inhibitor driven ion enhanced etching. Etched sample is shown in grey and an etch mask is in light blue. Black spheres are ions, blue are radicals, and red are volatile products. 72

Figure 3.4: Illustration of main GS-MBE components for the system at McMaster University. Three-stage antimony effusion cell is indicated with i) thermal cracker stage, ii) heated needle valve, and iii) reservoir. 76

Figure 3.5: Device fabrication process for NW arrays. a) Extracted NWs with indicated oxide layer are imaged in SEM, b) BCB polymer is spin-coated onto the sample, c) RIE etches the BCB to reveal NW tips, d) photolithography for transparent contacts before development, e) sputter deposition of transparent contacts, f) photolithography for opaque contacts after development, g) electron beam deposition of opaque contacts, and h) sputter deposition of Al back contacts followed by RTA. 78

Figure 3.6: SEM images of etched BCB using a) Recipe 2 (R_a = 18 nm) and b) Recipe 7 (R_a = 3 nm). Images are tilted to 30 degrees and scale bars indicate 200 nm. Samples are covered by 10 nm of e-beam deposited nickel. 86

Figure 4.1: Cross-sectional schematic of a) oxide-free Si substrate and b) Si substrates with CVD-deposited silicon oxide as they are prior to loading into the MBE. Growth methods/regions include i) Au-assisted,

ii) positioned-Au-assisted, iii) catalyst-free, iv) Au-assisted-SAE, and v) SAE.. 91

Figure 4.2: Au-assisted NWs (Figure 4.1a(i)) grown at 330 ˚C. (a) SEM image of NWs. Scale bar is 200 nm. Inset shows Au droplet at the NW tip with scale bar of 50 nm. (b) Length versus diameter of NWs. (c) Distribution of NW diameters for the indicated growth temperatures. 95

Figure 4.3: SEM image of NWs grown at 330 ˚C by positioned Au-assisted VLS growth (Figure 4.1a(ii)). Scale bar is 200 nm. 99

Figure 4.4: SEM images for VS NWs (Figure 4.1a(iii)) grown with a V/III flux ratio of 4 and temperature of a) 330 ˚C, b) 350 ˚C, c) 380 ˚C and d) 400 ˚C. Scale bars are 200 nm. Inset in c) shows a TEM image of the tip of a wire grown at 380 ˚C with a 10 nm scale bar. 100

Figure 4.5: Morphological trends of VS NWs. a) Length and diameter versus temperature for VS NWs at a V/III flux ratio of 4. b) Length and diameter versus V/III flux ratio at a temperature of 380 ˚C. Diameter data is indicated by blue circles, length by black triangles. Dashed lines are visual guides only. Representative error bars are indicated. 103

Figure 4.6: SEM images of patterned Au-assisted NWs on oxide-covered substrates (Au-assisted-VLS-SAE; Figure 4.1b(iv)) grown with a V/III flux ratio of 4 and temperature of (a) 400 ˚C, (b) 420 ˚C, (c) 440 ˚C and (d) 460 ˚C. Scale bars are 200 nm. e) Length and diameter versus period for NWs grown at 440 ˚C. Dashed lines are visual guides only. Representative error bars are indicated. 105

Figure 4.7: SEM images of Au-assisted-SAE NWs grown with a V/III flux ratio of a) 2, b) 3, c) 4 and d) 10 at a temperature of 440 ˚C. Scale bars are 300 nm. e) NW length and diameter as a function of V/III flux ratio. Dashed lines are visual guides only. Representative error bars are indicated. 108

Figure 4.8: SEM images for SAE NWs (Figure 4.1b(v)) with a V/III flux ratio of 4 and a temperature of a) 400 ˚C, b) 420 ˚C, c) 440 ˚C and d) 460 ˚C. Scale bars are 300 nm. Inset SEM image in a) shows multiple NWs growing from a single oxide hole with 100 nm scale bar. Inset in c) shows a TEM image of a NW tip grown at 440 ˚C with a 10 nm scale bar. Reproduced with permission from Ref. [102]. 110

Figure 4.9: SAE NWs grown at 440 ˚C with V/III flux ratio of a) 2, b) 3, c) 4, d) 6 and e) 10. Scale bars are 200 nm. Inset in b) shows an SEM image of a crystallite with a droplet remaining on top. Scale bar is 50 nm. Reproduced with permission from Ref. [102]. 112

Figure 4.10: Length and diameter of vertical SAE NWs versus period for a V/III flux ratio of a) 4, b) 6, and c) 10. Flux ratios less than 4 are excluded due to

a lack of vertical NWs. Dashed lines are visual guides only. Horizontal dash-dotted lines represent the length due to direct impingement of As. Representative error bars are indicated. 113

Figure 5.1: SEM images for SAE NWs with a V/III flux ratio of 4 and a growth temperature of (a) 400 ˚C, (b) 420 ˚C, (c) 440 ˚C and (d) 460 ˚C. Scale bars are 300 nm. Reproduced with permission from [101]............ 121

Figure 5.2: SEM images for SAE InAs NWs grown at 440 ˚C with V/III flux ratio of (a) 2, (b) 3, (c) 4, (d) 6 and (e) 10. Scale bars are 200 nm. Inset in (b) shows an SEM image of a crystallite with a droplet remaining on top. Scale bar is 50 nm. 122

Figure 5.3: Illustration of possible scenarios of filling the holes: (a) excessive group V flux producing III-V crystallite; (b) excessive group III flux producing large metal droplet and irregular crystallites at the periphery of the hole, and (c) balanced group V and III fluxes producing a small droplet and one NW per hole. 124

Figure 5.4: Growth temperature – V/III flux ratio map for the experimental geometry of MBE-grown SAE InAs NWs on Si. Red lines correspond to the In collection limited by the diffusion length of In adatoms and magenta lines show the period limitation (solid line: A =360 nm, dash-dotted line: A =440 nm; for larger periods this limitation becomes ineffective). NW (NW) nucleation region is within the domain restricted by the curves. Symbols show the experimental points with the measured yields of vertical InAs NWs. 129

Figure 6.1: Morphological aspects of NW arrays. (a) Schematic of NWs in a triangular lattice with hexagonal cross-sections and the diameter (D), period (P), and length (L) indicated, (b) plan view SEM of 1000 nm period array of holes in the Si oxide, (c) droplets and crystallites on the oxide away from the NW arrays, (d) 30° tilted SEM of a core-shell NW from 1000 nm period array, and (e) trends of diameter and length versus array period. Error bars represent standard deviations....... 137

Figure 6.2: Fractional flux growths. 30-degree tilted SEM images of InAsSb NWs with a fractional flux of (a) 5%, (b) 10%, (c) 14%, and (d) 23%. Scale bars are 200 nm. (e) Length and diameter versus fractional flux. (a) – (c) are shown with a period of 360 nm and (d) is shown with a period of 520 nm. 142

Figure 6.3: Raman shifts for NW arrays of (a) InAs, and InAsSb with FF of (b) 5%, (c) 10%, (d) 14%, and (e) 23%. Experimental Raman data is given by black dots, and the solid curves are fitted Lorentzian profiles such that the three (or two) peaks add up to match the experimental data. Green curve is the InSb-like TO+LO mode, red is InAs TO mode, and blue is InAs LO mode. 145

Figure 6.4: LO and TO peak position shifts with Sb content in InAsSb NW arrays. Equations from reference [187] are shown in light grey, experimental data from this study are shown in black. Error bars for composition are from the EDX measurement error (1%). Raman shift error bars are estimated from the fits. 146

Figure 6.5: Core growth of InAsSb without subsequent shell growth. (a) 30-degree tilted SEM image of the core NW array at a period of 360 nm (scale bar is 200 nm), (b) BF-TEM of a NW from the 1000 nm period emphasizing the stacking faults (twins) in the crystal structure, and (c) accompanying selective area electron diffraction (SAD) pattern.... 148

Figure 6.6: TEM analysis of NW arrays. (a) – (f) Vertical FIB-cut NWs from each of the 1000, 1500, 2000, and 3000 nm arrays with indicated selected area electron diffraction (SAD) pattern and high-resolution TEM of the substrate-NW interface. Scale bars indicate 200 nm. (g) – (j) HAADF-STEM from microtome horizontal cross-section of a NW from the 1000 nm array with point scans, EDX area map of As and Sb, line scan section of As area map, and line scan section of Sb area map, respectively. 150

Figure 6.7: High resolution TEM images of an InAsSb NW (FF = 14%). (a) along the top 150 nm of the NW, (b) SAD of the indicated region, and (c) higher magnification at the base of the NW. Twin planes (TP) and stacking faults (SF) are identified in (a) by blue and purple arrows respectively. Ordered regions are shown in (c). 153

Figure 6.8: Absorptance spectra of InAsSb NW arrays for the indicated periods (black: 1000 nm, red: 1500 nm, green: 2000 nm, blue: 3000 nm). Solid lines are experimental data, dashed lines are simulated results, and dash-dot lines are experimentally measured background absorptance near the NW arrays, which includes the effect of droplets, crystallites, and the silicon substrate. Experimentally measured silicon substrate absorptance (grey curve in each plot) shows negligible absorptance. Insets are hexagonal NW cross-sections with indicated diameters in nm. Corresponding tilted SEM images are shown below each absorptance curve... 155

Figure 6.9: (a) E_x, (b) E_y, (c) E_z, (d) H_x, (e) H_y, and (f) H_z field components in simulated semi-infinite InAsSb NW array at a wavelength of 2050 nm for period of 1000 nm and diameter of 440 nm. The E- and H-field patterns correspond to that of the HE_{11} mode. The E- and H-field component magnitudes are in units of V/m and A/m. 157

Figure 6.10: Solar photoresponse (green) of each NW pad relative to dark (black). Dose labels for the arrays are giving by D1, D2, D3, D4, and D5. The

period is indicated at the top. Blue squares signify a shorted device and red squares signify a responsive device. 161

Figure 6.11: Photoresponse of InAs NW arrays. a) IV measurements for a NW with average diameter of 120 nm, illuminated with the indicated wavelength. b) V_{oc} shift vs wavelength for 90 nm and 120 nm diameter NW arrays. Plots courtesy of Baugh Group. 164

Figure 6.12: Single InAsSb NW contacting in SEM. a) 52° tilted SEM (view of a single NW contacted by a tungsten nanoprobe. b) IV measurements of NWs with indicated diameters. Image and plot courtesy of Watkins Group. 166

Figure 7.1: RIE etched InSb (100) wafers with 600 nm diameters and 2000 nm period using a) recipe 1 and b) recipe 2. 174

Figure 9.1: Nominal parameters for modeling BCB thickness in VASE. a) parameters for the biaxial Cauchy film and b) Psi and Delta for a thick (1.5 μm) BCB layer in the 400 – 800 nm wavelength range. 192

Figure 9.2: Plot of BEP and flow rate vs FF for extracting parameters for InAsSb growth in MBE. 196

List of Tables

Table 1.1: IR wavelength ranges and corresponding black body temperature peaks 30

Table 2.1: Typical AFM parameters used to measure small surface deviations. . 53

Table 3.1: Diameter labels with corresponding EBL parameters and hole diameters. 70

Table 3.2: RIE recipe alterations for improved BCB roughness. Stage 1 of the project. 84

Table 3.3: RIE recipe alterations for improved BCB roughness. Stage 2 of the project. 85

Table 6.1: Parameter variation in the four FF growths shown in Figure 6.2. 140

Table 6.2: Quantified Raman analysis of InAsSb NWs with all TO and LO shifts and their corresponding compositions. 147

Table 7.1: Recipes for ICP-RIE etching InSb (100) NWs 173

1 Background

1.1 Introduction

The feature size of semiconductor-based devices is halved every eighteen months, while improving or maintaining the same performance. This pressure has led the industry to move away from conventional two-dimensional architectures and into nanoscale three-dimensional constructions (e.g. finFETs). III-V materials may also replace silicon (Si) due their superior electrical and optical properties.

One such structure is the III-V nanowire (NW). A NW is a high aspect ratio crystalline column with dimensions on the nanoscale. NWs were first fabricated in 1964 by Wagner and Ellis [1] following the vapour-liquid-solid (VLS) growth mechanism. Other mechanisms include vapour-solid (VS), and selected area epitaxy (SAE), which is an extension of VS. All three of these mechanisms belong to the bottom-up fabrication approach, often referred to as "growth". Growth of NWs has been achieved in many epitaxial deposition systems including molecular beam epitaxy (MBE) [2], chemical vapour deposition (CVD) [3], chemical beam epitaxy (CBE) [4], metal organic chemical vapour deposition (MOCVD) [5], and laser ablation [6]. NWs have been fabricated using a wide range of semiconducting materials such as group IV's (Si and Ge [6,7]), III-V's in all combinations (Al, Ga, In, and P, As, Sb [8–15]), and nitrides [3]. It is also possible to fabricate NWs using the top-down (etching) approach. Typically, NWs are etched by reactive ion etching

(RIE) but anisotropic wet etching and metal assisted etching (MAE) have been demonstrated as well [16].

To date, only a few semiconductor NW products have been commercialized, mostly with applications in micro/nano-light emitting diode (LED) displays. Many other NW products are still in an active research phase including photodetectors [17], solar cells [18], transistors [19], lasers [20], resonant tunneling diodes (RTDs) [21], and high electron mobility transistors (HEMTs) [22]. These products may be enhanced by the unique advantages of NWs. NWs can often overcome material lattice mismatch due to their high surface-to-volume ratio. They also offer enhanced absorption capabilities over thin films and act naturally as antireflection coatings. Finally, NWs can construct unique electrical pathways for electron-hole pairs (EHPs). Details of these advantages are discussed in the following sections of this chapter.

This chapter outlines several important concepts pertaining to the overall thesis. First, NW growth is discussed in several forms including VS, SAE, and VLS. Although several growth techniques were used in this thesis, the primary method was SAE. An understanding and overview of crystal structure in NWs is established next, followed by some considerations for growing antimonide materials. Light absorption in NWs is explained in Section 1.3, with a focus on the relationship between NW diameter and its absorbing wavelength. This leads to Section 1.4 on IR photodetection, and the motivations for this thesis. Here, NW infrared

detectors are compared to competing technologies. Finally, an overview of the thesis is given in Section 1.5.

1.2 Nanowire Growth

Bottom-up NW fabrication can follow several growth mechanisms in MBE. The most commonly used NW growth method is VLS growth, which employs a liquid droplet to collect growth species and thermodynamically control the formation of sequential NW layers. VS growth, sometimes called catalyst-free growth, is a method without a liquid droplet to collect material. Instead, it relies on common thin film nucleation and layer formation, but in three-dimensions. An extension of VS growth is SAE. SAE uses the same mechanisms to form NWs as VS; however, it adds a patterned oxide mask to position the NWs and reduce film growth between them.

1.2.1 Fundamentals of Growth

Many of the concepts defined for thin film growth in MBE are applicable to NWs, especially to VS growth. In MBE, an impinging atom in the vapour phase that contacts the substrate can adsorb onto the surface (Figure 1.1). Under the right conditions, the adsorbed atom (adatom) will diffuse across the substrate until it either desorbs or nucleates. Nucleation sites expand and coalesce until they form a thin film and the process repeats.

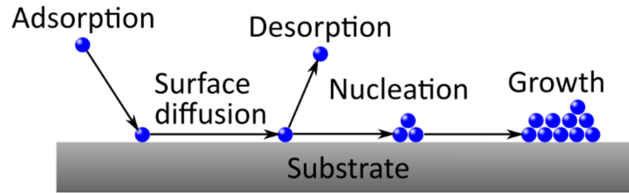

Figure 1.1: Process of material deposition in MBE. Vapour phase atoms adsorb, diffuse, and then nucleate to grow layers, or else desorb.

Adsorption of an adatom is governed by its probability of sticking. There are two types of adsorption: physisorption and chemisorption. In physisorption the atom loses some of its initial kinetic energy to the substrate and is weakly bonded to the surface with van der Waals forces. Physisorption is described as an attractive potential well with energy on the order of 10 – 100 meV [23]. Chemisorption is adsorption through chemical bonding in an exchange of electrons. The potential well used to describe chemisorption is much larger, typically 1 – 10 eV.

Desorption is the re-evaporation of adatoms and works in reverse of adsorption. If the adatom has enough energy to overcome the adsorption potential well then it can desorb back into the vacuum. The average lifetime of an adatom on the surface before desorbing is given by [23]:

$$\tau_{des} = \nu^{-1} \exp\left(\frac{E_{des}}{kT}\right) \tag{1.1}$$

where ν is the vibrational frequency of the adatoms, E_{des} is the energy barrier to desorption, k is the Boltzmann constant, and T is the temperature of the substrate.

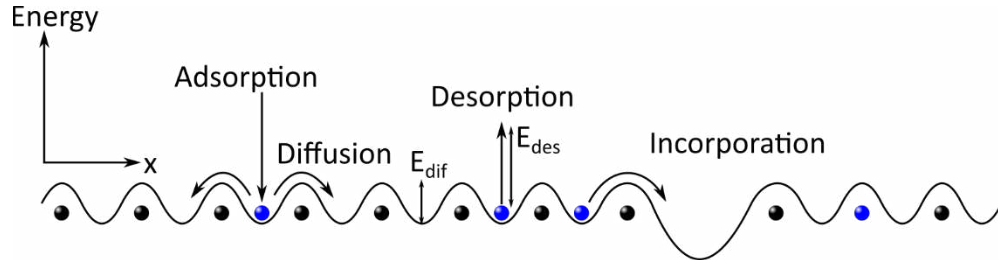

Figure 1.2: One-dimensional surface diffusion processes beginning with adsorption and ending with either desorption or incorporation. Incorporation occurs when an empty lattice site is filled with a diffusing adatom. Black spheres indicate original lattice atoms. Blue spheres indicate diffusing or new lattice atoms.

If an adatom is provided enough thermal energy it can diffuse across a surface until it either incorporates or desorbs. It moves across the surface by hopping between energy wells defined by incorporated surface lattice atoms as in Figure 1.2. For an adatom to diffuse, it must overcome the potential barrier $\mathrm{E_{dif}}$, which depends strongly on the surface construction. Adatoms that find an empty lattice site can incorporate into the surface becoming an energy barrier to future adatoms. The diffusion process is typically described by a diffusion length, which is the average distance an adatom diffuses on a surface before desorbing [23]:

$$\lambda = \sqrt{\mathrm{D}\,\tau_{\mathrm{des}}} \tag{1.2}$$

where D is the surface diffusion coefficient. In practice, the diffusion length depends on the two-dimensional surface orientation, composition, and uniformity, as well as the diffusion direction. For example, the diffusion coefficient of metal adatoms across Si(111) and Si(110) surfaces differs by an order of magnitude for typical MBE temperatures [24,25].

Due to the constant flux and flow of atoms during growth, it is often best to discuss growth in terms of thermodynamics. Thermodynamics describes the average properties of grouped atoms, such as phases, using bulk parameters. According to the second law of thermodynamics, a system at constant pressure, temperature, and volume always works to reach equilibrium by minimizing the Gibbs free energy. In a two-phase system, equilibrium is reached when the number of atoms transferring from phase 1 to phase 2 is the same as from phase 2 to phase 1. This means the change in free energy is the same whether the transfer is forward or backward. Alternatively, the two phases in equilibrium have the same chemical potential energy.

Chemical potential energy is the driving force for all crystal growth. If one phase (vapour) has a higher chemical potential than another (solid) then the thermodynamic system works to transfer particles from the first phase to the second. Overall, crystal growth in MBE is achieved by maintaining the following inequalities:

$$\mu_{\mathrm{vapour}} > \mu_{\mathrm{adatom}} > \mu_{\mathrm{solid}} \tag{1.3}$$

where μ is the chemical potential energy of the indicated phase. Chemical potential energies, and specifically their differences (supersaturation), are dependent on temperature, pressure, and deposition rate in the MBE. Vapour supersaturation to the adatom phase is constant for typical MBE temperatures and pressures. Adatom supersaturation to the solid phase is where most growth

optimization occurs and is governed by nucleation theory. Furthermore, particle transfer is limited by the kinetics discussed above (diffusion, desorption, incorporation).

Nucleation of new crystal layers occurs in small clusters of combined adatoms. Cluster formation changes the Gibbs free energy of the system:

$$\Delta G = \Delta G_{Volume} + \Delta G_{Surfaces} \quad (1.4)$$

where ΔG is the change in free energy to nucleate, ΔG_{Volume} is the change in free energy associated with forming a new volume, and $\Delta G_{Surfaces}$ is the change in free energy associated with forming new surfaces. Volume formation is related to the chemical potentials of the phases according to $\Delta G_{Volume} = -n(\mu_{adatom} - \mu_{solid})$, where n is the number of atoms transferred. Surface formation is driven by $\Delta G_{Surfaces} = \gamma\xi$, where γ is the energy per unit area required to form a surface (surface energy) and ξ is the surface area of the formed solid. Free energy is reduced when $|\Delta G_{Volume}| > |\Delta G_{Surfaces}|$. Therefore, nucleation occurs when there is a large adatom supersaturation and/or a small energy to form a surface.

Adatoms continue to incorporate to form clusters. At some critical radius the free energy of the cluster is at a maximum. This maximum in free energy is the barrier to formation of a stable cluster (Figure 1.3a). Beyond this critical radius, free energy is minimized by increasing the radial size of the cluster, rather than form new clusters, thereby forming a complete crystal layer.

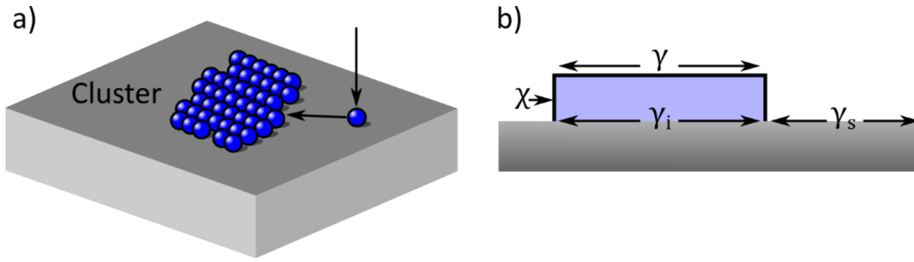

Figure 1.3: Nucleation of clusters. a) Adatoms contribute to a cluster that has surpassed its critical radius. b) Surface energies of a cluster in cross-section. γ, γ_i, γ_s and χ are the surface energies of the top surface of the cluster, the interface between the cluster and the growth surface, the growth surface itself, and the formation energy of the edge.

The type of nucleation and subsequent growth depends on the surface energies shown in Figure 1.3b. Growth is determine by the wetting parameter ($\Delta\gamma$) which is given by $\Delta\gamma = \gamma + \gamma_i - \gamma_s$. If $\Delta\gamma < 0$ then the free energy is minimized by incorporation on the growth surface (i.e. the adatoms prefer to stick to the substrate). If $\Delta\gamma > 0$ then the free energy is minimized by nucleating in three dimensions and avoiding layer-by-layer growth on the surface (i.e. the adatoms prefer to stick to each other). If $\Delta\gamma = 0$ then the cluster and substrate are the same material and two-dimensional nucleation occurs.

From these conditions there are three main crystal growth modes in MBE shown in Figure 1.4. Layer-by-layer growth reduces free energy by covering each previous layer fully before beginning the next. Island growth reduces free energy by minimizing the contact area with the substrate and forming a three-dimensional cluster. Stranski-Krastanov (SK) growth begins as layer-by-layer but,

due to strain energy, the growth will transition to island growth. This is a common method of forming quantum dots [26].

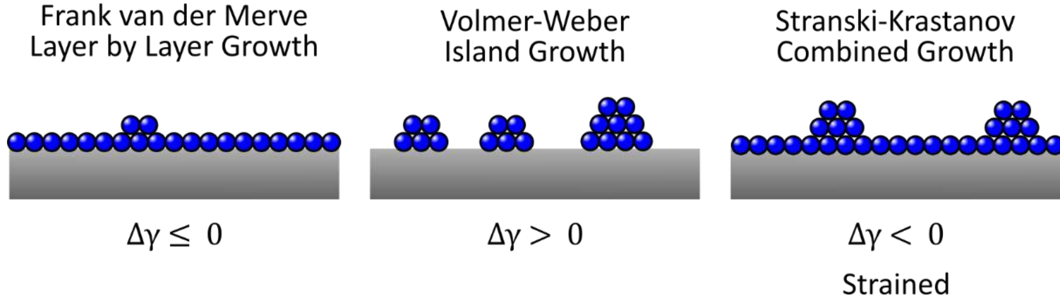

Figure 1.4: Three main crystal growth modes in MBE. Layer-by-layer: each layer is completed before nucleating the next. Island: three-dimensional islands are formed leaving the surface mostly uncovered. Stranski-Krastanov (SK): combined layer-by-layer and subsequent island growth.

The nucleation rate of clusters depends on the barrier to formation (ΔG^*), the attachment rate of adatoms to the cluster (ω^*), and the concentration of single unit large clusters (c_1) [23]:

$$J = \omega^* Z c_1 \exp\left(\frac{\Delta G^*}{kT}\right) \qquad (1.5)$$

where Z is the Zeldovich factor used to account for variation in cluster size and shape. For a circular, two-dimensional cluster, the barrier to nucleation is [23]:

$$\Delta G^* = \frac{\pi \chi^2}{n_0 \Delta\mu - (\Delta\gamma)} \qquad (1.6)$$

where n_0 is the density of lattice sites on the surface and $\Delta\mu$ is the chemical potential difference between the adatom and solid phases. Nucleation is therefore dependent on temperature, pressure, and deposition rate in the MBE

system. For example, decreasing substrate temperature in MBE often increases $\Delta\mu$, which in turn increases the nucleation and growth rates [27]. Furthermore, ω^* and chemical potential are surface orientation-dependent parameters thereby linking the nucleation barrier to specific crystallographic surfaces (facets). ω^* increases with increasing surface diffusion coefficient. In this way, the directional growth rate of crystals is controlled by both kinetics and thermodynamics.

Thus far, the crystal growth discussion has been limited to a single adatom species on a monocrystalline substrate; however, this thesis is focused on III-V NW growth. When growing binary III-V materials the group III and group V elements must combine epitaxially to form layers. They follow completely independent kinetics and thermodynamics with their own adsorption, diffusion, desorption, and incorporation rates, as well as their own chemical potential differences.

1.2.2 Vapour-Solid (VS)

VS growth of NWs is similar to the VS mechanism of thin film growth discussed in the previous section. The main growth steps are shown in Figure 1.5. First, nuclei are formed on the substrate under conditions of island or SK growth with a rate dependent on the growth conditions as well as substrate defects [28,29]. The three-dimensional nuclei often form irregular high energy facets due to the differences in surface energies between the nucleus and the substrate. Over time, high energy facets begin to disappear because of their higher growth rate, while lower energy facets dominate the crystal morphology [30]. Eventually, only a few primary facets remain. The overwhelmingly common morphology of VS NWs

includes a [111] top facet and six {-110} side facets that form a hexagonal cross-section [28,31–36].

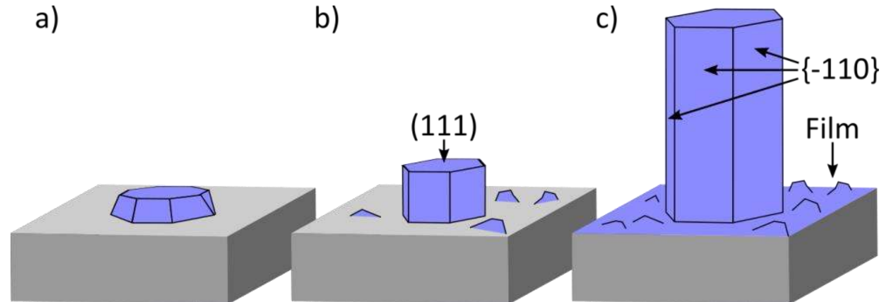

Figure 1.5: VS growth progression showing a) Nucleation of multi-facetted nucleus, b) extinction of high index facets, and c) simultaneous axial and radial growth of primary facets depending on growth parameters. Parasitic film growth is also indicated.

Growth of any NW structure requires that the axial growth rate (elongation) be faster than the radial growth rate. For VS growth this means the supersaturation of adatoms on the top facet must be higher than on the side facets. However, due to the VS mechanism at work here, the NWs commonly show correlated axial and radial growth rates. It is possible, however, to accent one mode over the other. Axial growth primarily progresses in the [111] direction on a (111) surface. (111) surfaces typically have higher surface energies than {-110}, thereby leading to preferential nucleation on the top facet. Radial growth can be accented by increasing the supersaturation of adatoms on the side facets, reducing the adatom supply to the top facet, and overall decreasing the adatom diffusion lengths on the side facets. This is often achieved by decreasing temperature [37,38].

During VS growth there is always competition for growth species between the NWs and a parasitic film on the substrate. Only a small fraction of nucleation events form the appropriate facets for NW growth. The remaining form large clusters that coalesce into a polycrystalline film covering the substrate. Not only does this film prevent further NW nucleation but it also reduces the local adatom supersaturation through its own incorporation. Furthermore, it can affect ternary and quaternary compositions, as well as doping in the NWs [39]. Ultimately, it is the parasitic film that limits VS growth as a viable fabrication technique for NW devices.

1.2.3 Selected Area Epitaxy (SAE)

SAE growth is an extension of VS growth. It follows the same nucleation and facet formation processes, but a mask is used to reduce the parasitic film growth between the NWs. At normal growth conditions the mask will increase the desorption or diffusion rate of one or more of the growth species. This inhibits nucleation either by increasing the barrier to nucleation or by decreasing the chemical potential difference. SAE is the most important growth mode in this thesis.

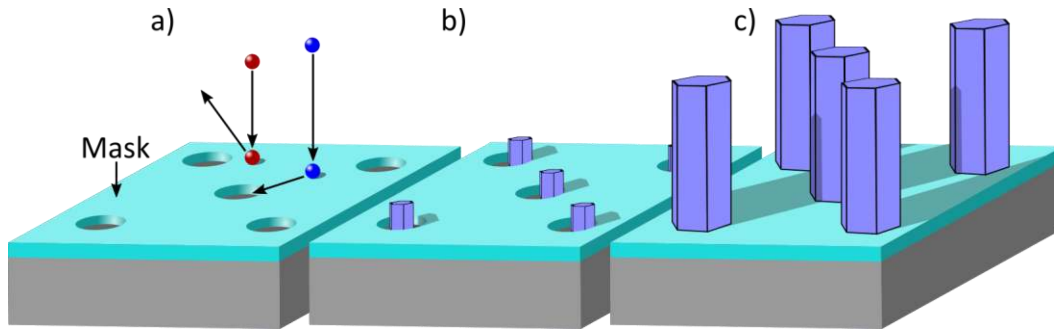

Figure 1.6: SAE growth progression. a) Growth impeding mask controls the nucleation position of NWs either by diffusion or desorption of growth species. b) NWs nucleate epitaxially in holes in the mask. c) Growth continues as VS. Shadowing becomes important as NWs grow taller.

Figure 1.6 shows the growth of SAE NWs. First, an oxide mask is prepared following steps as outlined in Section 3.1. Typically the mask is either SiO_2 or SiN [40]. An oxide mask is used because its growth and etching are well developed processes, and it has been shown to minimize film growth on the substrate (i.e. to improve selectivity) [35,41]. Processing steps open periodic holes through the oxide to the substrate surface. Next, growth is initiated in the MBE. Growth species preferentially nucleate on the exposed substrate surface and form the VS morphology. Lastly, NW facets continue to enlarge according to the growth conditions.

There are several benefits to the SAE growth mode. Foremost is the ability to quantify growth results by defining a NW yield. NW yield is defined as the fraction of holes filled by a vertical NW, often expressed as a percentage. This has helped optimize growth parameters for many material systems and allowed some groups to reach ~100% NW yield [42–44]. SAE also enables unique control over

NW position and morphology. The uniformly positioned NW sites lead to an increased control and uniformity of the diffusive adatom flux. Once NWs reach a certain length they start to shadow neighbouring NWs and mask areas, which affects local material fluxes [41]. In a uniform array the shadowing is consistent for all NWs, and therefore material fluxes are consistent. Next, the size of the holes provides some control over the final NW dimensions, in that large diameter holes will produce larger diameter NWs than small holes. Combining all these geometric controls of NW position, diameter, and length, SAE NWs can have superior optical characteristics [45,46] (Section 1.3). Another benefit is the ability to grow core-shell structures with uniform doping, passivation, and other heterojunctions [47]. Finally, it is simpler to planarize and contact uniform SAE NW arrays during device fabrication [48].

It should be noted that although SAE is referred to as a growth mode in this thesis, since it is the primary method of forming NWs, it technically does not describe the growth of the NWs. Instead it is a method of controlling the VS growth mode. With that in mind, it is possible to perform SAE using other growth modes such as vapour-liquid-solid, which is discussed in the next section.

1.2.4 Vapour-Liquid-Solid (VLS)

VLS growth is a process of forming NWs using a liquid droplet. In the MBE, growth species from the vapour phase are adsorbed into the liquid droplet and eventually layered in the solid phase to form a NW (hence the term "vapour-liquid-solid"). VLS is the most common growth mode since the first NWs in 1964 [1].

Since then it has been used to grow NWs of a large variety of materials [49,50], and structures [51]. Historically, the liquid droplet has been gold (termed Au-assisted); however, gold is known to produce deep level traps in silicon [52] and is therefore incompatible with any underlying silicon devices such as CMOS. Instead, NW research has shifted away from Au-assisted VLS, replacing Au with one of the growth species as the liquid droplet (termed self-assisted).

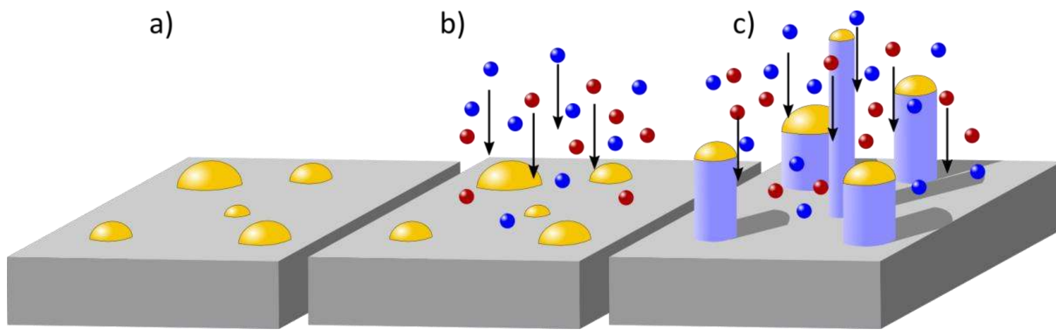

Figure 1.7: VLS growth progression. a) Seed particles are deposited onto a substrate using various in-situ and ex-situ methods. b) Growth species are supplied to the substrate surface and are adsorbed by the seed particles. c) Supersaturation of the seed particle occurs, and a solid phase is formed beneath the liquid droplet. Repetition of this process creates a long, thin crystal (NW).

Figure 1.7 outlines the process for VLS growth and is applicable to both Au-assisted and self-assisted methods. First, liquid droplets (seed particles) are formed on the substrate surface. For Au-assisted growth, a thin (1 – 10 nm) layer of gold is deposited onto the substrate, followed by annealing in the MBE to form randomly distributed liquid gold droplets [53]. For self-assisted growth, one of the growth species forms droplets in the MBE at the growth temperature. Next, growth species impinge on the substrate and diffuse until they are adsorbed by the droplets. Eventually the droplets will reach thermodynamic supersaturation

of the growth species where it becomes energetically favourable to nucleate at the liquid-solid interface under the droplet. Once a nucleation event occurs, the adsorbed growth species incorporate to form a complete layer and the process repeats.

VLS NWs grow in competition with the film similar to VS NW growth. An oxide mask can be used to prevent the film growth, thus creating SAE-VLS growth. Both Au-assisted and self-assisted NWs can be grown in the SAE mode. The latter begins like SAE-VS NWs but nucleates a liquid droplet in the oxide holes, which continues as VLS for the duration of growth. This mode is not considered in this thesis. Au-assisted growth (with and without SAE) is discussed in Chapter 4.

1.2.5 Crystal Structure

Axial NW growth progresses layer-by-layer in the [111] direction. Each epitaxial III-V layer can take one of three spatial arrangements denoted A, B, or C (Figure 1.8). A repeating two-layer sequence (AB-AB-AB) is called wurtzite (WZ), while a repeating three-layer sequence (ABC-ABC-ABC) is called zincblende (ZB). Depending on the growth parameters, NWs may be ZB or WZ or a combination of both. Both crystal phases can form in NWs due to the small difference in nucleation energy for some materials (i.e. InAs [54]). High temperatures or supersaturations have large fluctuations in energy during growth [55]. These large fluctuations make the small energy difference between ZB and WZ insignificant and thus the material can switch phases. Materials with low ionicity (antimonides)

predominantly grow in a ZB crystal structure, while materials with a high ionicity (nitrides) favour WZ [56].

When NWs have an interruption in the regular stacking sequence, it is referred to as a stacking fault or a twin plane. Stacking faults may occur as a transition between crystal phases (AB-AB-ABC-ABC) or they may be a single irregular insertion (ABC-AB**A**-ABC). Twin planes are a reversal of the stacking sequence, which can only occur in ZB (ABC-ABC-B-CBA-CBA). Both can degrade optical properties of NWs due to the different band structures of ZB and WZ [57]. They also act as scattering centres for electrons, which can increase resistivity through the NW by a few orders of magnitude [58].

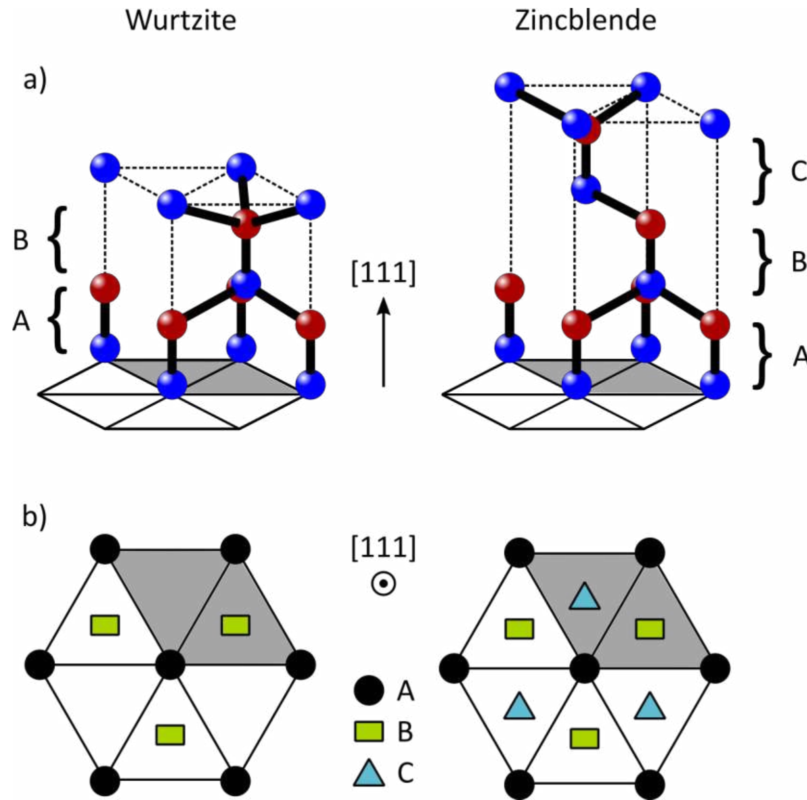

Figure 1.8: Atomic stacking in the wurtzite (WZ) and zincblende (ZB) crystal phases for III-Vs. a) Side profile with indicated A, B, and C layers. Dotted lines are a guide for the eye. b) Top down view in the [-1-1-1] direction with indicated lateral positions of the A, B, C layers. Shaded regions in b) highlight the position of the lattice drawn in a).

III-V NW growth often occurs on Si(111) or III-V(111)B substrates so that growth progresses perpendicular to the substrate. However, it is also possible to grow NWs in non-vertical equivalent [111] directions depending on substrate preparation [33] or crystal phase changes [59]. Non-vertical NWs can also be due to the non-polar nature of Si(111) substrates. On III-V substrates the close packed [111] direction alternates between a group III terminated surface (type A) and a group V terminated surface (type B). A type A surface has 3 equivalent [111]B directions for NW growth, all orientated at 19.6° to the surface and 120° to each

other [60]. Thus, vertical NW growth can be as simple as choosing a III-V(111)B substrate. However, silicon substrates are non-polar and the type designations do not exist. It is therefore possible to grow NWs in the vertical [111]B direction as well as the tilted [111]A directions. Tomioka et al [33] found they could control the direction of InAs growth on Si(111) by passivating the exposed silicon with As. The As-incorporated surface acted like a III-V(111)B surface and eliminated the other possible [111]A directions for the subsequent NW growth.

Thin film heterojunctions form dislocation defects when there is a large lattice mismatch and the deposited film is greater than some critical thickness. During deposition, strain energy will accumulate and can only be released by the creation of a defect. In contrast, NWs can accommodate the same lattice mismatch without defects by relieving some of the energy. The energy is relieved along the sidewall surfaces of the NWs; therefore, it is the high surface-to-volume ratio in NWs that allows for mismatch tolerance. This was first described theoretically by F. Glas [61]. He showed that for a given lattice mismatch, there exists a critical NW radius below which the NWs may grow infinitely long without forming defects due to strain. Epitaxial growth of many axial heterostructures have been demonstrated. For example, III-Vs on III-Vs [62,63], and III-Vs on silicon [64–68].

Radially grown heterojunctions (core-shell NWs) will also form defects for a thick shell. Haapamaki et al [69] created an analytical model to predict the critical shell thickness for InAs-$Al_xIn_{1-x}As$ core-shell NWs. They found that as the core

radius became large, the critical shell thickness approached the constant thin film critical thickness. In general, the critical thickness for a two-dimensional thin film is smaller than the critical thickness of a radial shell, which is smaller than the critical thickness (length) of an axial NW.

1.2.6 Antimony (Sb) Growth Considerations

Most growths performed in this thesis were antimony (Sb)-based alloys. Antimonide (III-Sb) semiconductors have many unique properties that separate them from arsenic and phosphorus compounds. Antimonides have the largest lattice parameters and the smallest bandgaps (0.084 eV) of all the III-V's. They also have high electron mobilities (77,000 $cm^2\ V^{-1}\ s^{-1}$ for InSb) and low thermal conductivity, which is ideal for thermoelectric devices. However, Sb growths remain the most difficult to perform due to antimony's low vapour pressure, its surfactant effect, and the memory effect.

III-V growth by MBE (excluding Sb) is always performed at a V/III ratio greater than one since group V's desorb more readily than group III's. This ensures a supersaturation condition of group V for growth and any extra material will simply desorb. In typical MBE conditions, elemental Sb has a vapour pressure 5 orders of magnitude less than arsenic [70,71]. Because of its low vapour pressure, it does not desorb and can easily build up on NW and oxide surfaces, reducing selectivity in SAE. Growth of antimonides can be kept at a V/III ratio of 1 to minimize this effect.

Due to the large size of Sb (atomic number of Z = 51), and its relatively large covalent bonds, it tends to have a low incorporation rate during growth. Instead, it floats on top of the surface without being incorporated. This is called the surfactant effect. The surfactant effect disturbs the surface energy of the growing facets, thereby changing the facet growth rates. It can also limit the three-dimensional growth during initial nucleation of the NWs [72]. Finally, the diffusion length of adatoms is often reduced across surfaces passivated by Sb [73].

The memory effect is the result of both the low vapour pressure and the surfactant effect of Sb. It is the ability of Sb to remain on the growth facets for a significant time even after terminating the source flux. As a result, the subsequent layers may have unintentional Sb incorporation and it often leads to graded heterojunctions when changing from antimonides to other III-Vs.

1.3 Nanowire Absorption

With careful engineering, NWs can have enhanced optical properties over thin films of the same material, thickness, and quality. NW arrays have been demonstrated with increased optical absorptance as compared to thin films [74] and selectivity of the absorbing wavelength [75–77], both as a result of the unique geometry of NWs. Four optical phenomena arise in an array of NWs: radial mode resonance, anti-reflection, evanescent coupling, and Fabry-Perot resonance. The advantageous absorbing properties are primarily caused by radial mode

resonance due to the symmetry of the NWs. Light at specific wavelengths is coupled into these resonances, which can subsequently be absorbed by the NWs. The efficient coupling of light is due to the large change in refractive index between the NW material and surrounding air. This creates an anti-reflective effect in the NWs. Evanescent coupling can also affect absorptance depending on the separation between NWs. The final phenomenon, Fabry-Perot mode resonance, is caused by standing wave solutions in a NW with finite longitudinal boundary conditions. It was found to have little affect on absorptance for NW lengths greater than 500 nm, and therefore will not be discussed further [45,46].

1.3.1 Radial Resonance

Radial mode resonance occurs when incident light couples to the waveguiding modes that exist within a NW. Coupled light can then be absorbed in the semiconducting NW following an exponential decay of light intensity. Resonance occurs most strongly at a specific resonant wavelength for a given mode. This effect can be used to tune absorbing wavelengths in geometrically uniform NW arrays [45,46].

Radial mode resonances include transverse electric (TE), transverse magnetic (TM), and hybrid (HE) modes. They arise in cylindrical waveguides due to the radial symmetry ($\varphi = \varphi + 2\pi$) and the radial boundary ($0 \leq \rho \leq R$) defined by the change in refractive index between the waveguide and the surrounding space ($n_1 > n_2$), as shown in Figure 1.9b. Circular cross-sections are shown here for simplicity. Applying these conditions to the typical hexagonal

cross-section of NWs is discussed later. In TE modes all electric field components are perpendicular to the propagation direction. In TM modes all magnetic field (H) components are perpendicular to the propagation direction. HE modes have a non-zero component of both fields in the direction of propagation. All three mode types are designated by m and n subscripts that indicate angular index and radial index, respectively.

If an incident plane wave has a wavelength that corresponds to the resonance of the waveguide, they will strongly couple, and the light will be funneled into the waveguide. HE_{1n} modes are responsible for coupling and guiding light in vertical NWs [74,78,79]. A polarized plane wave (Figure 1.9a) couples most strongly with HE_{11} (Figure 1.9c) because they are symmetric across the yz-plane and antisymmetric across the xz-plane. Other low-order modes are shown in Figure 1.9 but clearly do not share the symmetries of a plane wave.

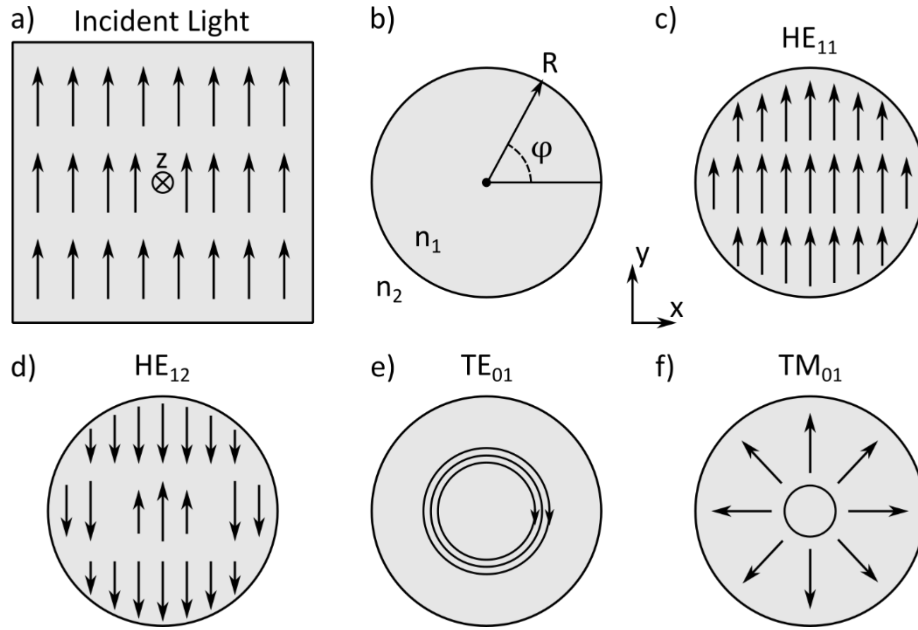

Figure 1.9: Electric field patterns of cylindrical waveguiding modes in cross-section as compared to a polarized incident plane wave. a) Incident plane wave propagating in the z direction. b) Geometric and optical parameters of the waveguide. Radial mode resonance electric field patterns for c) HE_{11}, d) HE_{12}, e) TE_{01}, and f) TM_{01}.

According to Maxwell's equations, the general solution for the transverse component of the electric field in cylindrical coordinates is comprised of Bessel (J_m) and Neumann (N_m) functions [80]:

$$E(\rho) = A_m J_m(\rho T) + B_m N_m(\rho T) \quad (1.7)$$

where A_m and B_m are constants pertaining to the boundary conditions, T is a constant related to the wavenumber in the waveguide, and m is an integer. In a cylindrical waveguide m is an integer value because of the radial symmetry of the azimuthal angle and B_m is set to zero because the Neumann function is not well

behaved at $\rho = 0$. Using boundary conditions for the z component of the electric field with no evanescent field outside of the NW:

$$J_m(RT) = 0 \tag{1.8}$$

Since the Bessel function can be approximated as a sine wave, RT must be an integer value of π ($RT = n\pi,\ \text{for } n \in \mathbb{Z}$) and,

$$\lambda_{HE1n} = \frac{Re[\bar{n}]D}{n} \tag{1.9}$$

where $Re[\bar{n}]$ is the real part of the complex index of refraction of the mode, and D is the diameter of the NW ($D = 2R$). Thus, there is a clear relationship between the diameter of the NW and the peak wavelength of the HE_{1n} waveguiding mode. The true hexagonal cross-section of a NW was shown not to affect the resonant wavelength of the guided mode for the same cross-sectional area [80]. All diameters quoted in this thesis were for a hexagonal cross-section. NW diameters were converted to an effective circular cross-section for simulations using:

$$D_{circ} = \sqrt{\frac{3\sqrt{3}}{2\pi}} D_{hex} \tag{1.10}$$

where D_{circ} and D_{hex} are the diameters for a circle and a hexagon, respectively.

K. Azizur-Rahman and R. LaPierre performed a simulation study of GaAs, InP, and InAs NWs that explored the relationships between NW array geometry and absorptance [45]. They identified several important results related to the radial NW modes. First, they found two major peaks in the absorptance spectra

that corresponded to HE_{11}, and HE_{12} guided modes. These two peaks linearly red-shifted with increasing NW diameter. HE_{11} was found at longer wavelengths than HE_{12} with a greater absorptance. The absorptance was even greater than that from a thin film of the same thickness. The large absorptance in NWs was due to the stronger coupling to HE_{11} as discussed above. Thus, HE_{11} is the most important mode for efficiently coupling light into a NW. They also showed that most of the absorptance in the HE_{11} mode occurs near the top of the NW, thereby making Fabry-Perot resonances negligible. Finally, the linear shift in absorptance with diameter was quantified. For all three materials, the HE_{11} shift was approximately 3.2 nm/nm (wavelength shift [nm]/diameter increase [nm]), while HE_{12} was 1.3 nm/nm. These findings identified an important relationship between absorbing wavelength and NW diameter, which can be employed for selective light absorption.

1.3.2 Evanescent Coupling

Evanescent mode coupling occurs when the evanescent part of the radial mode overlaps with neighbouring NWs. Some of the confined radial mode is transferred to the neighbouring NW; thus, they are amplitude coupled. The overall effect in an array of NWs is to increase the absorptance of the array, depending on the spacing between NWs. An optimal diameter-to-period ratio was found previously to be between 1/3 and 2/3 [45]. Below this region, when diameters are small or period is large, the array is deemed sparse and evanescent coupling is insignificant. Above the optimal region, when diameters are large or period is

small, the array is deemed dense and reflectance off the top of the NWs becomes important as it approaches a continuous thin film surface. Consequently, the absorptance magnitude decreases. Within the optimal region there is a blue-shift of the HE_{11} absorptance peak wavelength with increasing NW density (constant diameter, decreasing period). This shift was found to be less than 0.4 nm/nm for GaAs, InP, and InAs NWs [45]. The blue-shift from evanescent coupling has less of an effect on the HE_{11} peak than the radial mode; therefore, diameter is the more important parameter for tuning absorbing wavelength.

1.3.3 Absorptance in the NW

Once light is coupled into the NW it can be absorbed through the generation of electron-hole pairs for wavelengths up to the bandgap. The bandgap is still the upper limit for absorbing wavelength, even though longer wavelengths can be coupled into the NW geometrically [74]. The light intensity follows a rough exponential decay along the length of the NW [78]:

$$\mathrm{I(x)} = \mathrm{I_0} \exp(-2\mathrm{Im}[\bar{\mathrm{n}}]\mathrm{k_0 x}) \qquad (1.11)$$

where $\mathrm{Im}[\bar{\mathrm{n}}]$ is the imaginary part of the complex index of refraction of the mode, $\mathrm{k_0}$ is the vacuum wavenumber, and $\mathrm{I_0}$ is the initial intensity of the incident wave. x is the position along the NW's length where x = 0 is the tip of the NW. The refractive index of the mode is both mode-dependent and wavelength-dependent. Equation 1.11 indicates that longer NWs are better for maximizing NW absorptance. K. Azizur-Rahman and R. LaPierre found that 90% absorptance was

achievable with 750 nm long NWs for GaAs and InP [45]. When compared to thin film of the same thickness, the absorptance at these HE_{11} wavelengths were 50% and 65%, respectively. Therefore, radial resonant modes push the absorptance of NW arrays beyond a thin film.

1.4 Nanowire Infrared Detectors

A photodetector is a device that interacts with photons directly or indirectly to produce an electrical signal. Photoconductors, photodiodes, and phototransistors are all types of photodetectors that operate in many spectral regions. In the infrared (IR) region, there are also thermal detectors, which depend on thermal interactions to induce a current (thermoelectric effect, and changes in resistance).

Photodiodes rely on the depletion region of a p-n junction to separate optically generated electron-hole pairs (EHPs). Photons with energies greater than the bandgap of the semiconductor can be absorbed and generate an EHP. Once EHPs are generated, the minority carriers can diffuse to the depletion edge where they drift across the depletion region. Separated EHPs can be detected with an external circuit. Heterojunction devices operate similarly but are fabricated using two semiconductor materials with different bandgaps.

IR photodiodes may operate in any of the several IR regions summarized in Table 1.1 below. Immediately following the visible spectrum is the near infrared

(NIR) range. NIR is used in the telecommunications industry since these wavelengths have low loss in SiO_2 fibres. It can also be used for image intensifier night vision [81]. Short-wave infrared (SWIR) wavelengths are limited in open air by high water and CO_2 absorption. This is beneficial in agricultural sorting since high moisture content regions (like bruises) can be visualized. SWIR also has industrial applications in high temperature monitoring and manufacturing due to its high transmittance through glass and plastics. Mid-wave infrared (MWIR) has an atmospheric window at 3 – 5 µm where transmittance is very high. These wavelengths are primarily used for long distance communication and military applications. It also has applications in gas analysis, lower temperature manufacturing, and long-distance chemical analysis (astronomy). Long-wave infrared (LWIR) is primarily used in thermal detection and night vision. It is emitted by all materials and therefore does not require an external illumination source.

A multispectral photodetector is one that can absorb and distinguish several IR wavelengths in a single detector. Ideally a multispectral detector would not need to use expensive filtering techniques above the detector to separate wavelengths. This would allow IR detectors to be cheaply applied to numerous applications concurrently.

Table 1.1: IR wavelength ranges and corresponding black body temperature peaks

Region	Wavelength Range (µm)	Temperature Range (°C)
NIR	0.75 – 1.4	1800 – 3500
SWIR	1.4 – 3	700 – 1800
MWIR	3 – 8	700 – 90
LWIR	8 – 14	90 – -80

Modern IR technologies were introduced in the 1940's, moving beyond the simple thermal detectors onto photoconductive detectors [82]. Since then there have been four generations of IR photodetectors. The first used one-dimensional arrays of cooled photoconductors and scanning optics. The second generation introduced two-dimensional focal-plane arrays (FPAs) with read-out integrated circuits (ROICs), photodiodes, charge-coupled devices (CCDs), and quantum well infrared photodetectors (QWIP). The third generation developed two-color FPAs, III-V superlattice detectors, bolometers, and introduced quantum dot infrared photodetectors (QDIP). The fourth generation is currently developing advanced optical coupling techniques, three-dimensional and multispectral pixels, all while continuing to reduce pixel size [83]. Most photodetectors in the market are MCT, microbolometers, or InSb detectors. The advantages and disadvantages of these technologies are discussed in the following sections.

1.4.1 Mercury Cadmium Telluride (MCT) Detectors

Some advantages of MCT detectors include high detectivity (>10^{11} Jones), a large spectral range (1 – 30 µm), direct bandgap, long carrier lifetimes, relatively high operating temperatures, and good carrier mobilities. This ternary

semiconductor is also completely lattice matched between its constituent binaries. Problems with MCT include limited multispectral capabilities, expensive substrates for lattice matching, expensive fabrication techniques, and safety concerns with mercury. MCT also suffers from bulk, surface, and interface instabilities due to weak Hg-Te bonds [83].

The fabrication of MCT films sparked the modern movement of IR photodetectors beginning in the first generation with a one-dimensional photoconductive array and moving to the 3-D multispectral photodiodes that exist today. The basic operation of MCT photodetectors consists of p-n junction photodiodes in the photocurrent (reverse biased) region. Wavelength detection ranges are selected via composition (x) of $Hg_{1-x}Cd_xTe$. Figure 1.10 shows more recent dual band three-dimensional MCT detectors. These detectors are grown on CdZnTe substrates and then indium bump bonded to silicon read-out integrated circuits (ROICs).

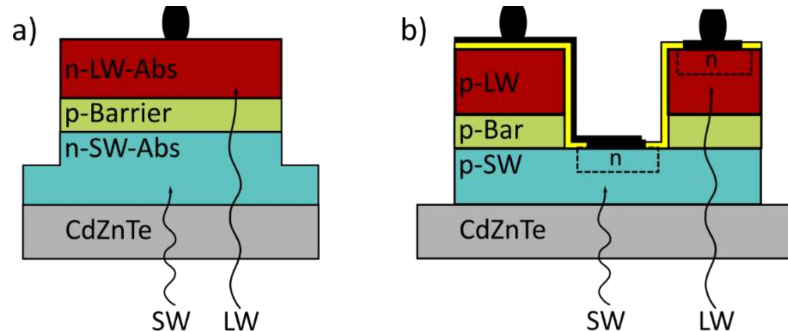

Figure 1.10: Dual band MCT photodetector architectures. a) bias-selectable n-p-n and b) simultaneous homojunction structure [6]. Metal interconnects and indium bump bonds are shown in black. Electrical isolation is shown in yellow. Long-wave (LW) and short-wave (SW) absorption regions are indicated.

In layered multiband detectors, the short-wave absorber material is first in the optical path so that the incident spectrum is absorbed up to its cutoff wavelength and the remainder transmits to the next level. Figure 1.10a is a bias-selectable sequential mode detector [82]. When a positive voltage is applied to the indium bond the top photodiode is reverse biased and the bottom one is forward biased. The forward biased photodiode is shunted by its low impedance resulting in photocurrent only from the reverse biased photodiode. When the polarity is switched the situation reverses and photocurrent is extracted only from bottom photodiode. Thus, the structure can detect both IR ranges sequentially but not simultaneously. Figure 1.10b is a simultaneous homojunction dual band detector. This structure is simply two single band detectors in reverse bias stacked on top of each other. Again, the short-wave absorption region comes first in the optical path; however, the structure requires two separate electrical contacts and ROICs. The electrical signals are read out simultaneously but at a cost of pixel and ROIC size. This idea can be extended to three or four levels, each with a different cutoff wavelength [84].

1.4.2 InSb Detectors

The most common III-V material for IR photodetection is InSb. InSb has a cutoff wavelength of 7.3 μm at 300 K and 5.4 μm at 77 K making it a MWIR detector. InAsSb with an antimony composition around 62% has a cutoff wavelength of 14.7 μm at 300K and 9 μm at 77 K making it possible to access the LWIR region. InSb photodetectors follow similar photodiode architectures as the

MCT detectors (p-n, p-i-n, and heterostructures). InSb detectors have several advantages over MCT; namely, more chemically stable, less fragile, and better device yield. However, they suffer from a lack of lattice matched substrates. Buffer layers of GaSb are required to integrate InSb with GaAs substrates [85], and then indium bump bonding to silicon for ROIC [86]. AlSb has been shown to work as a buffer layer for InSb thin films on silicon [87–89]. Finally, InSb offers no multispectral capabilities without the ternary InAsSb or heterostructure integration with MCT.

1.4.3 Microbolometers

Microbolometers are a type of thermal detector, which measure resistance changes in the active thermistor material due to absorbed heat. The most common active materials are vanadium dioxide (VO_2) and amorphous silicon (α-Si). VO_2 has a high negative temperature coefficient of resistance (>4% per degree) giving a large measurable change in resistance for every degree change in temperature. Complicated multistep fabrication is used to thermally isolate the bolometer pixel from the substrate.

Microbolometers make up about 95% of uncooled IR detectors in the market with costs dropping about 15% per year [90]. They are also small, low power, have long lifetimes, and are relatively inexpensive to fabricate. Recently, Seek Thermal and FLIR have produced bolometers below the $1000 mark enabling access to a larger consumer market. However, bolometers tend to have low

detectivity and are slow to respond. They also have the broadest spectral response and therefore do not have any multispectral capabilities.

1.4.4 InAs(Sb) Nanowire photodetectors

InAsSb NWs are a fourth-generation photodiode being developed as a potential alternative to MCT and as an improvement on InSb bulk detectors. NWs improve upon several fabrication limitations of MCT detectors and have inherent light trapping capabilities while all other detectors require an antireflection coating (ARC). They also have higher absorptance using less material and have controllable peak detection wavelengths. Finally, NWs are the ultimate in IR pixel size reduction with single NWs as small as 500 nm in diameter for optimal MWIR absorption.

NW photodetectors have vertical, forest-like arrays of NWs in direct contact with the ROIC. Under illumination, EHP are generated in the NWs, separated by a p(i)n-junction (or heterojunction) within the NW, and electrons are driven down into the ROIC. In general, NWs have shown reasonable detectivities (10^8 – 10^{11} Jones) and very high gain (>10^6) [91–93]. Unlike quantum devices (QWIP, QDIP), NWs can operate at room temperature with low dark currents (pA – nA range).

As discussed in Section 1.3, absorptance in NWs can exceed that from a thin film of an equivalent thickness due to the HE_{1n} waveguiding modes. Figure 1.11 shows several HE_{11} absorptance peaks in simulated InSb NWs from [46]. The

values selected for diameter (D), period (P), and length (L) of the NW array produces approximately 80% absorptance. An InSb thin film with thickness of 10 µm never exceeds 70% absorptance while even the longest NWs are only 3.5 µm. Finally, wavelength specific absorptance peaks can be used to create multispectral photodetectors. Instead of a stacked heterostructure, these NW arrays can be positioned side-by-side.

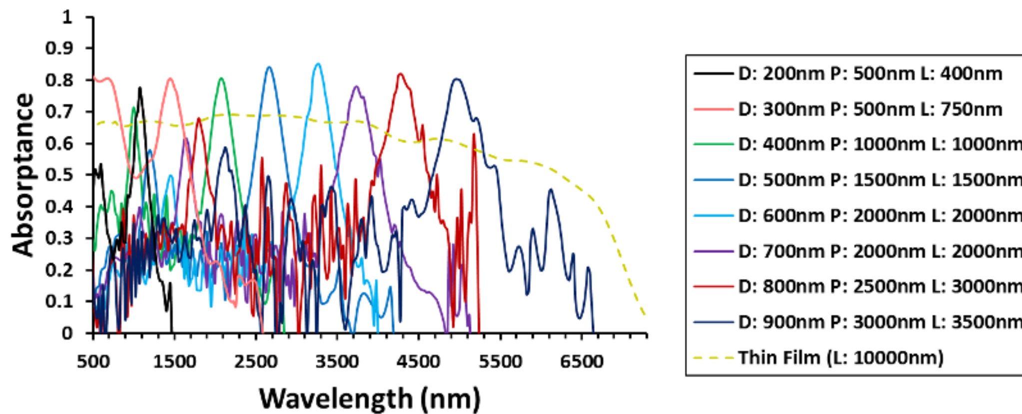

Figure 1.11: Simulated absorptance of InSb NWs with indicated diameter (D), period (P), and length (L). Dimensions were chosen for ~80% absorptance. Thin film of InSb is shown for comparison. Adapted from [46].

NWs may adopt a radial (core-shell) structure in which the p-n junction is created in the radial direction instead of along the length of the NW (axial). This geometry eliminates the known trade-off between absorbing thickness and carrier diffusion to the junction. Instead, the radial dimension of the NWs can be kept smaller than the carrier diffusion length such that nearly all photogenerated carriers are collected (high internal quantum efficiency (IQE)), while the length of

the NW is selected to absorb all the incident light (high external quantum efficiency (EQE)).

A pixel may consist of a full array of NWs or as few as a single NW. A set of multispectral subpixels would require at least one NW per desired wavelength range. MCT detectors have reached a pixel size of 5 µm and microbolometer pixels are fabricated as small as 12 µm. A multispectral NW array sensitive to MWIR could easily be as small as current microbolometer pixels and a solitary NW will be much smaller than MCT technology. If a multispectral pixel consisted of a few single NWs, each with different diameter, then multispectral detection could be achieved with pixel sizes comparable to MCT. However, this level of size control does not currently exist for InAsSb NWs.

To realize the many advantages of IR NW photodetectors, several issues must be solved and knowledge gaps must be filled. For instance, vertical yield of NWs on silicon, strong dimensional and compositional control, experimental validation of absorption characteristics, and improved carrier collection and dark current. As a final step the NW arrays must be fully integrated with existing CCD ROIC technology.

InAsSb NWs on silicon substrates have been notoriously difficult to grow due to the extreme lattice mismatch, short antimony adatom diffusion lengths, and surfactant effects of antimony [94–96]. Instead, most research groups have grown InAsSb NWs on III-V substrates, which eliminates one of the major NW

advantages over bulk structures. A possible solution is to use another III-V material with a closer lattice constant to silicon as a 'stem' [97,98]. The stem is grown before the InAsSb segment and can help improve vertical NW yield by bridging the lattice mismatch.

J. Svensson et al began experimentally characterizing the diameter dependence of InAsSb NWs grown on InAs substrates [99]. They found that large diameter InAsSb NWs (>500 nm) had a photocurrent peak in the 3-5 µm MWIR region. Corresponding to those peaks were absorptance peaks found in simulations of similar NW arrays. They concluded that the photocurrent peaks were due to light coupling to HE_{11} modes in the NWs. These results are similar to simulations performed previously (Figure 1.11). However, Svensson used randomly positioned NWs with large diameter ranges. Further characterization is required with position- and size-controlled NW arrays.

M. Thompson et al fabricated low dark current InAsSb p-i-n photodiodes on silicon using an InAs stem [100]. The room temperature dark current for a 200-NW array was 18 pA at a bias of -0.1 V. They attribute the low dark current to a small electrical cross-sectional area in the NW and high crystal quality. However, the p-i-n junction in these NWs were axial instead of radial. As stated previously, a radial junction can increase the IQE of the photodetector.

1.5 Thesis Overview

This thesis begins with an overview of characterization methods in Chapter 2. It includes crystal and morphological characterization of NWs by electron microscopy, spectroscopic absorptance in IR and by Raman, and electrical characterization by an IV probing station. Chapter 3 discusses the methods used to fabricate NWs. It includes molecular beam epitaxy (MBE), pre-deposition steps (patterning, etching), and all device fabrication steps following deposition such as photolithography and sputtering. Chapter 3 also contains a parameter study for the improvement of dry etched roughness in polymer films, as it relates to fabricated IR devices. Chapter 4 compares several growth modes of InAs NWs on silicon substrates to identify high vertical yield conditions and study morphological changes with growth parameters. This analysis was published previously in the Journal of Crystal Growth [101]. Chapter 5 defines a model that finds conditions for high yield SAE InAs NW growth in MBE by considering various hole filling scenarios. This work was published previously in Nanotechnology [102]. Chapter 6 discusses the fabrication, characterization, and simulation of multispectral SWIR-absorbing NWs using the InAsSb material system. A novel heterojunction design was used to create large-diameter NWs on a silicon substrate. IR absorptance measurements of various NW arrays were compared to simulated HE_{11} resonances in equivalent NW arrays. It experimentally validates multispectral SWIR photodetection using InAsSb NWs. This work has been published in Nano

Futures [103]. Finally, conclusions and future work are discussed in Chapter 7 for improved Sb-based IR photodetection.

2 Characterization Methods

2.1 Electron Microscopy

One of the vital characterization methods to this thesis is electron microscopy. Electron microscopy enables the user to view features below the fundamental resolution limit of visible light microscopes. It also allows for compositional and crystal structure analysis down to an atomic scale. Specifically, scanning electron microscopy (SEM) was used to observe morphological and topological characteristics while transmission electron microscopy (TEM) was used to extract compositional and structural information.

2.1.1 Principles

Surpassing the resolution limitations of optical microscopy requires a decrease in illuminating wavelength according to the Rayleigh criterion [104,105]. The Rayleigh criterion defines the smallest resolvable distance in a microscope depending on the incident wavelength λ and the numerical aperture NA of the focusing lens.

$$\delta = \frac{0.61\lambda}{\mathrm{NA}} \tag{2.1}$$

Numerical aperture is the range of angles where light can be collected or emitted in a lens and is given by $\mathrm{NA} = \mathrm{n}\sin(\theta)$. n is the index of refraction and θ is the maximum angle in which light is collected. With an ideal NA of 1 the

minimum resolvable feature in an optical microscope is approximately 300 nm, which is too large for nanoscale research. Electron microscopes allow us to surpass the limitations of an optical microscope.

In 1925, Louis de Broglie proposed a wave-particle duality nature of all matter with a wavelength λ dependant on the momentum p of the object:

$$\lambda = \frac{h}{p} \tag{2.2}$$

where h is Plank's constant. Electrons with mass m_o, and elementary charge e that are accelerated in a vacuum with a voltage V have momentum:

$$p = \sqrt{2m_o eV} \tag{2.3}$$

Thus, the wavelength of an electron is controlled by its accelerating voltage in electron microscopes. Correcting for relativistic effects at high accelerating voltages, Equation 2.2 becomes:

$$\lambda = \frac{h}{\sqrt{2m_o eV\left(1 + \frac{eV}{2m_o c^2}\right)}} \tag{2.4}$$

where c is the speed of light in vacuum (2.998 x 10^8 m/s). SEM operation typically occurs in the 1 keV – 30 keV range which has a wavelength-limited resolution on the order of Angstroms. However, practical resolutions are on the order of nm due to volumetric interactions between the electron beam and the sample. TEM typically has much higher accelerating voltages (100 keV – 300 keV). Thus, electron

microscopes are not diffraction limited by the wavelength of incident electrons. Instead they are limited by spherical, chromatic, and astigmatic aberrations in the electromagnetic lenses.

When the primary electron (PE) beam is incident on a sample in electron microscopy there are several possible interactions shown in Figure 2.1. Secondary, backscatter, and Auger electron interactions are typically used during SEM while X-rays, forwardscatter and transmitted electrons are used during TEM.

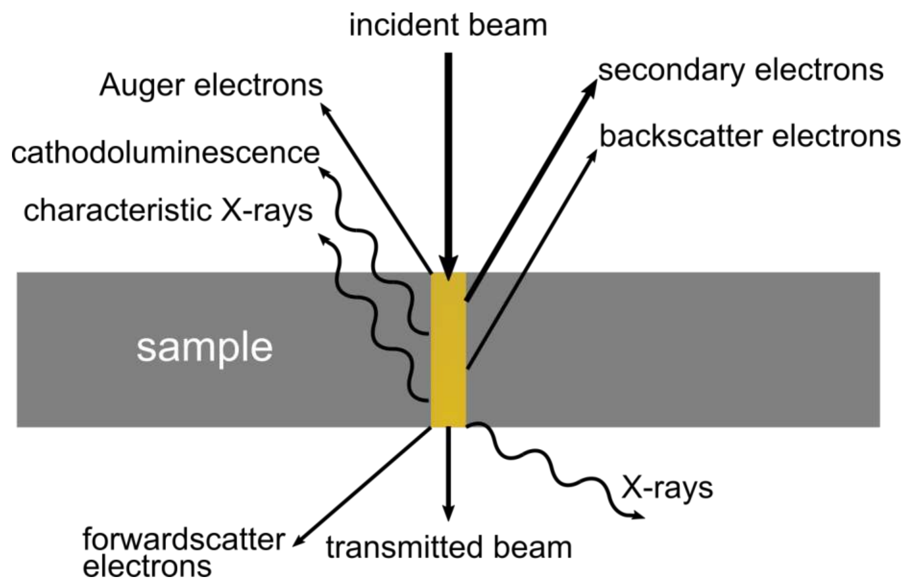

Figure 2.1: Interactions of a high energy beam of electrons within a semiconductor sample. Interactions below the sample only occur when it is sufficiently thin (TEM). Interactions above mostly pertain to bulk samples in SEM.

2.1.2 Scanning Electron Microscopy (SEM)

Secondary electrons (SE) are the primary interaction for SEM imaging. The PE beam is raster scanned over the surface of the sample using a set of deflection plates. Low energy SE are produced when valence shell electrons are inelastically

scattered from the primary beam. Due to their low energies, SE can only be collected within tens of nanometers of the surface. Contrast in SE comes from height and angle differences on the sample due to the proximity to the detector. Thereby making SEM a topological characterization method. Backscattered electrons are produced when high energy electrons in the primary beam are elastically scattered backwards (reflected) due to Coulomb forces from the nucleus of the atom. The probability of backscattering is related to the size of the nucleus, and therefore the atomic number (Z) of the atom. A higher probability of backscattering in high Z atoms increases the image contrast and conversely for a lower probability in low Z materials. In this way, backscatter detection can highlight compositional changes in a sample.

The JEOL 7000F SEM was used extensively in this thesis. Often the NWs being characterized had feature sizes that were beyond the capabilities of an optical microscope, and the topological features (facets, tilt, etc.) would be completely unobtainable with visible light. Typical SEM parameters were 1-10 keV acceleration voltage, ~100 pA beam current, and a working distance of 6-8 mm.

Sample mounting is a very important part of SEM imaging. Improperly mounted samples can lead to sample charging and reduced image quality [106]. Samples were mounted to aluminum stubs, which were attached to a sample stage and loaded into the SEM loading chamber. The mounting method and stub depended on the desired image. When working in plan view or up to 45° tilt, a flat stub with copper clips was used to mount the sample. A 45° tilted stage was used

to achieve higher angles, primarily for cross-sectional (90°) images. These were mounted with double sided carbon tape and/or carbon paste. Carbon paste was used for higher quality or higher magnification (>100,000x) imaging to help sufficiently ground the sample. Samples such as polymers, photoresists, and oxides were also imaged in SEM. A sputter deposited gold layer (~3 nm) was added to improve the conductivity of these insulating samples and thus improve image quality.

2.1.3 Transmission Electron Microscopy (TEM)

High accelerating voltages (>100 kV) and thin samples (~100 nm) allow the PE beam to transmit. Electrons not scattered or otherwise lost make up the transmitted beam, which impinges on a phosphor screen or CCD camera creating a bright field (BF) TEM image. Thickness, composition, crystal structure, and defects produce contrast in a BF TEM image since these affect the scattering of the PE beam. Dark field (DF) TEM captures other electrons not captured in BF TEM. The scattered electrons are focused on the phosphor screen or CCD camera and the directly transmitted beam is blocked with an aperture. For DF images, the resulting image is dark where the beam easily transmits and bright where the beam scatters. Other TEM imaging techniques used in this thesis include: high resolution (HR) TEM, selected area electron diffraction (SAED), scanning TEM (STEM), high angle annular dark field (HAADF), and energy dispersive X-ray spectroscopy (EDS).

High resolution (HR) TEM relies on Bragg reflections through the crystal lattice to form spots and fringes that identify the atomic columns indirectly. One must consider TEM spot size and aberration corrections to directly relate the fringes to atomic columns. This mode reveals information about crystal phase and dislocations in a crystal lattice. HR TEM is usually coupled with SAED. SAED creates a 2-dimensional diffraction pattern that contains information about the crystal lattice including its crystallographic orientation, stacking defects, and crystal structure (ZB, WZ, polycrystalline, etc). Similar information can be extracted from a HR TEM image by taking the fast Fourier transform (FFT) of a specific area.

STEM can be used to raster scan across the sample to achieve a high resolution limited by the probe size. Detectors without spatial recognition may be used in STEM mode since the raster technique accurately defines the position of the PE beam. HAADF is one such detector. It is ring-shaped and designed to capture high angularly scattered electrons from nuclei in the sample. Thus, HAADF is a high resolution and highly Z-sensitive technique. Contrast is seen between atoms/materials with different Z.

Energy dispersive X-ray spectroscopy (EDS) takes advantage of the characteristic X-rays that are emitted by the sample during scattering. Since scattering occurs in inner orbitals, electrons relax into the ground state quickly and emit a photon with a wavelength in the X-ray range. The wavelength of the X-ray depends on the orbital transition which is specific to the excited atom. The wavelength (energy) of the X-ray is measured in a silicon detector giving

characteristic energy counts for most chemical elements. In this way, a quantified composition can be found using EDS.

A JEOL 2010F operated at 200 kV was used to capture all TEM images in this thesis and to perform EDS analysis to find chemical compositions. The EDS detector is a Si(Li) polymer window detector from Oxford instruments (Moxtek AP3.3) with a detection limit of 1 at%.

2.1.4 TEM Sample Preparation

A TEM sample must be thin (~100 nm) to allow beam transmission and avoid chromatic aberration effects [104]. Some NWs in this thesis, such as in Chapter 4, were grown this thin, allowing for a simple drop-cast method for sample preparation. Others, such as in Chapter 6, were too thick for TEM and required focussed ion beam (FIB) or ultramicrotome preparation.

To drop-cast NWs, a small piece of sample was cleaved and placed in a vial with semiconductor grade isopropyl alcohol (IPA) as a suspension fluid. The vial was sonicated for 3 – 10 minutes causing the NWs to break off and suspend in the IPA. A micropipette was used to drop-cast a 2 µL drop onto a holey carbon TEM grid. The drop was allowed to dry for a few minutes before repeating the process 10 – 15 times, after which a low density of NWs was left lying on the TEM grid.

FIB prepared samples were used to look at NWs in a vertical cross-section cut along the length of the NW. FIB was performed by a technician in the CCEM using a Zeiss SMT NVision 40 SII CrossBeam system. In FIB, Ga^+ ions form a beam

column impingent on the sample at 54°, which sputter (mill) sample material. The raster scan capabilities plus the included SEM means the sample can be milled accurately to a small region of interest, such as a row of NWs. The FIB is also able to deposit platinum and carbon precisely through the dissociation of precursor gases. Generally, carbon is used to fill gaps in a sample to increase its rigidity, and platinum is used to weld (mount) the final lamella.

Figure 2.2 outlines the FIB lamella fabrication process. First, a region of interest is selected using the SEM. The technician adds guidelines to help visualize the thickness of the lamella while it can still be viewed from the top. Next, a conformal carbon layer is deposited on the region of interest to fill in the space between the NWs (Figure 2.2b), and then a platinum capping layer is deposited to completely encapsulate it (Figure 2.2c). Trenches are milled all around the region until it is almost disconnected from the substrate. A micromanipulated tungsten probe is welded to the lamella before it is completely removed. The lamella is then welded to a TEM post using platinum and the probe is removed (Figure 2.2e). Finally, the lamella is thinned to ~ 100 nm for TEM analysis. In some cases, (Figure 2.2f) the lamella exceeds the nominal length of approximately 7 µm. Instead of thinning the entire lamella, a thick post may be left in the centre to help increase rigidity.

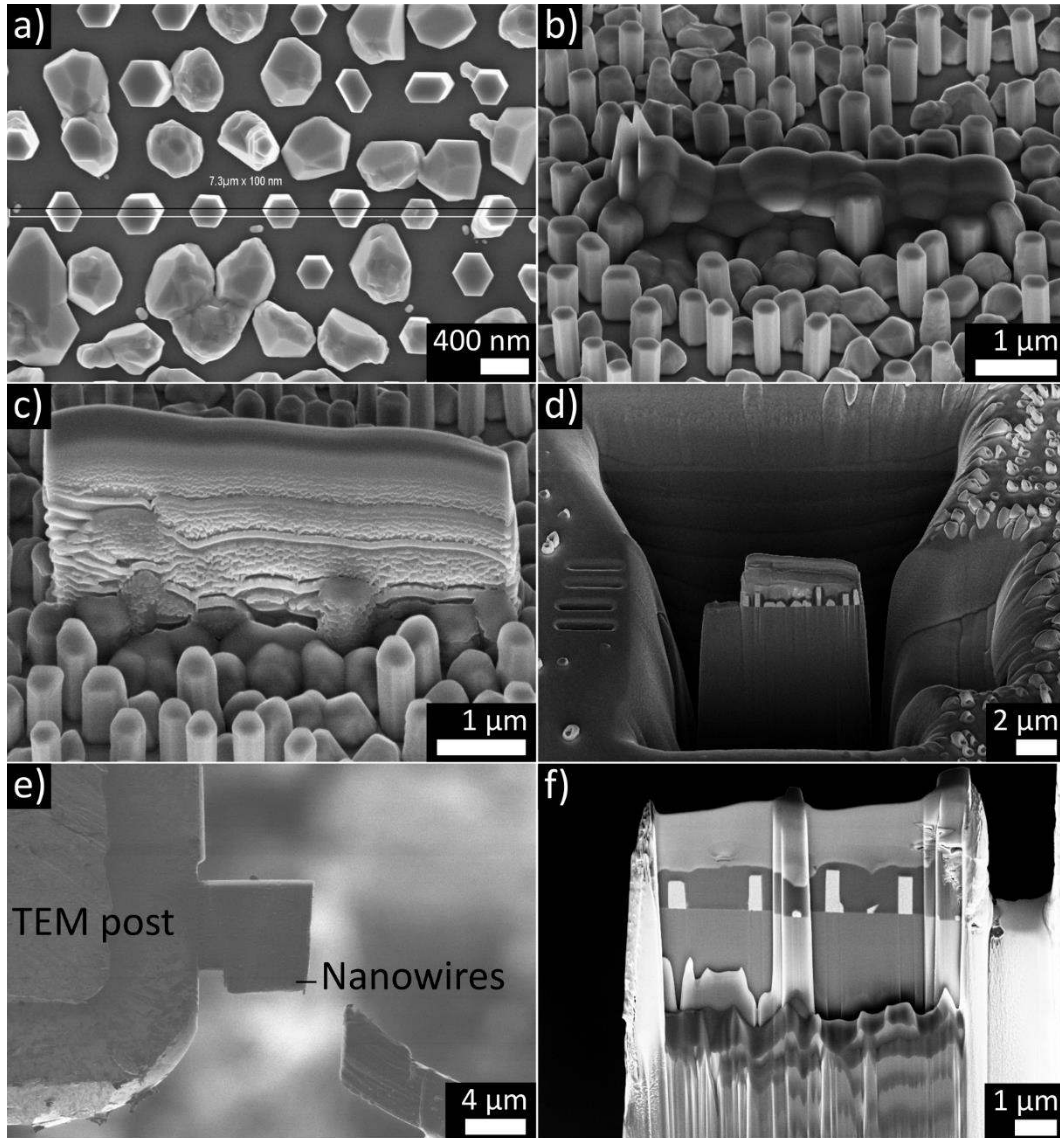

Figure 2.2: Process for creating a NW array cross-section using a focussed ion beam system. a) Area of interest is selected, b) a conformal carbon layer is deposited in situ, c) a platinum capping layer is deposited in situ, d) trenches are milled around the NWs, e) the lamella is attached to a TEM post using a platinum weld, f) the lamella is thinned to ~100 nm for TEM analysis. Images taken by Travis Casagrande from the CCEM.

Ultramicrotome prepared samples were used to examine NWs in a horizontal cross-section through the diameter of the NW. Ultramicrotome was performed by a technician in the Electron Microscopy Facility of the Faculty of

Health Sciences using a Leica Ultracut UCT ultramicrotome. Samples were embedded into hard Spurr's epoxy resin and polymerized before being cut at a glancing angle by a diamond blade. The thin sections (50 – 100 nm) were placed on a TEM grid for analysis. Figure 2.3a shows an ultramicrotome cut NW array in BF TEM. The order of the NW array can be seen in contrast to the surrounding disordered NWs. The rough top edge is where the diamond blade met the substrate due to its glancing angle. Horizontal cross-sections were primarily used to study the core-shell NWs in Chapter 6.

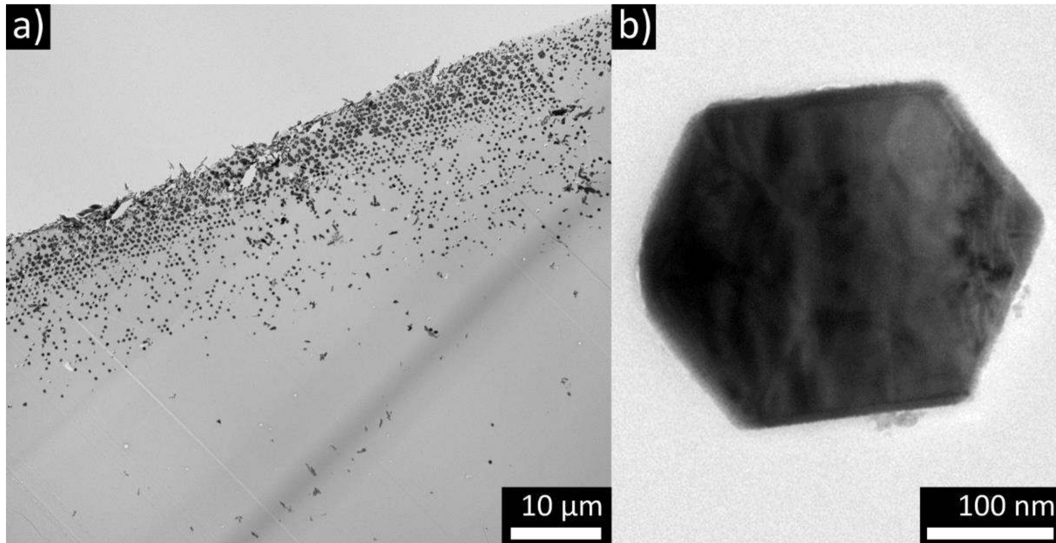

Figure 2.3: Ultramicrotome horizontal cross-section of NWs in BF TEM. a) View including most of a NW array with an evident angular cut. b) Close up of single NW.

2.2 Atomic Force Microscopy (AFM)

AFM is a 3-dimensional scanned imaging method with high spatial resolution. In imaging modes it is used to create 3-dimensional surface

reconstructions with high resolutions in the vertical (1 Å) and lateral (10 Å) directions [107]. These resolutions are due to fine tipped probes and well-controlled piezoelectric feedback loops.

Three main modes of operation exist for imaging in an AFM; contact mode, non-contact mode, and tapping mode. In contact mode the probe is scanned across the sample surface in close contact, less than 0.5 nm between the probe tip and the surface. At this distance, repulsive van der Waals forces will deflect the probe tip as it is scanned across the surface. Z contrast in the image is produced by changes in the probe deflection thereby reconstructing a profile of the sample. In non-contact mode the probe is scanned a few nanometers above the surface. At this distance, attractive van der Waals forces deflect the probe. Tapping mode is a hybrid between contact and non-contact modes. Here the probe is oscillated at its natural frequency and a constant amplitude. The probe is scanned across the surface, gently tapping as it moves. As the surface profile changes, the oscillation amplitude changes producing z contrast in the resulting image. Tapping mode is exclusively used in this thesis, and so the other modes are not discussed further.

Tapping mode is often used because it is the fastest and highest resolution mode as well as being less destructive than contact mode. To operate in tapping mode, a sharp AFM tip is loaded onto the piezoelectric tuner and placed over a sample. A laser is aimed at the back of the cantilever and the reflected spot is aligned to the center of the four-quadrant photodiode. The optical path, shown in Figure 2.4, provides feedback to the electronic system. As the cantilever

resonates, the laser spot moves between the upper and lower sections of the photodiode, which is read out as a sine wave with a set amplitude. The amplitude is driven by the piezoelectric tube attached to the cantilever at its natural frequency. As the sample topography changes, the amplitude read out by the photodiode will change and create contrast in the reconstruction. Small amplitude modulations are detected using a lock in amplifier.

Lateral resolution of the AFM is limited by the diameter and aspect ratio of the cantilever tip. Features smaller than the diameter of the tip can still have an accurate height in the amplitude image, however, there will be a projection of the lateral dimensions of the tip over the feature location. This also applies if contamination is picked up by the tip during a scan. Therefore, sample and tip cleanliness are critical for obtaining a high-resolution AFM image. Aspect ratio (length/diameter) of tips will also limit the resolution, especially when imaging nanoholes. In Figure 2.4 the common pyramid-shaped tip is depicted. The tip easily fits in the large nanohole but is not able to reach the bottom of the small nanoholes. Also, as the tip is scanned across an upslope or downslope the image will contain a projection of the back and front tip angles. Thus, an appropriate tip must be selected for accurate sample imaging.

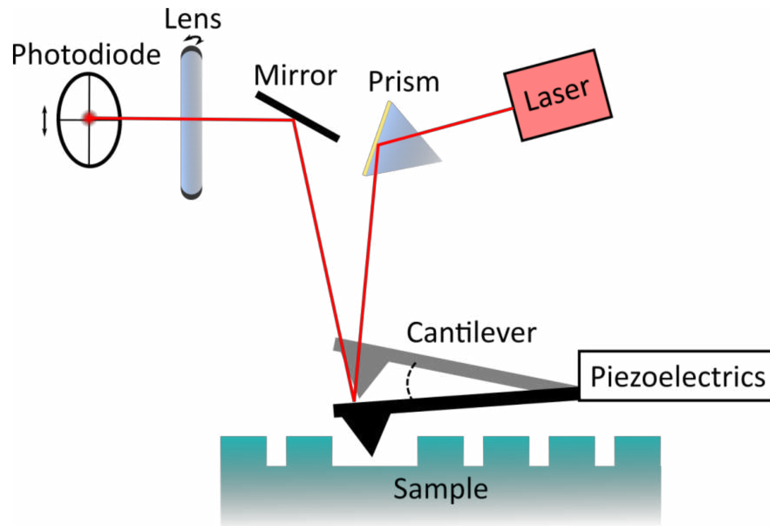

Figure 2.4: AFM tapping mode operation. Laser is aligned through a prism to the back of the cantilever. Reflected laser spot is captured in an aligned photodiode.

Roughness of the surface can be extracted from the amplitude profile [108]. If there are n data points in the reconstruction, each with height deviations of z from the mean line then RMS roughness can be calculated:

$$R_{RMS} = \sqrt{\frac{1}{n}\sum_{i=1}^{n} {z_i}^2} \qquad (2.5)$$

RMS roughness is the mean line (or surface) that divides the profile such that the sum of the squares of the height deviations from it will be zero. It is sensitive to large deviations from the mean. The arithmetic average roughness is the average absolute deviation of the measured heights:

$$R_a = \frac{1}{n}\sum_{i=1}^{n} |z_i| \qquad (2.6)$$

It better accounts for the absolute size of the peaks and valleys in the data, therefore it is a useful metric for understanding discontinuities in a non-conformal thin film deposited on a rough surface. Typically, $\mathrm{R_a}$ is less than $\mathrm{R_{RMS}}$ for rough films.

AFM measurements were performed using a NanoScope IIIa Multimode AFM from Digital Instruments. Silicon probes from Oxford Instruments (AC160TS-R3) had a three-sided tetrahedral shape, a tip radius of 7 nm, a tip length of 14 µm, a front angle of 0° and a back angle of 35°. The operational software (also named NanoScope) was used to determine resonant frequencies (~300 kHz), to set scan and feedback parameters, and to perform analysis on the images. In Section 3.4 the surface roughness of a polymer is characterized using tapping mode AFM. Typical scan parameters for measuring small surface roughness are summarized in Table 2.1.

Table 2.1: Typical AFM parameters used to measure small surface deviations.

Parameter	Value	Parameter	Value
Scan Size (µm)	1-5	Integral Gain	1
Scan Rate (Hz)	1	Proportional Gain	1.3
Samples/line	512	Look Ahead Gain	0
Z Limit (nm)	250	Amplitude Setpoint (V)	1-2

2.3 Variable Angle Spectroscopic Ellipsometry (VASE)

Ellipsometry is a non-destructive optical technique for characterizing optical constants, thickness, and other material properties. It relies on the change in polarization due to reflections in the material. The precision of the measured

material parameters depends on a fitted model. The thickness of a well-defined sample can be measured precisely to a few Å.

A basic ellipsometer will include a monochromatic light source, polarizer, analyzer, and a detector. Monochromatic, linearly polarized light is incident on the sample surface at a defined angle, such as in Figure 2.5. S- and p- components of the incident light interact with the sample according to the Fresnel equations. In multilayer structures the Fresnel equations apply at each boundary creating a series of reflections. The reflections interfere and have an overall phase shift depending on the thickness and the material properties of the films. In general, a reflected wave will be elliptically polarized due to the phase shifts in the material. The state of polarization can be determined by a rotating polarizer (analyzer). Through a full rotation, the analyzer passes light to the detector according to its polarization state. Intensity as a function of time at the detector is used to extract the relative parameters Ψ and Δ, where:

$$\tan\Psi e^{i\Delta} = \frac{R_p}{R_s} \tag{2.7}$$

and,

$$\tan\Psi = \frac{|R_p|}{|R_s|}, \qquad \Delta = \delta_p - \delta_s \tag{2.8}$$

R_p and R_s are the complex Fresnel reflection coefficients of p- and s- polarizations respectively. δ_p and δ_s are the phase changes for these polarizations. In this way, material properties can be indirectly measured in ellipsometry by directly

measuring phase and magnitude of the reflected signal. Beyond the basic ellipsometer, measuring Ψ and Δ at several angles, in the case of a variable angle ellipsometer, increases the amount of data for fitting thereby increasing the number of possible determinable parameters (and layers). Extending the wavelength range with a spectroscopic ellipsometer further increases the number of determinable parameters.

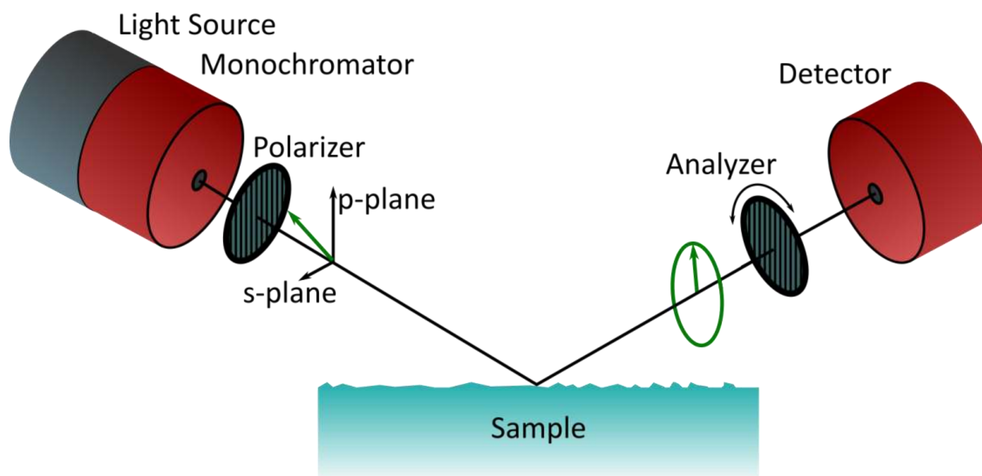

Figure 2.5: Ellipsometer with a rotating analyzer. Incident light is monochromatic and linearly polarized with a component in both the s- and p-planes. Reflected light is generally elliptically polarized.

Ψ and Δ are always measured with extreme accuracy due to the relative nature of the measurement. However, the extracted parameters depend strongly on the model used to fit the data. A model is created in the software by stacking layers of materials with known optical constants to represent the layers of materials in the sample. Initial parameter values are selected, and regression analysis is performed by the software until a minimum mean squared error (MSE) is found. Further decreases in MSE can be obtained by increasing the complexity

of the model and adding roughness, compositional gradients, anisotropy, etc. The minimum MSE usually represents the most accurate model for the data. A good MSE can provide an estimated data error of < 0.01%. However, this is only a software estimate, not an actual representation of the measurement error.

Ellipsometry measurements were performed on a J.A. Woollam M-2000 Variable Angle Spectroscopic Ellipsometer with a normal angular range of 45° - 75°, a wavelength range of 245 nm – 1690 nm, and a 3 mm x 7 mm spot size. This system was primarily used to measure the thickness of deposited oxide films as described in Section 3.1.1. It was also used in Section 3.4 to optimize polymer roughness and thickness. CompleteEASE software was used to perform the measurements and fit models to extracted data.

2.4 Fourier Transform Infrared Spectroscopy (FTIR)

FTIR is a spectroscopic absorption technique that relies on an interferometer to broadband illuminate a sample without the need for diffraction gratings [109]. Spectra are obtained from the resulting interferograms using a Fourier-transform. The benefit is fast scan times (~ 1 ms), a large spectral range (near-IR to far-IR), and a high spectral resolution (0.1 cm^{-1}).

A schematic representation of an FTIR is shown in Figure 2.6 below. A broadband source is passed through a Michelson interferometer which consists of a beam splitter, a stationary mirror, and translational mirror. In the interferometer

the beam is split along two different paths. One reflects from the stationary mirror, passes through the beam splitter and impinges on the sample/detector. The second path reflects off the translational mirror before impinging on the sample. When the two beams recombine at the beam splitter they interfere according to the path difference δ. For each wavelength (or a monochromatic source) a phase difference of the paths is,

$$\Delta = \frac{2\pi}{\lambda}\delta \tag{2.9}$$

where λ is the incident wavelength. Therefore, when δ is an integer multiple of λ the interference is constructive, and all the light is directed to the sample. When δ is a half integer multiple of λ the interference is destructive, and no light reaches the sample. An interferogram is created by scanning the translational mirror and measuring intensity as a function of mirror position. A spectrum is recovered from the interferogram with a Fourier transform [110]. The spectrum is often expressed as absorbance as a function of wavenumber (inverse wavelengths in cm^{-1}). Absorbance, not to be confused with absorptance, is a transform of transmittance or reflectance according to the Beer-Lambert law.

$$\mathrm{Abs} = -\log_{10}\left(\frac{\mathrm{I}}{\mathrm{I_0}}\right) \tag{2.10}$$

I and $\mathrm{I_0}$ are measured intensities (transmission or reflection) with and without the sample in the beam path, respectively.

Absorptance (A), the physical parameter corresponding with reflectance and transmittance, can be found by measuring transmittance (T) and reflectance (R) directly and considering conservation of energy laws. It represents the absorbed intensity relative to the incident intensity.

$$A + R + T = 1 \tag{2.11}$$

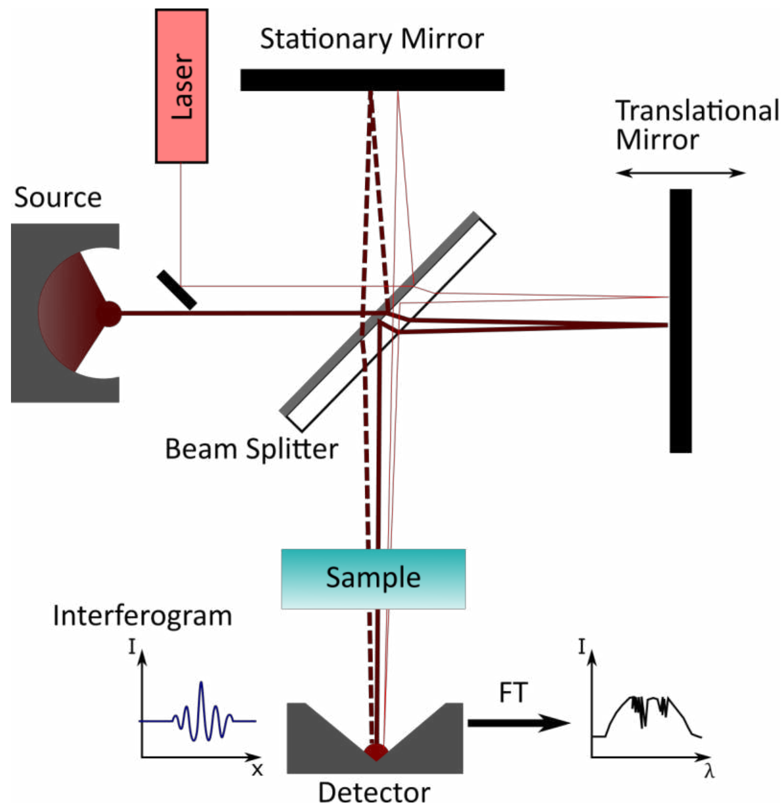

Figure 2.6: FTIR Michelson interferometer beam path with broadband source. Interferogram incident on the sample is converted to a spectrum with a Fourier transform. Mirror position is measured directly with HeNe laser.

A Helium-Neon (HeNe) laser is added to the beam path through the interferometer. It measures the path difference in real time to ensure a high

accuracy and precision of the mirror position. According to the Nyquist sampling criterion, sinusoids need to be sampled at twice their frequency to be described accurately, which means the number of data points in the interferogram is limited by the laser wavelength. This sets the maximum wavelength range of the extracted spectrum. Furthermore, the resolution of the spectrum is defined by the maximum path difference between the two beams.

Figure 2.7 shows the configuration of the Bruker Hyperion 3000 microscope attachment to the Bruker Vertex 70v FTIR used in this thesis. The Vertex is responsible for sourcing the interference pattern and can be operated as a self-contained unit. The Hyperion is an attachment to the Vertex system that allows reflectance measurements to be made and focal plane array images to be taken. Both instruments are controlled by Brukers OPUS 7.2 software. Infrared light with a spectral range of 8000 – 600 cm^{-1} (1.25 – 16.6 μm) and a spectral resolution of 2 cm^{-1} is reflected through an interferometer, as in Figure 2.6, before entering the input port of the Hyperion. In reflectance mode, a set of mirrors reflect the light around to a 15xIR objective lens where it is focused onto the sample. Reflected light is captured by the objective lens (NA = 0.4) and directed to the mercury cadmium telluride (MCT) D316-025 single element detector. In transmittance mode, mirrors reflect the light down to an aperture and condenser to focus the light onto the sample. The transmitted light is captured by the objective lens and directed to the MCT detector. A focal plane array (FPA) consisting of 64 x 64 MCT-D364 detectors could also be used to see infrared

images of the sample. Both modes used a knife edge aperture above the objective lens to select a specific region of the sample for analysis. Regions are selected by enabling the visible light mode. Visible light mode is also used to find the reflectance and transmittance background spectra, which include a gold mirror and a stage hole respectively.

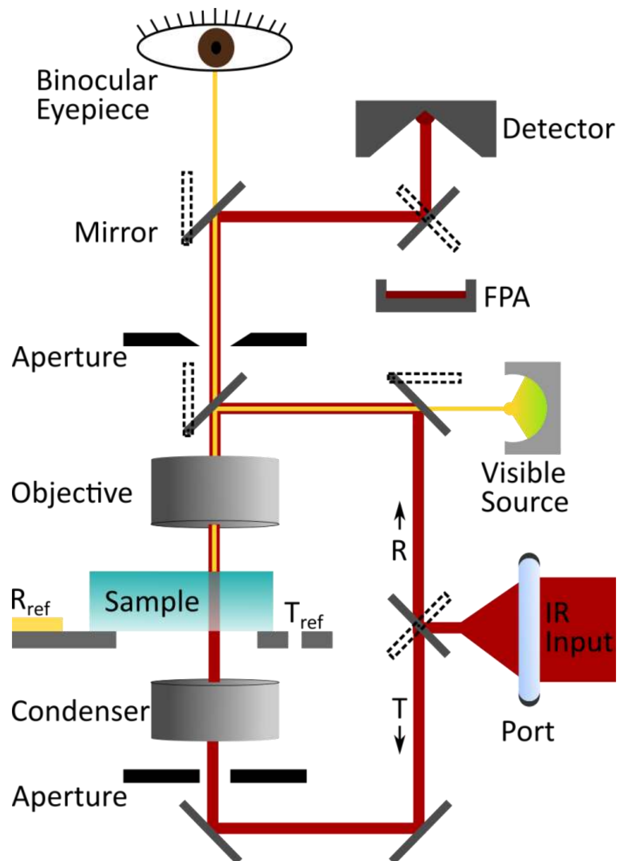

Figure 2.7: Hyperion 3000 beam path for measuring reflectance and transmittance. IR input from the interferometer in a Vertex 70v system. IR reflectance and transmittance paths are indicated by R and T respectively. Alternative mirror positions are indicated with dotted lines.

An obvious complication arises from this microscope setup. Reflectance and transmittance measurements are incident on opposite surfaces of the sample.

In a homogenous, isotropic, and vertically symmetric sample this would be appropriate. However, in the general case, samples do not have identical top and bottom surfaces or symmetrical interfaces throughout their bulk. For example, a sample with a textured top surface and smooth bottom surface will have different reflectances from each of those surfaces. For Equation 2.11 to be accurate the measurements must be made in the same incident direction, which means the sample must be turned over during transmittance measurements. This presents another challenge. Optical alignment to the sample area can only occur through the objective lens and therefore opaque samples cannot easily be aligned for transmittance. Instead, the FPA was used to see through the IR transparent bulk to map the IR absorbing material on the other side.

2.5 Raman Spectroscopy

Raman spectroscopy is a non-destructive characterization technique for material properties such as composition, crystal orientation, and phase [111]. Raman indirectly determines phonon energies in a crystal lattice by measuring the Stokes shift in scattered light.

Monochromatic photons may be scattered from atoms in a solid lattice by elastic or inelastic interactions. Elastic or Rayleigh scattering is when the scattered photon has the same energy as the incident photon. Inelastic or Raman scattering is when the scattered photon has a different energy than the incident photon.

When the scattered photon loses energy, it is referred to as Stokes scattering. When the photon gains energy it is referred to as anti-Stokes scattering. In both cases the energy difference is attributed to phonons in a solid lattice through creation or annihilation.

With photon excitation there are two main (optical) phonon modes: longitudinal (LO) and transverse (TO). In the former, atomic oscillations occur parallel to the direction of propagation, while in the latter they occur perpendicular to propagation. Binary semiconductors all show characteristic LO and TO modes as measured in Raman. Ternary III-V semiconductors often display two-mode behaviour, which means there are two sets of LO and TO modes present in the spectrum. One from each of the binaries. This arises because of the two different masses occupying the same lattice positions (i.e. As and Sb in InAsSb).

A schematic representation of a Raman spectroscopy system is shown in Figure 2.8. In a confocal backscatter Raman system, the sample is excited with a laser incident through a microscope objective lens. Backscattered light (Rayleigh, Stokes, and anti-Stokes) is captured by the microscope objective. A holographic notch filter is used as a mirror along the excitation path and as a filter to remove Rayleigh scattered light along the detection path. A reflective grating is used to spatially separate the remaining Raman wavelengths and a CCD measures the intensity of each wavelength. The CCD measures wavelength but Raman data is typically quoted as a function of Raman shift in wavenumbers.

$$\text{Raman Shift}[\text{cm}^{-1}] = \left(\frac{1}{\lambda_{\text{Laser}}} - \frac{1}{\lambda_{\text{Raman}}}\right) \quad (2.12)$$

where λ_{Laser} and λ_{Raman} are the laser and measured Raman wavelengths, respectively. Data is converted to wavenumbers because they are proportional to energy, and it effectively removes the dependence on laser wavelength.

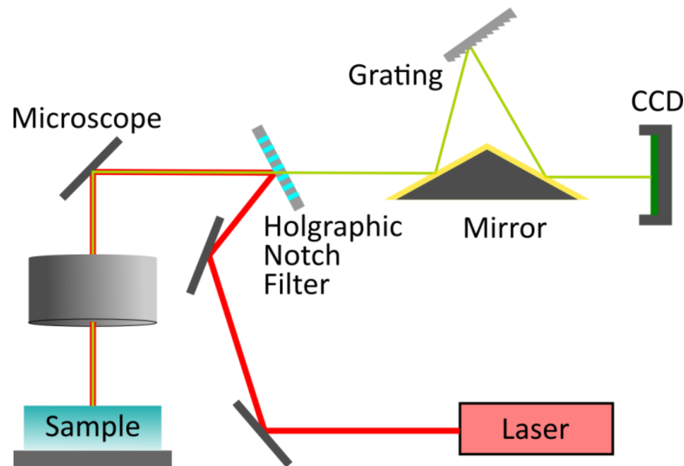

Figure 2.8: Renishaw confocal micro-Raman spectrometer setup. Excitation (laser) beam path is indicated in red and detection (Raman) beam path is in green.

This thesis uses a Renishaw micro-Raman system in the backscatter geometry. A 20 mW Ar^{+} ion laser at 514 nm wavelength excited the samples through a 50x objective lens (NA=0.75) with a 1.5 µm spot size.

2.6 Current-Voltage (I-V) Characterization

I-V characteristics of semiconductors can reveal information about p-n junctions or heterojunctions. Typically, I-V measurements are taken by stepping a bias voltage across the two terminals of the device (p and n), while measuring

current in a four-point probe configuration. I-V curves taken in the dark reveal information about the diode characteristics of the device via fitted diode model. Illuminated I-V responses provide information about the photogeneration in the device. I-V measurements can also be used to verify ohmic contact, and to quantify resistivity of materials.

Electrical measurements were performed using a Karl Suss probing station with four precision manipulated needle probes. A Keithley 2400 sourcemeter simultaneously sourced voltage and measured current as controlled by a Python script. The probe station was surrounded by blackout sheets to allow for dark I-V measurements and a Newport 67005 lamp provided an AM1.5G spectrum. An SLS203L globar source from Thorlabs provided optional infrared illumination with a wavelength range of 500 – 9000 nm.

3 Fabrication Methods

3.1 Pre-growth Preparation

A series of standard preparation steps were followed prior to loading a sample into the molecular beam epitaxy (MBE) system for NW growth. Those steps are summarized here, following Figure 3.1, and explained with more detail in the ensuing subsections. The steps describe the preparations for selective area epitaxy (SAE) growth, which was the most common growth mode in this thesis. Section 4.2 describes other preparation steps required for the less frequent growth modes studied there.

Preparation began with epi-ready 3-inch silicon (111) wafers from Virginia Semiconductor. Depending on the application, wafers were either high resistivity (>100 Ω-cm), or highly boron doped with a low resistivity (>2 x 10^{19} cm^{-3}, <0.005 Ω-cm). All wafers had a micro-roughness below 5Å. New wafers were first loaded into a chemical vapour deposition (CVD) system for growth of a 20 – 30 nm silicon oxide (SiO_x). Next, electron beam lithography (EBL) positioned small holes in a positive electron resist, which defined the location of future NWs. Full wafers were then cleaved into 6 equal-size pie pieces for easier handling. A reactive ion etching (RIE) system was used to transfer the EBL pattern to the underlying oxide. RIE conditions were chosen to leave a thin layer (~5 nm) of oxide in the holes and the EBL resist was lifted off. Finally, a buffered hydrofluoric acid (BHF) etch was

performed immediately before loading into an MBE to remove the remaining oxide from the holes.

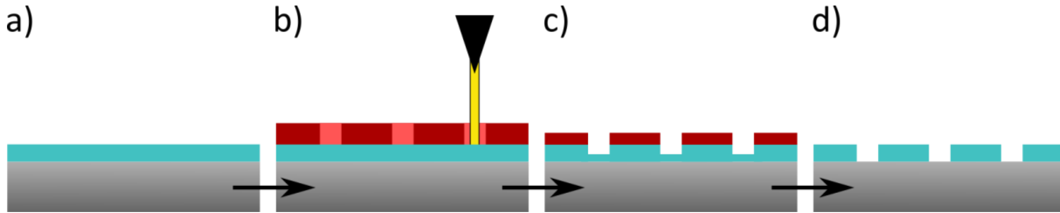

Figure 3.1: Process flow for NW growth preparation. Beginning with an epi-ready wafer (grey), a) a CVD oxide (blue) is grown on top of the wafer, and b) an EBL pattern (red) defines the NW positions. c) RIE etches partway through the oxide in the EBL holes. d) Resist is lifted off and remaining oxide in the holes is removed with BHF.

3.1.1 Chemical Vapour Deposition (CVD)

CVD was used to deposit a thin (20 – 30 nm) silicon oxide on the silicon substrates (Figure 3.1a). The oxide mask is later used to control the locations and growth kinetics of NWs in MBE. This plasma enhanced-CVD from Johnson Ultravac uses a radio frequency (2.455 GHz) generated plasma to dissociate the reactant gases. At the sample surface, a relatively small amount of thermal energy is required to react adsorbed gases and grow an oxide film [112]. A substrate temperature of 500 °C was used to deposit the reactants silane (SiH_4), and oxygen (O_2) for 21 minutes to achieve a 30 nm oxide layer.

3.1.2 Electron Beam Lithography (EBL)

EBL, shown Figure 3.1b, is a process of transferring a designed pattern to an electron beam sensitive resist for a subsequent procedure (deposition, etching,

etc.). The system is like SEM in principle and many SEM instruments are outfitted with simple EBL capabilities. Good instruments have a high resolution (<10 nm), and high stitching accuracy (<50 nm). Both SEM and EBL use a fine diameter electron probe to interact with a sample. The difference between SEM and EBL is that in SEM you want to maximize secondary or backscatter electrons while in EBL these interactions decrease the resolution by exposing surrounding resist. EBL uses a high accelerating voltage (100 kV) to minimize beam spreading and other detrimental volume interactions.

EBL uses a fine diameter electron probe to 'write' a pattern into an electron resist. Analogous to photolithography, there are two types of resist: positive and negative. Polymers are broken down in exposed areas in a positive resist and removed with a developing solution. Polymers are cross-linked and strengthened in exposed areas of a negative resist and therefore remain after development. There is a minimum amount of charge required to sufficiently expose the resist, called dose to clear. The dose that an area of resist receives is measured in $\mu C/cm^2$. Dose to clear is typically around 250 $\mu C/cm^2$ but depends on the thickness of the resist, accelerating voltage, and probe current.

EBL was performed at the University of Toronto Nanofabrication Centre on a Vistec EBPG 5000+ which has a resolution of <10 nm, a 560 x 560 μm^2 field size, and a stitching accuracy of 20 nm. The pattern in Figure 3.2 was created using a 120 nm thick ZEP520A (1:1 with anisole) positive resist. It is divided into three major regions; the top pads that have large vertical separations for fabricating

devices, the large TEM pad, and the bottom pads that have small vertical separations. The top section is written three times for redundancy. The TEM pad is 560 x 560 μm^2 to maximize the number of NWs in a single pad without surpassing the field size. This pad is later cleaved out and used to drop cast NWs for TEM analysis (see Section 2.1.4). The compressed region is meant to make SEM imaging easier by placing all pads close together. In Chapter 4 it was also used to grow Au-seeded NWs concurrently with SAE NWs.

Each square represents an array of dots following the single spot exposure method [113]. This method takes advantage of a finite interaction volume of the probe to produce a uniform array of dots. Each dot is exposed in a single shot from the EBL, which reduces write time when compared to a typical direct-writing technique. The diameter of the dots is defined by the probe current and dose received. An example of the dot array is shown in the top inset of Figure 3.2. The array is spaced triangularly such that each dot is equidistant from its six nearest neighbours. After growth, NWs will have a spacing (period) controlled by these dots, which is measured centre to centre.

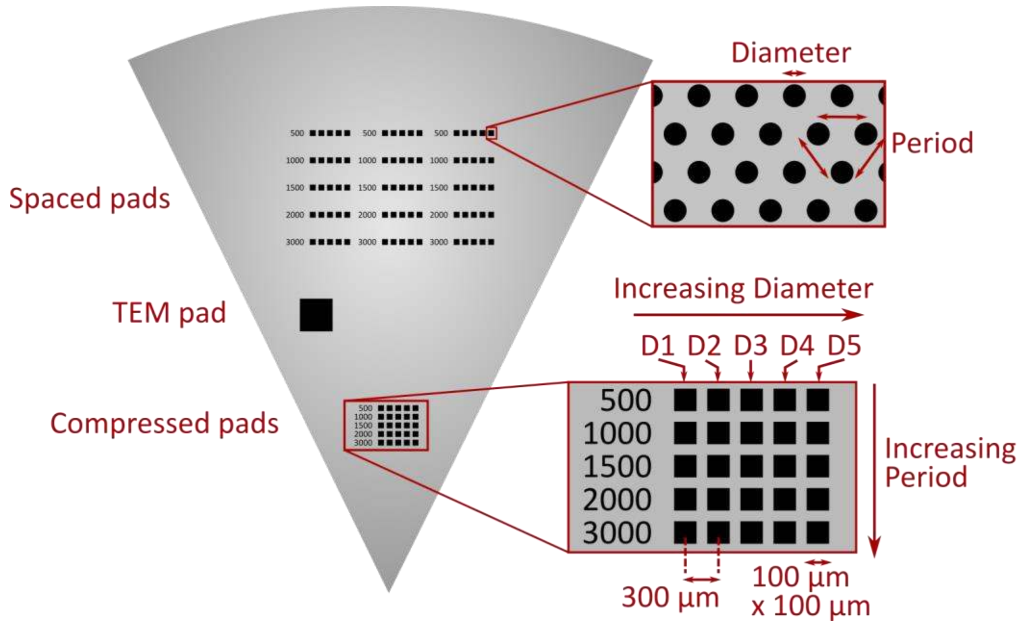

Figure 3.2: Top view of the EBL pattern used in this thesis. Items in black represent real features in the design. Red indicates annotations. Grey represents the cleaved pie piece with a thin CVD oxide. Black squares are NW pads with triangular arrays of patterned dots (Top inset). A magnified view of the compressed region is shown in the bottom inset with indicated diameter and period.

The bottom inset of Figure 3.2 depicts diameter and period trends for the pads. Markers along the left indicate NW period in nm. Period increases along the rows and remains constant along the columns. Diameters increase along the columns and remain constant along the rows. Diameter values are not marked in the pattern itself due to the variable dependence on etch conditions and times. They are instead referred to as D1 through D5, which have the nominal corresponding values in Table 3.1 below. Resulting hole diameters are larger than the patterned resist diameters due to undercutting in the subsequent oxide etching steps.

Table 3.1: Diameter labels with corresponding EBL parameters and hole diameters.

Label	Probe Current (nA)	Dose ($\mu C/cm^2$)	Resist Hole Diameter (nm)	Oxide Hole Diameter (nm)
D1	0.5	10,000	22	65
D2	1	10,000	30	65
D3	5	10,000	48	65
D4	25	13,000	70	85
D5	25	25,000	83	95

3.1.3 Reactive Ion Etching (RIE)

RIE is a dry etching technique that combines physical bombardment and chemical reactions to etch a sample material (Figure 3.1c). A radio frequency (RF) generated plasma is responsible for creating bombarding ions and chemically reactive radicals. With precise control of etching parameters (power, pressure, gases, etc.) it is possible to etch materials anisotropically, in contrast to the isotropic nature of wet chemical etching.

There are two main types of RIE systems; capacitively coupled plasma (CCP), and inductively coupled plasma (ICP). In CCP a chemically reactive gas is injected between two parallel plates. An RF bias applied across the plates creates an avalanche breakdown effect and generates ions, electrons, and radicals. A correlated DC bias accelerates ions toward a sample placed on the cathode. Both physical bombardment and chemical reactions occur at the sample surface and work to remove material while a vacuum pumps out volatile products. In ICP the plasma generation and ion acceleration are decoupled allowing for more precise control of etching parameters. CCP-RIE was used most often in this thesis and,

although ICP-RIE has many advantages (high plasma densities, low pressure operation, better anisotropy), it is not discussed further.

There are three main interactions within a plasma [114]. The first is ionization of the gas to produce electrons and positively charged ions, which maintain the plasma. The second is the excitations of gas molecules to higher energy vibrational, rotational, or electronic states. This leads to a characteristic glow in the plasma with an intensity proportional to the density distribution of electrons. The final reaction is dissociation of gas molecules into free radicals. Radicals are very chemically reactive and are responsible for several etching processes at the sample surface.

Plasmas may etch a sample via one or combinations of the processes shown in Figure 3.3. One etch method is to physically sputter sample material with the high energy ions, which works anisotropically. The second method is a simple chemical reaction between the gas (or reactants from the plasma) and the sample to produce volatile molecules. The volatile products typically have a high vapour pressure such that it enters the gas phase and is pumped out through the vacuum. Ion enhanced chemical etching (Figure 3.3c) combines both of the first two processes; kinetic energy of the ions accelerates volatile product removal. Inhibitor driven ion enhanced etching is a subset where all surfaces are passivated by a thin reactant or product layer. Anisotropic ion bombardment removes the layers on the horizontal surfaces but is unable to remove the layers on vertical surfaces, thereby passivating the sidewalls and creating an ideal anisotropic etch.

This is the method of etching silicon oxide in a C_xF_y plasma for nanohole patterning in this thesis [115]. Neutral C_xF_y molecules deposit a thin polymer layer on the oxide surface and a steady state polymer thickness is reached. Etching of the oxide occurs between the solid polymer and the oxide surface, which produces SiF_yCO_2. This dissociates to SiF_y and CO_2 via ion sputtering and is pumped out through the vacuum. The polymer thickness is balanced between ion activated polymer deposition, and fluorine atom chemical etching (and ion sputtering).

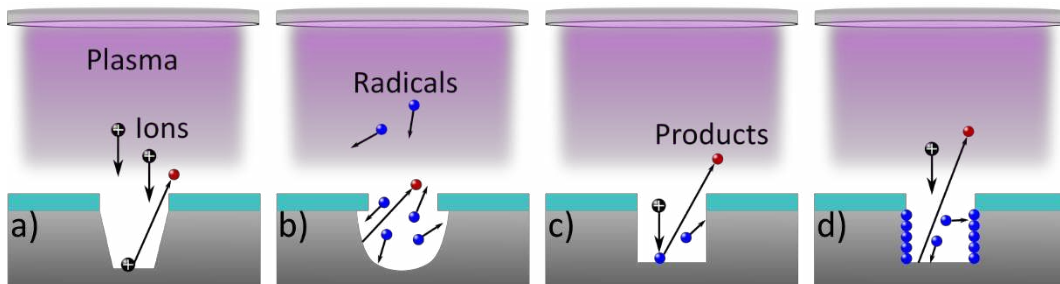

Figure 3.3: Cross-sectional view of RIE reactions. a) Physical sputtering, b) chemical etching, c) ion enhanced chemical etching, and d) inhibitor driven ion enhanced etching. Etched sample is shown in grey and an etch mask is in light blue. Black spheres are ions, blue are radicals, and red are volatile products.

There are several important parameters in CCP-RIE: power, chamber pressure, gas composition, and temperature. RMS power directly affects the DC bias and ion density. Increasing either will result in a higher etch rate; however, an increased DC bias will also increase the directionality, and decrease selectivity. Chamber pressure is inversely proportion to the directionality of the etch. Generally, a low pressure is desired for anisotropic etches. Many etches use multiple reaction gases or additives like O_2, N_2, or Ar. Depending on the specific

chemistry, the ratio of these reactants can affect etch rate, selectivity, and roughness. Substrate temperature affects the chemical reactions. Increased temperature can increase the isotropic etch rate, but it often decreases the selectivity.

When etching nanoholes, microloading and aspect ratio dependent etching (ARDE) effects can become significant. Microloading is the local etch rate dependence on exposed surface area on a substrate [116]. Densely packed features will etch at a slower rate than isolated features. The effect arises from the local depletion of etchant gases. ARDE is an effect seen when etching features smaller than 1 micron. Small features will etch at a slower rate than large features. The effect is exacerbated at high aspect ratios and is due to local differences in ion/neutral ratios in small holes where directional ions can enter small features unimpeded while neutrals supply decreases. For every period-diameter combination in our EBL pattern (Figure 3.2) there is a different nanohole etch rate due to microloading and ARDE.

The RIE used to etch nanoholes in this thesis was a Technics Micro CCP-RIE series 800. Plasmas were generated with an RF power supply operating at 13.56 MHz. Nanoholes were etched in a silicon oxide growth mask patterned by EBL. Typical parameters included 10 sccm of CF_4, RF power of 100 W, and a chamber pressure of 320 mTorr.

3.1.4 Buffered Hydrofluoric Acid (BHF)

BHF was used to remove the remaining oxide in the patterned nanoholes before loading into an MBE (Figure 3.1d). Removing the oxide layer exposes the substrate surface for the NWs to nucleate growth. BHF is a solution of hydrofluoric acid (HF, 49%) buffered with ammonium fluoride (NH_4F, 40%) in a ratio around 7:1 (NH_4F : HF), and diluted with deionized water 10:90 (NH_4F/HF : DI). It is also known to passivate silicon (111) surfaces with hydrogen bonds, which inhibits native oxide regrowth for up to 100 minutes [117]. Samples in this thesis were etched in further dilute BHF solutions at 10:1 (DI : BHF) to slow the etch rate. A dilute BHF etch was performed immediately prior to loading for all growths with an etch duration of 25 – 35 seconds.

3.2 Growth in Gas Source Molecular Beam Epitaxy (GS-MBE)

MBE is a method of high crystal quality deposition through thermal evaporation. In MBE a crystalline film is deposited epitaxially on a substrate with the ability to create atomically abrupt interfaces. It achieves this level of precision by operating in a molecular flow deposition regime. Molecular flow occurs in a high vacuum environment when the mean free path of depositing gas species is larger than the chamber length; i.e. there are no collisions along the deposition path. This, coupled with fast mechanical shutters, gives high precision abrupt layers. Impurities are mitigated by operating in an ultra-high vacuum (UHV)

environment (10^{-9} Torr), and liquid nitrogen cooled cryopanels trap material species that are desorbed from the substrate or elsewhere in the chamber.

Materials are typically sourced from an effusion cell. Effusion cells contain highly pure elemental source materials (e.g. Ga, In, Al) in a boron nitride crucible wrapped in a resistive molybdenum coil heater. Heated source materials build up a pressure differential relative to the chamber and flow out through a cavity directed at the substrate. Fast mechanical shutters (one for each effusion cell) controls elemental flow to the substrate. In a gas source MBE, like the one at McMaster, arsenic and phosphorus are supplied in hydride form and thermally decomposed (cracked) in a cracker cell. Instead of an effusion cell, the materials are stored externally in the gas phase, allowing for easy material replenishment. GS-MBE also allows the user to select for dimer or tetramer forms of the gas species by changing the cracking temperature.

McMaster's GS-MBE system is from SVT Associates and is operated by Shahram Tavakoli of the Engineering Physics Department. An illustration of the system is shown in Figure 3.4. Samples are loaded into a molybdenum holder that is inserted into the loading chamber. The loading chamber acts as a vacuum barrier between atmospheric pressure and the degas chamber by reaching 10^{-7} Torr. Samples are transferred to the degas chamber where they are heated to 300 °C to remove atmospheric gases that have adsorbed onto the substrate surface. Finally, samples are transferred into the UHV deposition chamber on a heated rotating stage with the deposition surface facing down. Effusion cells are at the bottom of

the chamber at a 33° angle to the sample surface normal. During deposition, solid source material is released from the heated effusion cell through a shutter and impinges on the rear heated sample. Heat is controlled via a thermocouple on the back of the sample and a pyrometer pointed at the front. Gas source materials flow through a cracker cell operating at 950 °C. Due to the low sublimation temperature (550 °C) and high thermal decomposition temperature (900 °C), antimony is sourced from a special three-stage effusion cell. The reservoir (Figure 3.4) is heated to 565 °C to sublimate the solid antimony material. A mechanical needle valve controls the flow of gaseous antimony out of the reservoir. It is also heated (800 °C) to mitigate condensation. In the third stage antimony is heated to thermal decomposition (930 °C) so that most of the gas is Sb_2.

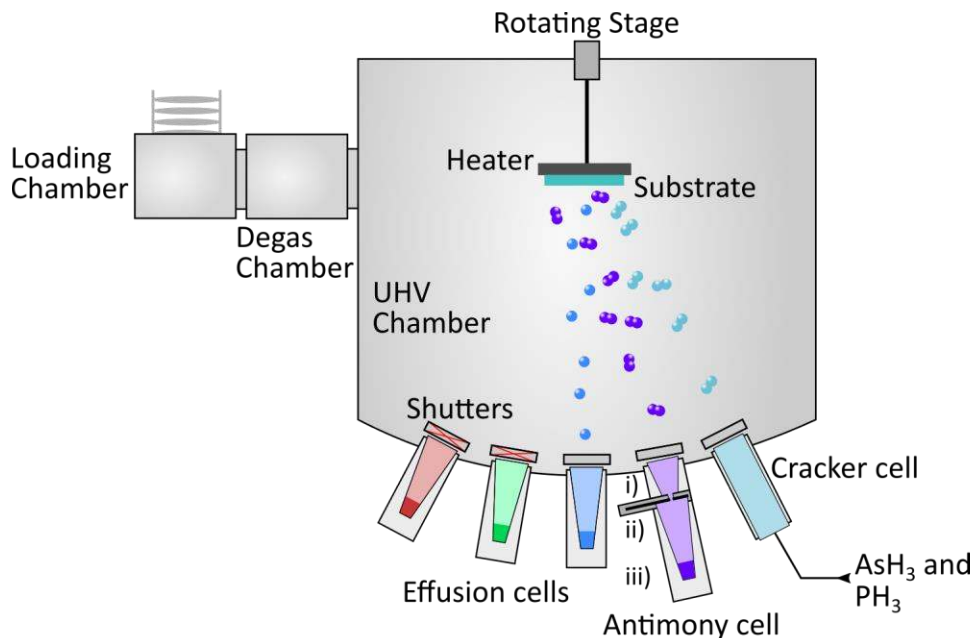

Figure 3.4: Illustration of main GS-MBE components for the system at McMaster University. Three-stage antimony effusion cell is indicated with i) thermal cracker stage, ii) heated needle valve, and iii) reservoir.

3.3 Post-growth Device Fabrication

After growing NWs in the MBE, a series of standard processing steps were followed to fabricate a photo-responsive device. Those steps are summarized here, following Figure 3.5, and explained with more detail in the ensuing subsections.

Newly grown NWs were always imaged in SEM to measure yield. Once complete, NWs were planarized with a rigid and chemically resistive polymer, benzocyclobutene (BCB). BCB was thinned to reveal the tips of the NWs using RIE. Next, a photolithography step left photoresist windows above the individual NW arrays. A transparent conductive film was deposited by sputtering and the photoresist was lifted off leaving the transparent conductor in contact with the NWs. Next, a second photoresist layer covered the transparent windows and defined a series of contact pads. Electron beam evaporation was used to deposit opaque contacts for the large contact pads. Finally, an aluminum contact was deposited across the back of the entire sample (Si substrate) by sputtering, and the device was annealed by rapid thermal annealing (RTA).

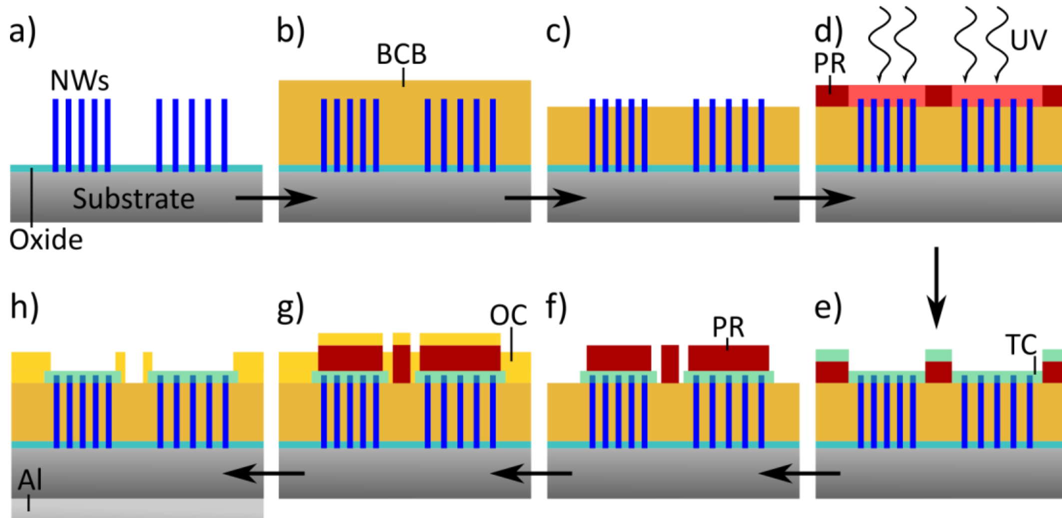

Figure 3.5: Device fabrication process for NW arrays. a) Extracted NWs with indicated oxide layer are imaged in SEM, b) BCB polymer is spin-coated onto the sample, c) RIE etches the BCB to reveal NW tips, d) photolithography for transparent contacts before development (PR = photoresist), e) sputter deposition of transparent contacts (TC), f) photolithography for opaque contacts after development, g) electron beam deposition of opaque contacts (OC), and h) sputter deposition of Al back contacts followed by RTA.

3.3.1 Polymer Spin-coat

A polymer spin-coat was applied to the NW arrays (Figure 3.5b) to improve their physical rigidity, to electrically insulate the top and bottom contacts, and to planarize for the remaining device fabrication steps. BCB was designed to be a spin-on dielectric for microelectronic devices [118]. Therefore, it has high breakdown voltage (5.3 x 10^6 V/cm) and high resistivity (1 x 10^{19} Ω-cm).

BCB was drop-cast onto a stationary sample loaded on a Laurell WS-650MZ-23NPP spinner. The sample was spun at 5000 rpm for 77 seconds at a ramp rate of 300 rpm/s followed by a softbake at 100 °C for 90 seconds. Spin characteristics were determined by a previous study [48]. Next, the sample was

hardbaked in a nitrogen glovebox at 250 °C for 1 hour during which it reached its final properties. Hardcure parameters were determined from the DOW Chemical data sheet. Once hardcured, BCB can only be thinned with RIE.

3.3.2 RIE Etchback

RIE was used to thin the BCB layer and expose the tips of the NWs for contacting (Figure 3.5c). BCB monomers consist of carbon, hydrogen, oxygen, and silicon atoms [119] and therefore require two gas reactants in RIE. Carbon is etched with oxygen, and silicon is etched with fluorine (CF_4), as described in Section 3.1.3.

RIE etchback was performed on the same Technics RIE system as in Section 3.1.3. Typical parameters included 4 sccm of CF_4, 4 sccm of O_2, RF power of 40 W, and a chamber pressure of 180 mTorr. Regularly, 100 nm – 600 nm of BCB is removed to reveal the NW tips. An RIE parameter study to minimize BCB roughness is discussed in Section 3.4 below.

3.3.3 Photolithography

Photolithography is the process of defining micron-scale patterns on a sample surface. It employs a pre-designed chromium shadow mask to project UV light to a UV sensitive polymer, which is spin-cast onto the sample. A developer solution is used to remove exposed regions of polymer (positive resist) or unexposed regions of polymer (negative resist) thereby transferring the pattern to the sample surface.

Two photolithography steps were use in this thesis. One to define the position of a transparent conductive layer (Figure 3.5d), and another to position opaque contact pads (Figure 3.5f). In both cases S1800 series positive photoresist was used. Mask alignment was performed on a Karl Suss MJB-3 aligner in a class 10000 cleanroom environment. After subsequent contact deposition, the photoresist was lifted off in an acetone bath.

3.3.4 Sputter Deposition

Sputtering is a method of thin film deposition for a wide range of conductive or insulating materials. It uses a combination of inert and reactive gases in a plasma to bombard a target. In RIE that target is the sample, but in sputtering the target is a pure version of the deposition material and the sample is placed opposite the target in the chamber.

In Figure 3.5e, indium tin oxide (ITO) was deposited via sputtering as a transparent contact. 250 nm was deposited in a Kurt Lesker system with an RF magnetron sputtering gun. Typical parameters included 36 sccm argon, 0.2 sccm oxygen, 5 mTorr pressure, and 124 W RF power for a deposition rate of 2 Å/s. In Figure 3.5h, 250 nm of aluminum was deposited via sputtering as a back contact. Typical parameters included 10 sccm argon, 1 mTorr pressure, and 145 W RF power for a deposition rate of 1.2 Å/s.

3.3.5 Electron Beam Evaporation

Electron beam evaporation (e-beam) is a method of thermal evaporation usually used for depositing thin metal films. In this technique, metals are locally heated through high energy electron bombardment until they reach an evaporation temperature and begin depositing on a suspended sample. Deposition rate and total thickness are measured with a quartz crystal thickness monitor. Opaque contacts were deposited (Figure 3.5g) after photolithography. They consisted of 25/50/225 nm of Ni/Ge/Au deposited at 1 Å/s.

3.3.6 Rapid Thermal Annealing (RTA)

RTA is process of quickly heating a sample to select one thermally activated process over another (dopant diffusion, alloy formation, crystal reorientation, etc.). Annealing was performed on a JIPELEC Jetfirst RTA at 400 °C for 1 minute. The process helped form ohmic contacts between aluminum and p-Si on the back and reduced the resistivity of the ITO layer on the front.

3.4 RIE Etchback Roughness

Roughness of the BCB after RIE etchback is an important parameter to consider while fabricating a device. The entire multi-layer top contacting scheme in Figure 3.5 sits on top of the BCB planarization layer. Roughness in the BCB affects resistivity in the transparent contacts, and can induce cracking of the contacts during subsequent annealing steps [120]. Previous reports from our

research group identified a post-etch roughness (R_a) greater than 90 nm [48], while other groups obtain roughness (R_{rms}) between 5 and 19 nm [121]. Clearly, there was room to improve our RIE recipe and a project commenced to reduce BCB roughness. The first stage of the project was performed by me, in which I reduced the roughness from 90 nm to 18 nm (Table 3.2). Stage 2 of the project was the work of my summer student Karam Ghanem and supervised by me. Karam was able to reduce the roughness below 5 nm. Both works are summarized in this section and are differentiated by 'stage 1' and 'stage 2' labels.

Roughness in plasma etched films can originate from many factors. Redeposition of involatile material or etch products can create micro-masking [122]. Micro-masking materials are etch resistant thereby reducing local etch rates and increasing roughness. High power, or low pressure can lead to local high energy events that create hot spots in the plasma thus roughening through ion bombardment. In a two-reactant gas, such as required for BCB, gas ratios can be very important both for roughness and overall etch rate. Low oxygen content leads to over etching of silicon components in BCB and under etching of the remaining carbon polymer [123]. Conversely, high oxygen content plasmas etch silicon components more slowly and can passivate the BCB surface with SiO_2 [118].

The goal of this project was to reduce surface roughness (R_a) below 10 nm so that a nickel transparent conductive layer could be used in place of ITO. 250 nm of ITO becomes nearly opaque beyond 2 µm wavelength. Thinner ITO (28 nm) has approximately 60% transmittance in the IR; however, the resistivity is also

increased by an order of magnitude relative to bulk [124]. For applications in IR photodetection, nickel is a more appropriate transparent contact. 10 nm of nickel has lower resistivity than bulk ITO, but still retains 40% - 50% transmittance across IR wavelengths (1 – 25 µm). Further transmittance can be gained by reducing the thickness of nickel at the expense of resistivity.

In the first stage, a short study on the effects of gas flow rates was performed. In stage 2, a thorough parameter study was performed on RF power, pressure, gas ratios, temperature, and the addition of nitrogen. In all cases, the pre- and post-etch thicknesses were measured using VASE (model in Section 9.1 of Appendix, defined in stage 1). Roughness ($\mathrm{R_a}$) was measured using AFM with parameters outlined in Section 2.2. Roughness was normalized to the etched thickness ($\mathrm{R_a}/\Delta_{\mathrm{Thickness}}$) to make results comparable across all etch rates and etch times. Normalized roughness had an error of ± 0.002 nm/nm for all recipes, defined by the standard deviation of at least 3 repeated etches. The roughness of BCB before etching was found to be less than 1 nm.

Recipe 1 in Table 3.2 was created by a previous student according to the BCB data sheet from DOW Chemical [118], and prior reports of BCB etching [125,126]. Recipe 2 was intended to be a simple, one-variable improvement over the original recipe. By increasing the flow rates of both CF_4 and O_2, the gas ratio was maintained while the replenishment rate of reactants was increased. More reactants in the plasma created a more isotropic etch, which normally has a smoothing effect.

Table 3.2: RIE recipe alterations for improved BCB roughness. Stage 1 of the project.

Parameter	Recipe 1	Recipe 2
RF Power (W)	50	50
Pressure (mTorr)	180	180
CF_4 (SCCM)	2	4
O_2 (SCCM)	2	4
Time (min)	10	10
Etch rate (nm/min)	34	59
R_a (nm)	90	18
Normalized R_a (nm/nm)	0.264	0.030

Each recipe in Table 3.3 represents a study of one specific parameter. Recipes 3 and 4 studied the effects of power and pressure, with no significant improvement in normalized roughness. Recipe 5 showed an increase in roughness when the relative amount of CF_4 in the plasma was increased. In this limit, there is sufficient CF_4 to etch the silicon components of the BCB, but carbon is etched more slowly. Carbon components and deposited polymer from excess CF_4 begin to micro-mask underlying BCB and create local spikes and roughness. High oxygen content plasmas were not tested because they are known to create an amorphous SiO_2 etch passivation layer and reduce etch rates to zero [118]. Recipe 6 explored the use of temperature control with a cold tap water cooling loop that sits below the bottom electrode of the RIE. The cooling loop can only be set on or off and cools with 10 °C water. Cooling the sample while etching produced the first significant improvement in normalized roughness. It provides etching uniformity across the sample thereby reducing roughness while maintaining a high etch rate. Recipe 7 is the culmination of all previous recipes with additional nitrogen.

Nitrogen is believed to form NO, which preferentially attacks Si-O bonds to produce NO_2 [123]. Remaining silicon easily bonds to the fluorine ions and is pumped away as the volatile compound SiF_4. Nitrogen also helps dissociate diatomic oxygen to atomic oxygen, which equalizes the ratio of oxygen and fluorine ions in the plasma although the flow rate of CF_4 is much higher than O_2. The cumulative effect of nitrogen and previous recipe optimizations was to reduce the roughness below 5 nm, while decreasing the etch rate to 21 nm/min. Less than 10 nm of roughness can be maintained up to an etched thickness of 714 nm, thereby achieving a suitable roughness for nickel transparent contacts.

Table 3.3: RIE recipe alterations for improved BCB roughness. Stage 2 of the project.

Parameter	Recipe 3	Recipe 4	Recipe 5	Recipe 6	Recipe 7
RF Power (W)	70	50	50	50	50
Pressure (mTorr)	180	300	180	180	490
CF_4 (SCCM)	4	4	7	4	35.8
O_2 (SCCM)	4	4	3	4	5.37
N_2 (SCCM)	0	0	0	0	1.79
Water-cooling	Off	Off	Off	On	On
Time (min)	10	10	10	10	10
Etch rate (nm/min)	62	49	44	64	21
R_a (nm)	18	13	64	14	3
Normalized R_a (nm/nm)	0.029	0.028	0.147	0.022	0.014

Figure 3.6 shows SEM images taken after 10 minutes of etching for recipes 2 and 7. A reduction in etched roughness is clear between the two samples; however, both samples had a resistivity of 1.4×10^{-5} Ω-cm (14 Ω/sq), or approximately double the value of bulk resistivity. This indicates that 10 nm of nickel is sufficiently thick to eliminate any correlation with roughness. Thus, it is

possible to use a thinner layer of nickel with recipe 7 (Figure 3.6b) and increase the IR transmittance. A thickness study should be performed to find the minimum nickel thickness before the effect of roughness is seen.

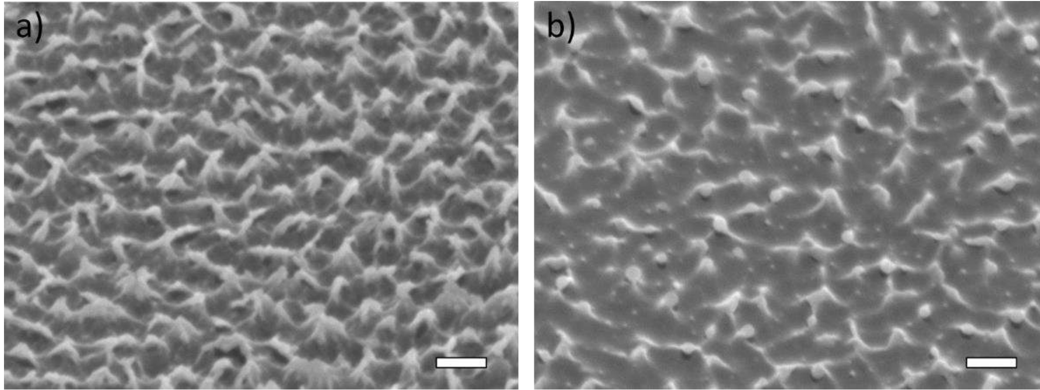

Figure 3.6: SEM images of etched BCB using a) Recipe 2 (R_a = 18 nm) and b) Recipe 7 (R_a = 3 nm). Images are tilted to 30 degrees and scale bars indicate 200 nm. Samples are covered by 10 nm of e-beam deposited nickel.

4 InAs Growth Modes on Silicon

4.1 Summary

This chapter contains work from our publication in the Journal of Crystal Growth titled "InAs nanowire growth modes on Si(111) by gas source molecular beam epitaxy" (DOI: 10.1016/j.jcrysgro.2015.11.035)[101]. In this report InAs NWs were grown on silicon substrates by MBE using five different growth modes: (1) Au-assisted VLS growth, (2) positioned (patterned) Au-assisted growth, (3) VS (catalyst-free) growth, (4) positioned Au-assisted VLS growth using a patterned oxide mask (VLS-SAE), and (5) SAE using a patterned oxide mask. Optimal growth conditions (temperature, V/III flux ratio) were identified for each growth mode for control of NW morphology and vertical NW yield. The highest yield (72%) was achieved with the SAE method at a growth temperature of 440 ˚C and a V/III flux ratio of 4. At the time of publication, no single study had been performed on all the main growth modes of InAs on silicon. Also, within McMaster, InAs NWs were never previously grown in the VS, or SAE modes, nor had it been grown on silicon in any mode. This study represents the beginning of integration of antimonide compounds with silicon. In Chapter 6 we use the same SAE InAs NWs to nucleate large diameter InAsSb NWs with a high yield.

4.2 Introduction

The direct integration of III-V materials with Si has the potential for low-cost, large-area device applications such as infrared photodetectors [17], photovoltaics [127], and high speed electronics [128]. However, III-V thin films cannot be grown directly on Si due to the lattice-mismatch strain between them that leads to the formation of misfit dislocations and severely degrades device performance. One approach that has attracted considerable attention recently is the direct growth of III-V NWs on Si. Lattice mismatch strain in NWs is relieved by elastic relaxation near the NW surfaces [129]. This enables highly lattice-mismatched III-V NWs to be grown directly on Si substrates, enabling large-area, low-cost III-V devices to be monolithically integrated into existing and mature Si technology. InAs NWs are particularly interesting because of their small bandgap and high electron mobility with potential applications in infrared photodetection [17] and high speed electronics [128]. NWs also support optical resonant modes such that they act as very effective waveguides that concentrate and absorb light, enabling highly efficient infrared photodetection [75].

NWs are typically grown using the VLS process in which a foreign metal seed particle (typically Au) nucleates the growth of NWs [130–132]. Growth species collect in the metal droplet by direct impingement, by diffusion after impingement on the surrounding substrate surface (the collection area), or by diffusion after impingement on the NW sidewall surfaces (following initial formation of the NW). Supersaturation of the seed particle by the growth species

results in the nucleation and epitaxial growth of NW material at the droplet-solid interface. NWs may also form below the Au-III eutectic temperature, which is usually referred to as vapour-solid-solid (VSS) growth [133]. The Au-assisted VLS growth mode is the most well-established method but Au may incorporate into semiconductor materials, leading to deep level defects [134]. Prior studies have shown a reduction in carrier lifetime in Au-assisted as compared to Ga-assisted GaAs NWs [135]. Au is also incompatible with Si CMOS technology. Thus, it is preferred to remove Au from the growth process entirely. To this end, growth methods beyond the typical metal-assisted (VLS) approach have been studied. These include self-assisted growth [94,136–140], VS (catalyst-free) growth [28,31,36,141,142], and SAE [143,144].

In this chapter, we consolidate in a single study all the typical growth modes of InAs on silicon. Prior studies of InAs NW growth were typically conducted using solid-source molecular beam epitaxy (SS-MBE) or metal-organic vapor phase epitaxy (MOVPE). SS-MBE uses As_4 as the source species, derived from an effusion cell. In the present chapter, we present a growth study using gas source molecular beam epitaxy (GS-MBE), which uses As_2 derived from the cracking of gas hydrides (AsH_3). The advantage of GS-MBE consists of an essentially infinite supply of group V species from the external hydride sources. Furthermore, NW growth with As_2 differs from that with As_4. The dimer tends to decrease the group III diffusion length on NW sidewalls resulting in a reduced axial growth rate and an increased radial growth rate [145]. MOVPE typically uses metal-organics and hydrides, such

as trimethylindium (TMI) and arsine (AsH_3), as gaseous precursors. Precursors only decompose when enough thermal energy is supplied, which allows for a high selectivity of growth on patterned substrates [132,146]. However, it also requires higher temperature and V/III flux ratios than is typically used in MBE. GS-MBE uses a direct flux and relies on surface diffusion of adatoms to achieve selectivity of growth. These differences warrant a comprehensive study of the various growth modes by GS-MBE.

To our knowledge, there has been no prior report of the various InAs growth modes using GS-MBE. One single study spanning many growth modes, as in the present study, is advantageous because it allows a direct comparison of the various modes while minimizing systematic errors. Both patterned and randomly positioned NWs were investigated. The influence of temperature, V/III flux ratio and pattern period on NW yield and growth rate were studied. The conditions required for a high yield of vertical InAs NWs were identified.

4.3 Experimental Details

Boron-doped Si (111) substrates were used in all NW growths. NW growths were performed on oxide-free substrates (Figure 4.1a) and oxide-covered substrates (Figure 4.1b). Referring to Figure 4.1, each substrate was further delineated into zones containing either: (i) a large-area Au thin film; (ii, iv) a similar Au film, but patterned into an array of disks by EBL; and (iii, v) a Au-free zone.

Growth modes (i), (ii), and (iii) occurred simultaneously on the same substrate. Similarly, growth modes (iv) and (v) occurred simultaneously on the same oxide-covered substrate. Each of these cases is described in more detail below.

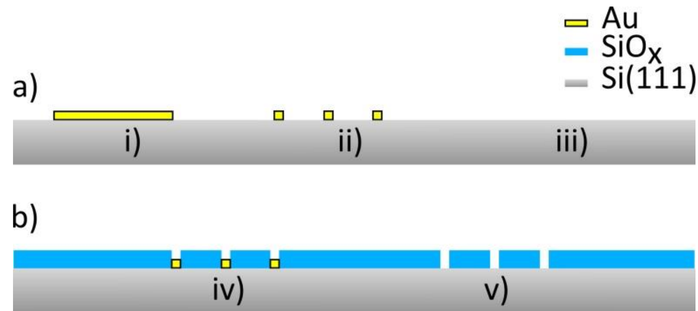

Figure 4.1: Cross-sectional schematic of a) oxide-free Si substrate and b) Si substrates with CVD-deposited silicon oxide as they are prior to loading into the MBE. Growth methods/regions include i) Au-assisted, ii) positioned-Au-assisted, iii) catalyst-free, iv) Au-assisted-SAE, and v) SAE.

(i) Au-Assisted VLS Growth: This case describes the Au-assisted VLS growth of randomly positioned NWs. A 30 s dip in semiconductor grade BHF was used to remove the native oxide from this region of the substrate. Immediately after BHF etching, a 3 nm thick Au film was deposited on the oxide-free region at room temperature by electron beam evaporation. The sample was then immediately loaded into the GS-MBE system for Au-assisted NW growth. As the temperature is raised for NW growth, the Au film consolidates into randomly positioned Au seed particles.

(ii) Positioned-Au-Assisted VLS Growth: This case describes the positioned Au-assisted VLS growth of NWs. A VISTEC EBPG 4200+ EBL system, operating at 100 kV, was used to form patterned holes in a 120 nm thick ZEP 520A photoresist

layer. After developing the photoresist, a 30 s BHF etch removed the native oxide in the holes. The Au disks were then formed by the immediate evaporation of a 3 nm thick Au film followed by a standard lift-off process. The EBL patterns were comprised of several 100 µm x 100 µm arrays, each containing a different hexagonal period (360, 440, 520, 600, 1000 nm) and Au disk diameter (22, 30, 48, 71, 83 nm). Au disk diameters were controlled via the electron beam current (nA) and total dose received by the resist (µC/cm^2). A 30 s BHF etch was performed just prior to sample loading in the GS-MBE to ensure an oxide-free surface between the Au disks.

(iii) VS Growth: This case corresponds to the VS growth method of randomly positioned NWs. Preparation for this case followed the same procedure as in the unpatterned Au-assisted case but without any Au deposition. A 30 s BHF etch was performed just prior to sample loading in the GS-MBE, which produced an oxide-free surface.

(iv) Au-Assisted-VLS-SAE: This case corresponds to the situation commonly known as Au-assisted selective area epitaxy (Au-assisted-VLS-SAE). For the oxide-covered substrates, 20 ± 2 nm of SiO_x was deposited by CVD. EBL patterns were transferred from the resist layer into the oxide using RIE for 40 s under 320 mTorr of CF_4. RIE was followed by a 35 s BHF wet etch. Immediately after BHF etching, the substrate was loaded into the e-beam evaporator for 3 nm of Au deposition, followed by a standard lift-off process. The patterns were comprised of several 100 µm x 100 µm arrays, each containing a different hexagonal period (360, 440,

520, 600, 1000 nm) and Au disk/oxide hole diameter. The Au disks (diameters of 22, 30, 48, 71, 83 nm) were isolated within larger oxide holes (diameters of 64, 65, 67, 83, 94 nm, respectively). The oxide holes were larger than the Au disks due to undercutting of the resist during RIE and HF etching.

(v) SAE: This case corresponds to the situation commonly known as selective area epitaxy. Holes were patterned into an oxide which covered the Si substrate as described above, but without any Au deposition. A 10 s BHF dip was performed immediately before loading into the GS-MBE to ensure all native oxide was removed from the bottom of the holes.

In all cases, InAs NWs were grown by GS-MBE in which As_2 was supplied from a hydride (AsH_3) cracker cell operating at 950 ˚C, and In was supplied by an effusion cell. Substrates were degassed at 300 ˚C for 15 minutes and then annealed at 700 ˚C for 15 minutes. The substrates were then cooled down to the growth temperature before introducing the growth species. Growth was initiated in the GS-MBE at the growth temperature by simultaneously opening the In shutter and As_2 gas flow. Substrate temperature was varied from 330 ˚C to 400 ˚C for the oxide-free substrates and from 400 ˚C to 460 ˚C for oxide-covered substrates. Unless otherwise specified, In impingement rate was 0.125 µm/h, V/III flux ratio was 4, and growth duration was 30 min. After growth, samples were cooled down without an In or As_2 flux.

Post-growth analysis was done using a JEOL 7000F SEM and a JEOL 2010F TEM. SEM images were taken at a tilt angle of 30˚ to the substrate normal. Length measurements were made from the base to the top of the NW (just below the droplet, if one existed). No adjustments were made to account for the portion of the NW length buried by film growth. Diameter measurements were made near the top of the NWs. TEM images were taken along the {2110} zone axis.

4.4 Results and Discussion

4.4.1 Au-Assisted VLS Growth

A representative SEM image of InAs NWs grown on a Si (111) substrate at 330 ˚C by the Au-assisted method (corresponding to Figure 4.1a(i)) is shown in Figure 4.2a. The highest density of NWs was obtained at 330 ˚C, as represented in Figure 4.2a. The NW density decreased with temperature until 400 ˚C where NW density was negligible. Higher magnification SEM images, such as that shown in the inset of Figure 4.2a, indicated the presence of a Au droplet at the top of each NW, confirming that growth occurred by the Au-assisted method. The Au seed particles acted as a site for preferred nucleation of the NWs. The NWs grew preferentially in the direction perpendicular to the Si (111) substrate, similar to other III-V NWs reported in the literature [60]. The NW morphology was rod-shaped with minimal tapering.

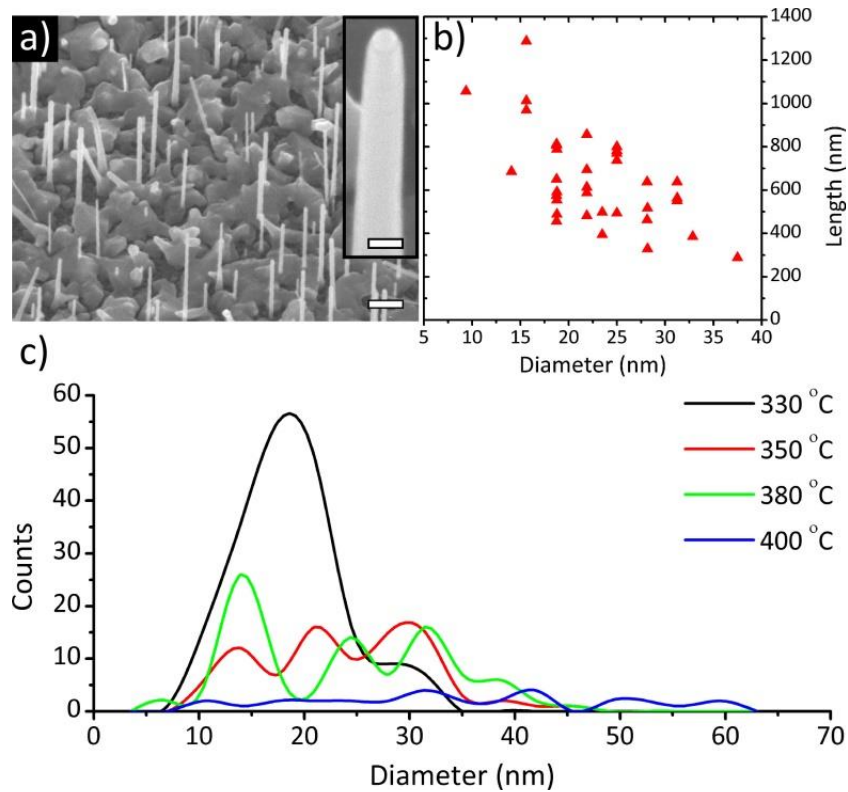

Figure 4.2: Au-assisted NWs (Figure 4.1a(i)) grown at 330 ˚C. (a) SEM image of NWs. Scale bar is 200 nm. Inset shows Au droplet at the NW tip with scale bar of 50 nm. (b) Length versus diameter of NWs. (c) Distribution of NW diameters for the indicated growth temperatures.

The length and diameter of NWs were measured, as shown in Figure 4.2b, for the 330 ˚C growth temperature. The axial growth rate varied between 10 nm/min and 40 nm/min, depending on NW diameter, with an average of 21 nm/min among all NWs in Figure 4.2b. The dispersion in Au nanoparticle dimensions, arising from the Au thin film, resulted in multiple possible starting diameters for the NWs. An inverse relationship between NW length and diameter was observed, which is usually indicative of growth that is limited by In diffusion on the substrate surface or NW sidewalls [147]. The roughness of the substrate

surface evident in Figure 4.2a indicates that an InAs thin film also grew by vapour-solid deposition on the Si (111) surface between the NWs. In such a case, the adatom diffusion along the surface surrounding each NW, and feeding the NW growth, will be very much reduced by the surface roughness. The collection of adatoms from the NW sidewalls will also be negligible in the early stage of growth before any substantial NW length has formed. Thus, NWs are expected to grow predominantly by direct impingement on the nanoparticle in the early stages of growth. At the same time, thin film deposition will occur on the substrate surface surrounding each nanoparticle and/or NW. Hence, Au nanoparticles and/or NWs may become buried in the competing thin film, resulting in a low surface density of NWs.

We also speculate that there may be an incubation period between the time when the In shutter is opened, and the time when NW nucleation occurs, as observed in other NW materials [148,149]; i.e., some incubation time is required to supersaturate the Au seed particle with In before the onset of NW growth. During this delayed onset of NW growth, the thin film growth can bury the seed particles, again resulting in a low surface density of NWs.

Diameter distributions are presented in Figure 4.2c for each of the four growth temperatures investigated (330, 350, 380, 400 ˚C). The highest NW density was obtained at the growth temperature of 330 ˚C with most of the NWs having a diameter in the range of 10-30 nm. The NW density decreased, and the spread in NW diameters increased, with increasing growth temperature. These

observations are likely due to the instability of the seed particles when annealing at the substrate temperature before the onset of growth. For example, Plante et al [149] showed an increasing spread in the size distribution of Au nanoparticles with temperature due to atomic Au diffusion on the substrate surface. Jung et al [150] showed that InAs NW growth could originate from the splitting and diffusion of larger Au particles into smaller ones. These processes result in the formation of nanoparticles of various sizes originating from the initial Au film and are responsible for the corresponding distribution in starting diameters and eventual length distribution of NWs. As shown in Figure 4.2b, the larger Au nanoparticle diameters that occur at the higher growth temperatures will result in a much lower growth rate of NWs due to the inverse length-versus-diameter growth relationship. The larger diameter NWs are also expected to require a longer incubation time for supersaturation before the onset of NW growth. As a result, larger diameter nanoparticles at the higher growth temperatures are more likely to become buried in the competing two-dimensional film growth, resulting in the observed low density of NWs with increasing temperature.

Previous studies have shown that InAs NWs grown by SS-MBE are possible in the temperature range between 300 to 440 ˚C [132,151–155]. These growth temperatures are below the Au-In eutectic temperature, leading some to refer to this process as vapour-solid-solid (VSS) growth [133]. However, in situ reflection high-energy electron diffraction (RHEED) observations of phase transitions of the seed particle at the tip of InAs NWs indicated that they can be liquid below the

eutectic point of the Au-In alloy [132]. Therefore, the growth of InAs NWs may occur by the VLS growth process from a liquid Au-In droplet, despite the growth temperature being below the eutectic temperature [132].

4.4.2 Positioned-Au-Assisted VLS Growth

In this method, Au disks were patterned by EBL (corresponding to Figure 4.1a(ii)) with the aim of producing NWs with identical diameter and length. An SEM image of InAs NWs grown by GS-MBE is shown in Figure 4.3 for a growth temperature of 330 ˚C, Au disk diameter of 83 nm, and period of 360 nm. Au droplets were observed at the top of NWs by SEM (not shown), confirming that growth occurred by the Au-assisted VLS method. However, the NW yield (fraction of Au disks that resulted in a NW) was below 1%. A similar low yield (<1%) of NWs was obtained regardless of growth temperature (330, 350, 380, 400 ˚C), Au disk diameter (22, 30, 48, 71 and 83 nm), or pattern period (360, 440, 520, 600 and 1000 nm). The axial growth rate of the vertically oriented NWs, averaged over 8 NWs, was 22 nm/min at 330 ˚C. A rough two-dimensional film growth was observed in all cases, which covered most of the deposited Au. As described earlier, this rough film growth, and the likely presence of an incubation time before the onset of NW growth, resulted in the nanoparticles and/or NWs becoming buried and producing a low NW yield. One might consider predicting the positioned Au-assisted NW yield as $\sigma A/N$ where σ is the unpatterned NW density (Figure 4.2a), A is the total area of Au in the patterned array, and N is the number of Au dots in the array. The highest density of unpatterned NWs was 6

μm^{-2} at a temperature of 330 ˚C. Considering the array with the largest disk diameter (83 nm) and smallest period (300 nm), we estimate the maximum yield to be ~3%.

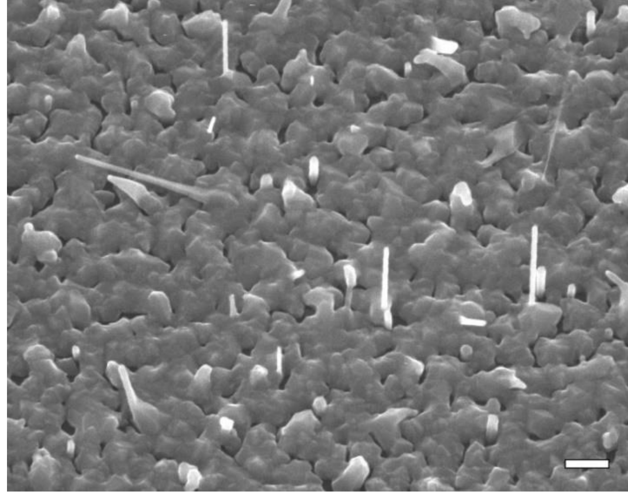

Figure 4.3: SEM image of NWs grown at 330 ˚C by positioned Au-assisted VLS growth (Figure 4.1a(ii)). Scale bar is 200 nm.

As will be discussed later, suppression of the film growth is necessary to produce a high NW yield. This can be accomplished with the presence of an SiO_x oxide layer on the Si substrate surface. The Au-assisted VLS growths on bare Si (111) surfaces will therefore not be considered further.

4.4.3 Catalyst-Free VS Growth

Randomly positioned VS NWs were grown by GS-MBE on the Si (111) substrate, corresponding to case (iii) in Figure 4.1a. SEM images for four growth temperatures are presented in Figure 4.4, showing that the NWs were non-tapered. The inset of Figure 4.4c shows a TEM image of the tip of a NW grown at 380 ˚C. It shows the absence of any droplet at the NW tip. The cool down after

NW growth was done without any group V flux impingement. Therefore, consumption of an In particle due to reaction with As_2 during cool down could not have occurred. Instead, the lack of an In droplet indicates that the NWs grew by a VS method. The contrast stripes evident in the TEM image are stacking faults, commonly observed in NWs, where the crystal structure alternates between zincblende and wurtzite [54].

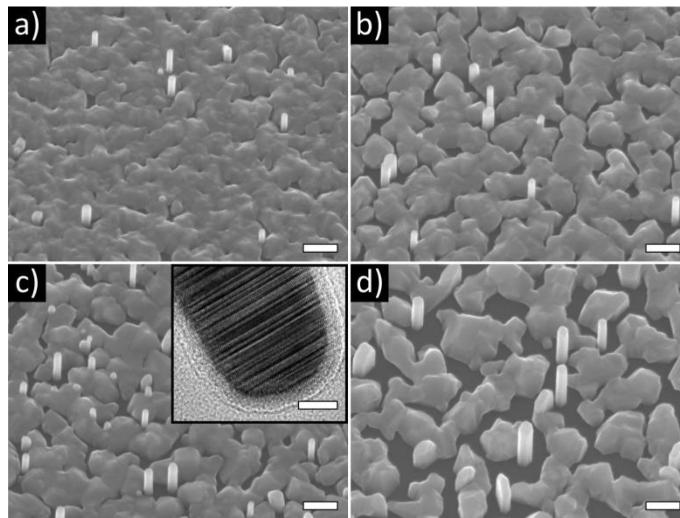

Figure 4.4: SEM images for VS NWs (Figure 4.1a(iii)) grown with a V/III flux ratio of 4 and temperature of a) 330 ˚C, b) 350 ˚C, c) 380 ˚C and d) 400 ˚C. Scale bars are 200 nm. Inset in c) shows a TEM image of the tip of a wire grown at 380 ˚C with a 10 nm scale bar.

Previous work [28,36,127,141,142] using MOVPE and SS-MBE has observed similar non-tapered InAs NWs without the use of Au droplets. In particular, Dimakis et al [28] observed that the nucleation of InAs NWs in SS-MBE took place in In-rich areas forming spontaneously on the Si (111) substrate in the beginning of the growth process. As the nucleation proceeded, the growth conditions changed from In-rich to As-rich, and the growth continued in a VS mode

without an In droplet at the tip of the NWs. Growth of the NWs then occurred by the anisotropic incorporation of adatoms on the top facet of the NW as compared to the NW sidewalls. We speculate that our NWs may grow by the same method as described by Dimakis et al [28], although further work (such as the detailed growth time study by Dimakis et al [28]) is needed to ascertain the details of growth.

The VS growth method, described above, should be contrasted with the self-assisted VLS growth method. The presence of a thin oxide layer on a substrate can lead to self-assisted NW growth [94,136–140]. For example, Grap et al [137] achieved self-assisted SS-MBE growth of InAs NWs by creating a thin (~6 nm) porous oxide layer on a GaAs surface. Upon the initiation of growth, In droplets form in pinholes in the porous oxide. These In droplets subsequently act as the seed particles for self-assisted NW growth. It also appears that, for self-assisted growths, the growth conditions are sufficient to maintain In supply and sustain the droplet at the top of the NWs throughout growth. In our case, however, VS samples were BHF etched immediately prior to loading in the GS-MBE. This is expected to produce an oxide-free Si substrate. In this case, In droplets can form randomly on the Si surface by In diffusion and coalescence [28], which subsequently nucleate NW growth. However, unlike self-assisted NW growth, it appears that In supply to the tip of the NWs for our VS GS-MBE growths is insufficient to sustain a droplet, such that there is an eventual transition to VS NW growth.

As shown in Figure 4.5a, the NW diameter and length increased slightly with growth temperature for the VS growths. The axial growth rate increased with temperature from 6 nm/min at 330 ˚C to 12 nm/min at 400 ˚C. While the two previous Au-assisted cases produced axial growth rates greater than 20 nm/min at 330 ˚C, the VS growth mode only obtained a growth rate of 6 nm/min. Assuming the same growth method as described by Dimakis et al [28], the diameter of NWs is determined by the initial stage of In droplet formation. As the temperature increases, the In diffusion on the Si (111) surface increases and larger In droplets are expected, resulting in the nucleation of larger diameter NWs. In the later stage of growth, NWs grow axially by VS deposition with As-rich and group-III limited conditions (the V/III flux ratio is greater than unity). Therefore, an increased supply of In with increasing temperature, due to diffusion on the substrate surface or NW sidewalls, results in NW elongation.

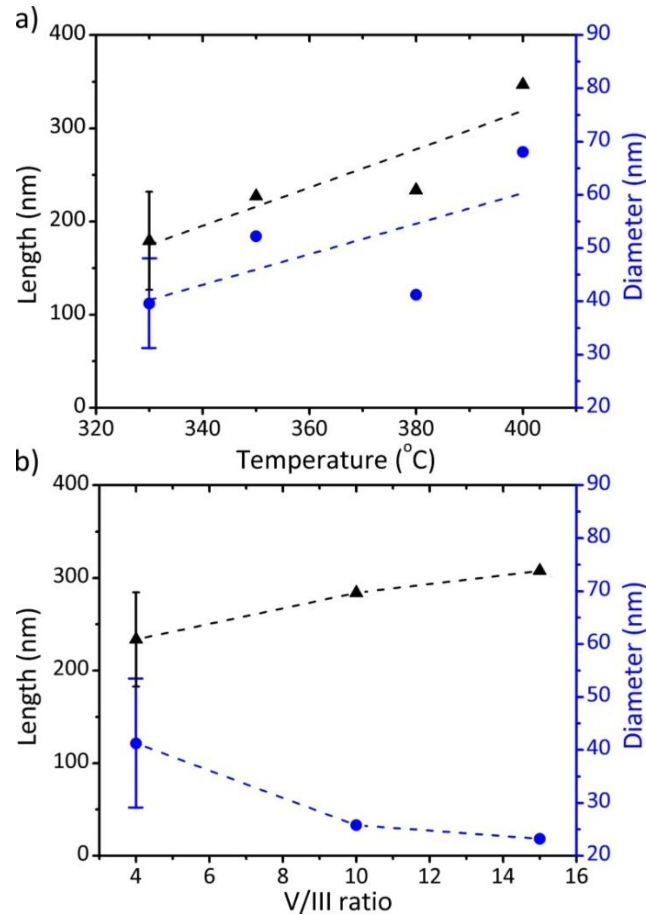

Figure 4.5: Morphological trends of VS NWs. a) Length and diameter versus temperature for VS NWs at a V/III flux ratio of 4. b) Length and diameter versus V/III flux ratio at a temperature of 380 ˚C. Diameter data is indicated by blue circles, length by black triangles. Dashed lines are visual guides only. Representative error bars are indicated.

Next, we examined the effect of V/III flux ratio at a constant growth temperature of 380 ˚C. The V/III flux ratio was varied by adjusting the As_2 flux, keeping the In impingement rate constant at 0.125 µm/h. As seen in Figure 4.5b, only a slight increase in NW length and decrease in NW diameter were observed for a nearly 4-fold increase in V/III flux ratio. The axial growth increased slightly with V/III flux ratio from 8 nm/min at a V/III flux ratio of 4 to 10 nm/min for a V/III

flux ratio of 15. The decrease in NW diameter with V/III flux ratio may signify a reduced In adatom diffusion length on the Si (111) surface under the presence of higher group V flux, leading to the formation of smaller In droplets and corresponding NW diameter. The relatively minor influence of the V/III flux ratio on the NW length is explained by the As-rich conditions prevailing during VS growth at the tip of the NW.

4.4.4 Au-Assisted-VLS-SAE

To circumvent the problems associated with two-dimensional film growth on the substrate surface between NWs, GS-MBE growths were performed using an oxide mask where film growth is suppressed. SEM images in Figure 4.6 show NWs grown by the Au-assisted-VLS-SAE method (corresponding to Figure 4.1b(iv)) for a Au disk diameter of 22 nm, period of 360 nm, and growth temperature varying between 400 and 460 ˚C. The presence of a Au nanoparticle observed by SEM at the top of NWs (not shown) verified that growth occurred by the Au-assisted method. As observed in Figure 4.6, the presence of an oxide mask has significant advantages compared to bare Si (111) substrates considered previously because parasitic film growth on the oxide surface can be suppressed. Indeed, negligible film growth was observed on the oxide surface above 420 ˚C.

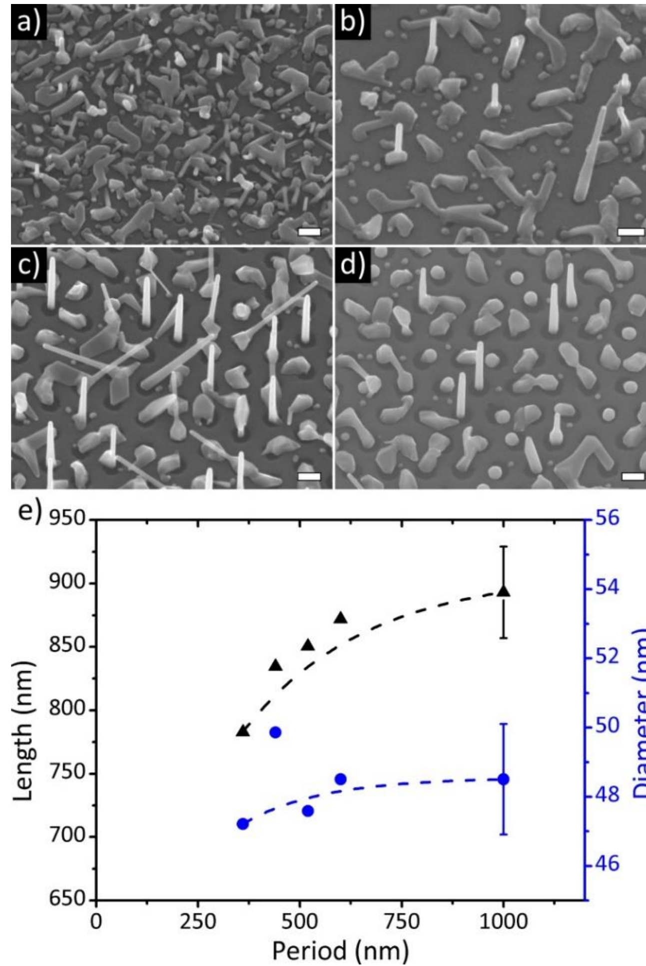

Figure 4.6: SEM images of patterned Au-assisted NWs on oxide-covered substrates (Au-assisted-VLS-SAE; Figure 4.1b(iv)) grown with a V/III flux ratio of 4 and temperature of (a) 400 ˚C, (b) 420 ˚C, (c) 440 ˚C and (d) 460 ˚C. Scale bars are 200 nm. e) Length and diameter versus period for NWs grown at 440 ˚C. Dashed lines are visual guides only. Representative error bars are indicated.

The yield of vertical NWs for a growth temperature of 400 ˚C was below 2%, as shown in Figure 4.6a. At this temperature, crystallite growth was observed on the oxide surface, presumably due to insufficient In diffusion to feed the Au disks for NW growth. Crystallite growth on the oxide surface decreased and the vertical NW yield increased with temperature (5% yield at 420 ˚C, and 10% yield at 440 ˚C), as shown in Figure 4.6b and 4.6c, representing an improvement over

the patterned Au case without an oxide. In addition to the vertical NWs, Figure 4.6c also shows NWs tilted along equivalent (111) growth directions. Increasing the temperature likely also increased the desorption of As_2, resulting in crystallites being replaced with In droplets on the oxide mask at 420 ˚C (Figure 4.6b). Above 440 ˚C (Figure 4.6c), As_2 desorption is likely a limiting factor in the NW growth. At 460 ˚C, many NWs and crystallites were replaced with In droplets in the oxide holes (Figure 4.6d). Note that the optimum temperature for Au-assisted-VLS-SAE growth (440 ˚C) is 110 ˚C higher than that for Au-assisted growth on bare Si substrate without an oxide (330 ˚C). This is likely due to differences in the In diffusion length on SiO_x compared to bare Si. The In diffusion length on SiO_x is likely less than the hole separation, allowing for only crystallite growth in the oxide holes at temperatures below 420 ˚C.

Figure 4.6e shows the NW length and diameter versus period for a growth temperature of 440 ˚C, V/III flux ratio of 4, hole diameter of 64 nm, and an initial Au disk diameter of 22 nm. To our knowledge, such a figure has not previously been presented for patterned Au-assisted InAs NWs. The NW length showed a strong dependence on period while NW diameter appeared nearly independent of period, with similar results obtained for other hole and Au disk diameters. These results can be explained using a model previously developed for the SAE growth of patterned GaAs NWs on Si (111) [41]. This model showed that growth material is supplied by a secondary flux of group V adatoms desorbing from the oxide surface between the NWs, which subsequently impinge on the NW droplet

and sidewalls. Shadowing of the incident and scattered flux by neighboring NWs in the array strongly affect the axial growth rate, leading to significant differences with period. The diffusion of As_2 is expected to be negligible. On the other hand, the desorption of In from the oxide surface is expected to be negligible at our growth temperatures, while In diffusion on the oxide surface and NW sidewalls is possible. The axial growth of the NWs therefore occurs by the direct impingement of As_2 on the droplet including desorption of As_2 from the oxide mask, while In is supplied by direct impingement on the droplet and diffusion from the oxide mask and NW sidewalls. These contributions increase with period, as the surface area of the oxide mask increases, as observed in Figure 4.6e [41].

Next, the effect of V/III flux ratio was investigated at a fixed temperature of 440 ˚C. The V/III flux ratio was varied by adjusting the As_2 flux, keeping the In impingement rate fixed at 0.125 µm/h. Figure 4.7a-d shows SEM images of the Au-assisted-VLS-SAE growths with V/III flux ratios of 2, 3, 4 and 10 for a 22 nm Au disk diameter and a 360 nm period. Increasing the V/III flux ratio caused the NWs to become longer and thinner, which is quantitatively shown in Figure 4.7e. The axial growth rates were 10, 16, 21 and 23 nm/min for V/III flux ratios of 2, 3, 4 and 10, respectively. At low V/III flux ratios (2 to 4), the axial growth rate increased rapidly with As_2 flux indicating that growth was limited by group-V flux being supplied to the Au-In droplet. When the V/III flux ratio exceeded 4, the length was almost independent of group V flux, indicating that the axial growth transitioned to a group-III limited regime, similar to that observed elsewhere [156] in a SS-MBE

system. The decrease in NW diameter with V/III flux ratio will be discussed in the next section.

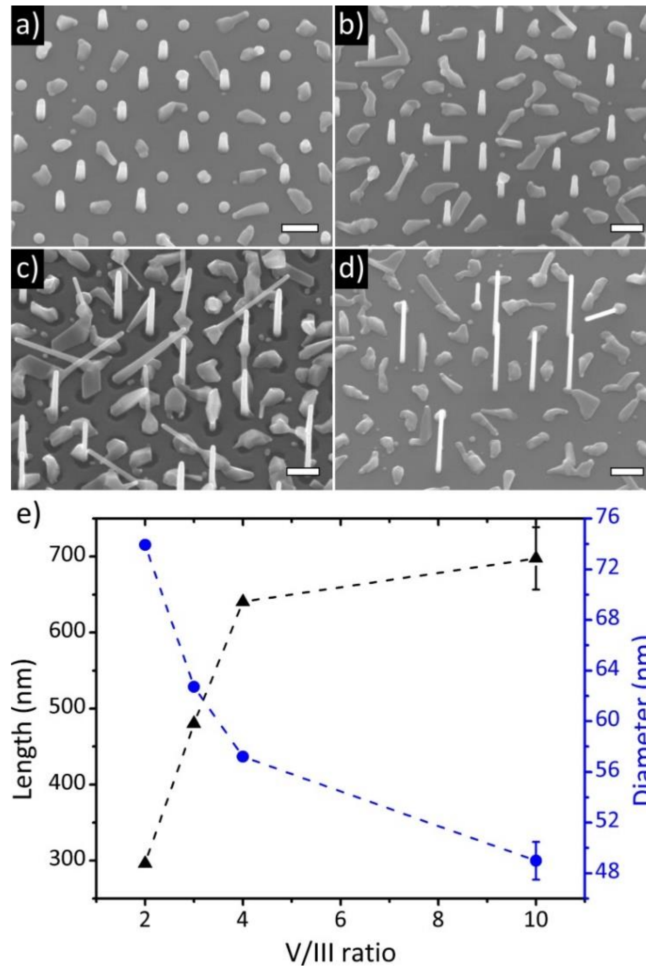

Figure 4.7: SEM images of Au-assisted-SAE NWs grown with a V/III flux ratio of a) 2, b) 3, c) 4 and d) 10 at a temperature of 440 ˚C. Scale bars are 300 nm. e) NW length and diameter as a function of V/III flux ratio. Dashed lines are visual guides only. Representative error bars are indicated.

4.4.5 SAE Growth

SEM images are shown in Figure 4.8 for SAE growth without Au droplets in the oxide holes (corresponding to the case in Figure 4.1b(v)) with a hole diameter of 94 nm, period of 360 nm, and a growth temperature ranging from 400 to 460

˚C. The NW yields at 400 ˚C, 420 ˚C, 440 ˚C, and 460 ˚C were 31%, 62%, 72% and 4%, respectively. The results were similar with different hole diameter or period. At the lowest growth temperature of 400 ˚C (Figure 4.8a), the oxide holes were mostly filled with one or more tilted NWs, or NWs crawling out of the holes onto the oxide surface. In some holes, multiple NWs grew in equivalent (111) directions, as shown in the inset of Figure 4.8a. Many crystallites were also observed on the oxide surface. At 420 ˚C (Figure 4.8b), fewer crystallites grew in the oxide holes, and were replaced with more vertical NWs. Crystallites no longer formed on the oxide surface and instead small (~30 nm) droplets remained, similar to Figure 4.6b. At 440 ˚C, no crystallites or droplets nucleated directly on the oxide surface and the vertical NW yield was highest. Finally, at 460 ˚C, In droplets formed in the holes and no NWs grew, signifying that NW growth was limited by As_2 desorption, similar to the Au-assisted-VLS-SAE case in Figure 4.6d. The size of the In droplets was larger than what could be accounted for by direct impingement, indicating that the holes were filled both by direct impingement and In diffusion from the oxide mask. To our knowledge, this transition from crystallites to NWs, and subsequently to droplets, with increasing temperature has not been reported previously for InAs NWs grown by MBE.

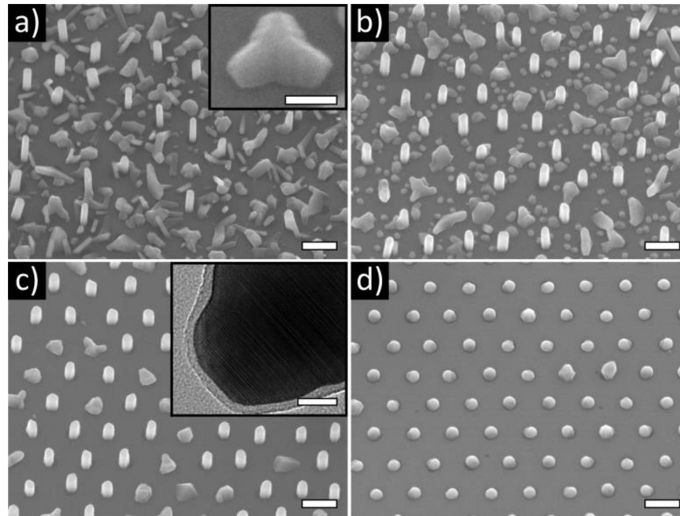

Figure 4.8: SEM images for SAE NWs (Figure 4.1b(v)) with a V/III flux ratio of 4 and a temperature of a) 400 ˚C, b) 420 ˚C, c) 440 ˚C and d) 460 ˚C. Scale bars are 300 nm. Inset SEM image in a) shows multiple NWs growing from a single oxide hole with 100 nm scale bar. Inset in c) shows a TEM image of a NW tip grown at 440 ˚C with a 10 nm scale bar. Reproduced with permission from Ref. [102].

We acknowledge that yield may be improved further, likely by optimizing the substrate preparation steps. For example, Madsen et al [44] found that leaving a thin (~1 nm) oxide on the substrate could increase vertical yield nearly to 100%. Meanwhile Plissard et al [43] found a correlation between Ga pre-deposition time and yield for GaAs NWs on Si(111). Other groups find that the method of etching, type of etchant, duration of etch, and the cleaning steps after etching can all affect the NW yield [31,32]. A combination of these optimized processes could help improve our yield; however, the exploration of substrate preparation steps is outside the scope of this report. With suitable optimization of surface and growth conditions, a nearly 100% yield of vertical InAs NW growth on Si is achievable in either MOVPE [146] or MBE [35].

The TEM image in the inset of Figure 4.8c shows that no droplets were observed on the NW tips, like Ref. [35] using SS-MBE. In our samples, no As_2 flux was impinging during the cool-down procedure after NW growth. Therefore, any In droplet that may have been present at the tip of the NWs during growth would have remained there because there was no As present to consume the droplet during cool down. Instead, the absence of an In droplet indicated that none was present in the final stage of growth. These results indicate that NW nucleation may have occurred by the formation of In droplets in the holes, but that growth quickly transitioned to the VS mode [146], similar to the catalyst-free process discussed earlier.

The effect of V/III flux ratio was investigated at a constant temperature of 440 ˚C where the yield of vertical NWs was greatest. The V/III flux ratio was varied by adjusting the As_2 flux, keeping the In impingement rate fixed at 0.125 μm/h. SEM images of the SAE growths in Figure 4.9a-e show the results for V/III flux ratios of 2, 3, 4, 6 and 10 at a period of 360 nm and a hole diameter of 83 nm. The results were similar for different hole diameter or period. At a V/III flux ratio of 2, the holes were filled with In droplets, indicating that the As flux was too low to support any NW growth. As in Figure 4.8d, we note that the In droplets in Figure 4.9a are larger than expected by direct impingement, indicating that In diffusion occurred on the oxide mask. At a V/III flux ratio of 3, crystallites appeared to form in the holes. The inset of Figure 4.9b shows that the crystallites nucleated in the holes by In droplets, which in some cases remained at the top of the crystallites. Finally,

at V/III flux ratios above 4, NWs appeared with a length that increased and a diameter that decreased with V/III flux ratio, like Figure 4.7e. No In droplets were observed at the tip of the NWs. Hence, once again, the NW nucleation appeared to start from In droplets in the holes, as in the inset of Figure 4.9b, but then quickly transitioned to VS NW growth.

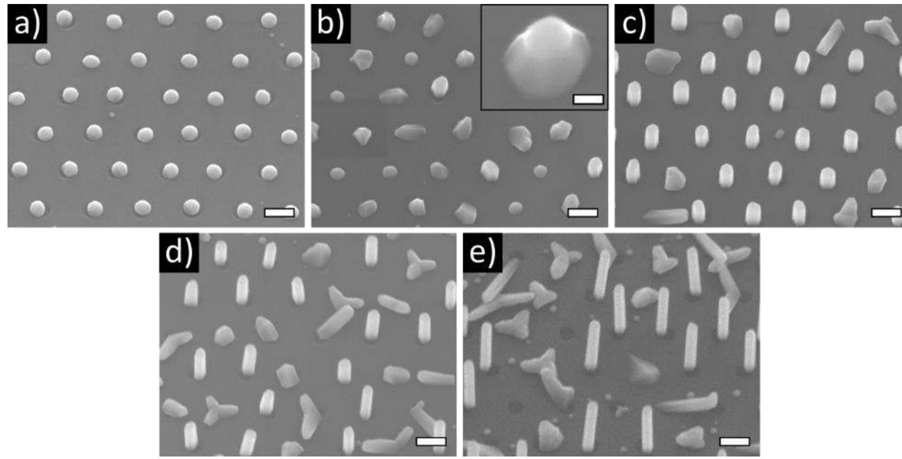

Figure 4.9: SAE NWs grown at 440 ˚C with V/III flux ratio of a) 2, b) 3, c) 4, d) 6 and e) 10. Scale bars are 200 nm. Inset in b) shows an SEM image of a crystallite with a droplet remaining on top. Scale bar is 50 nm. Reproduced with permission from Ref. [102].

Figure 4.10 shows the NW length and diameter versus period at 440 ˚C for an 83 nm hole diameter and V/III flux ratios of 4, 6 and 10 where NWs were observed to grow. The axial growth rate for SAE NWS was about 10, 13 and 22 nm/min for V/III flux ratios of 4, 6 and 10, respectively. NW length increased with period, indicating that axial growth occurred by desorption of As_2 from the oxide mask as discussed earlier [156]. NW length increased with V/III flux ratio showing a direct dependence of growth rate on group V flux. The dash-dotted horizontal

lines in Figure 4.10 represent the calculated NW length due only to direct impingement of the group V growth species. Any length above this horizontal line is due to secondary sources of As derived by desorption from the oxide mask [156]. To our knowledge, such a study on the effect of period on the length and diameter of SAE InAs NWs grown by MBE has not been presented previously for various V/III flux ratios.

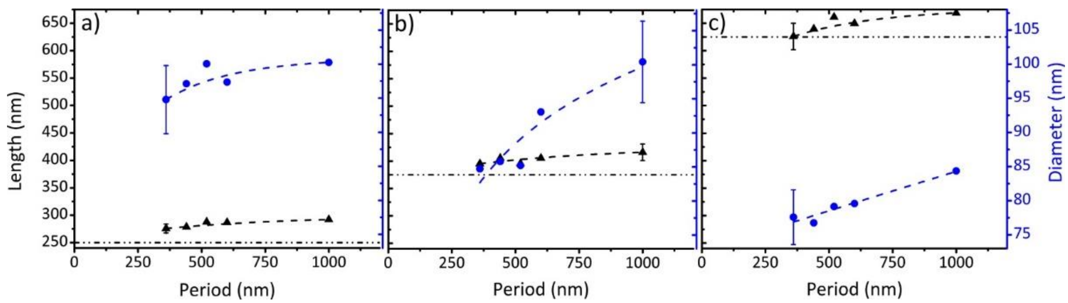

Figure 4.10: Length and diameter of vertical SAE NWs versus period for a V/III flux ratio of a) 4, b) 6, and c) 10. Flux ratios less than 4 are excluded due to a lack of vertical NWs. Dashed lines are visual guides only. Horizontal dash-dotted lines represent the length due to direct impingement of As. Representative error bars are indicated.

The diameter of NWs decreased with increasing V/III flux ratio. As discussed previously, nucleation occurs by the formation of In droplets created by direct impingement but also by diffusion from the oxide mask into the holes. This indicates that In supply for NW axial growth occurs by direct impingement and diffusion from the oxide mask and NW sidewalls. Higher V/III flux ratios are expected to hinder the In diffusion, resulting in the initial formation of smaller In droplets and therefore smaller diameter NWs. A similar process of In diffusion,

feeding the Au seeds in the initial stage of growth, could explain the diameter dependence observed in Figure 4.7e for the Au-assisted-VLS-SAE NWs.

Before concluding, we provide a brief comparison of MBE and MOVPE. There are some notable differences between the MBE and MOVPE growth technique. Growth by MBE occurs by direct impingement from atomic or molecular beams (e.g., In, As_2), and is limited by the In adatom diffusion or As_2 desorption. Due to the nature of the direct beams used in GS-MBE, growth may also be limited by the shadowing effects from neighboring NWs [41]. On the other hand, growth by MOVPE is determined by decomposition, diffusion and desorption of the precursors (e.g., trimethylindium and arsine). A good comparison of MOVPE and MBE can be obtained by the SAE growth of InAs NWs reported in Ref. [146] and [35]. MOVPE-grown InAs NWs in the SAE mode have been reported at a typical growth temperature between 520-560 °C and V/III ratio above 100 [34,143,146,157]. The larger V/III ratio in MOVPE compared to MBE is due to differences in the decomposition and diffusivity of the MOVPE precursors. Growth rates as high as 275 nm/min have been reported for MOVPE-grown InAs NWs [146], which are more than an order of magnitude larger than that reported for MBE [35].

An advantage of MOVPE is complete selectivity of the growth between the Si surface and the SiO_x mask (no InAs deposition is found on the mask) at all growth conditions above 490 °C [146]. In MOVPE, the selectivity is mainly governed by the lower precursor reactivity and higher desorption on the mask as compared to

the Si surface. Instead, growth selectivity in MBE relies on surface diffusion of In from the mask. For example, a growth temperature of 460 °C in SS-MBE resulted in InAs NW formation at predefined SAE holes but also in large InAs clusters on the SiO_2 mask due to reduced surface diffusion [35]. At 480 °C surface diffusion increased, resulting in a clean SiO_2 mask and InAs NWs only at the predefined holes. At 480 °C the length of the NWs began to decrease, and at 520 °C NW growth almost ceased due to thermal decomposition. Therefore, good selectivity was achieved in the range of 480-510 °C. The observation of a narrow temperature window is also observed for MOVPE-grown InAs NWs [36,144] but at higher growth temperatures due to the need for precursor dissociation [35].

The crystal quality of InAs NWs grown by SAE has not been extensively reported for MOVPE [146] or MBE [35]. However, optimization of the InAs crystal structure (minimization of planar defects such as stacking faults) have been demonstrated in the Au-assisted method for both MBE [54] and MOVPE [158] by appropriate growth parameter tuning. MBE techniques are expected to provide lower impurity incorporation from the ultrahigh vacuum environment.

4.5 Conclusions

InAs NWs were grown by GS-MBE on Si (111) substrates. Various growth modes were explored including randomly positioned and patterned Au-assisted VLS growth, VS growth, Au-assisted-VLS-SAE growth, and SAE growth. The SAE

method gave the highest yield of vertical NWs (72%) with an In impingement rate of 0.125 µm/hr, temperature of 440 ˚C, and V/III flux ratio of 4. The NW nucleation in the SAE method may have occurred with an In droplet, but quickly transitioned to a VS growth method with no In droplet at the tip of NWs. Subsequent axial growth of the SAE NWs occurs by the direct impingement of As_2 at the NW tip as well as the desorption of As_2 from the oxide mask, while In is supplied by direct impingement at the NW tip and by diffusion from the oxide mask and NW sidewalls.

The axial growth rate of NWs exceeded the In 2D equivalent growth rate of 0.125 µm/h (2.1 nm/min). The lowest axial growth rate was 6 nm/min in the VS growth mode, while the highest was 23 nm/min in the Au-assisted-VLS-SAE mode at a temperature of 440 ˚C and V/III flux ratio of 10. Au-assisted NWs, patterned and unpatterned, achieved comparable growth rates of 22 and 21 nm/min at a temperature of 330 ˚C and a V/III flux ratio of 4. However, this is a result of the smaller droplet diameters produced while annealing the Au on the substrates. Finally, the SAE mode also achieved a high axial growth rate of 22 nm/min at a V/III flux ratio of 10 and growth temperature of 440 ˚C.

5 Conditions for High Yield of InAs NWs on Silicon

5.1 Summary

This chapter contains work for our publication in Nanotechnology titled "Conditions for high yield of selective-area epitaxy InAs NWs on SiO_x/Si(111) substrates" (DOI: 10.1088/0957-4484/26/46/465301) [102]. In this report experimental data and a model are presented which define the boundary values of V/III flux ratio and growth temperature for droplet-assisted nucleation of InAs semiconductor NWs in selective-area epitaxy on SiO_x/Si (111) substrates by molecular beam epitaxy. Within these boundaries, the substrate receives a balanced flux of group III and V materials allowing the growth of vertically oriented NWs as compared to the formation of droplets or crystallites. All experimental results were obtained at McMaster, and simulations were performed by Vladimir Dubrovskii from ITMO University in Russia. This report attempts to describe the nucleation conditions for SAE NWs from Chapter 4. In doing so, it provides an understanding of the parameter space in which SAE InAs NWs can be grown with a high yield.

5.2 Introduction

III-V semiconductor NWs grown directly on silicon substrates have attracted considerable attention in recent years for improved photovoltaics [49]

and photodetectors [159] integrated with highly developed and low-cost silicon technology. Methods to grow NWs include the Au-assisted vapor-liquid-solid (VLS) [130–132], self-catalyzed or self-assisted VLS [6–18], catalyst-free VS [28,31,142,165–168], and selective-area epitaxy (SAE) [141,143,144,169] techniques. Among these methods, SAE seems to be the most promising as it enables the fabrication of NWs without the use of any foreign seed particle that may contaminate the NW. It also suppresses parasitic film growth on the substrate surface between the NWs and allows for positioned NW growth with controlled dimensions. However, one of the issues in SAE NW growth on silicon is the achievement of a high yield of vertically oriented NWs, as compared to the competing formation of droplets or irregular crystallites. In this chapter, a nucleation model is presented that predicts the V/III flux ratio and growth temperature boundaries for self-catalyzed VLS nucleation of vertical NWs on patterned silicon substrates. The model is compared to experimental results of SAE InAs NWs grown by molecular beam epitaxy (MBE), but should apply equally well to other material systems or growth methods such as metal-organic chemical vapor deposition (MOCVD) if the initial nucleation stage of NWs has a self-assisted VLS character.

5.3 Experimental Details

Growths were performed on boron-doped Si (111) substrates covered with 20 ± 2 nm of SiO_x deposited by chemical vapour deposition. Hexagonal arrays of patterned holes were formed in a spin-coated 120 nm thick ZEP 520A resist layer using a VISTEC EBPG 4200+ EBL system. After developing the resist, holes were etched in the oxide by reactive ion etching under 320 mTorr of CF_4 for 40 seconds, followed by a 45 s dilute BHF wet etch. The transferred pattern gave several 100 µm x 100 µm arrays with different hexagonal periods (360, 440, 520, 600, 1000 nm) and hole diameters (65, 83, 94 nm) on a single Si substrate. Substrates were loaded into the gas source MBE system immediately following the wet etch process to minimize oxide regrowth in the holes. In all cases, InAs NWs were grown by GS-MBE in which As_2 was supplied from a hydride (AsH_3) cracker cell operating at 950 ˚C, and In was supplied by an effusion cell.

SAE InAs NWs were grown in the MBE system with a constant In impingement rate of 0.125 µm/hr, and growth duration of 30 min. Four growth temperatures (400, 420, 440, 460 ˚C) were studied with a constant V/III flux ratio of 4. Five V/III flux ratios (2, 3, 4, 6, 10) were studied with a constant growth temperature of 440 ˚C. All growths were initiated by simultaneously opening In and As shutters and were cooled after growth without any In or As flux. Vertical yield (percentage of holes with a vertical NW) was determined using a JEOL 7000F SEM.

5.4 Results

SEM images are shown in Figure 5.1 for SAE InAs growth with a hole diameter of 83 nm, period of 360 nm, and a growth temperature ranging from 400 to 460 ˚C. The average NW yield at 400 ˚C, 420 ˚C, 440 ˚C and 460 ˚C was 26, 39, 63, and 2%, respectively. The results were similar with different hole diameter or period. At the lowest growth temperature of 400 ˚C (Figure 5.1a), the oxide holes were mostly filled with one or more tilted NWs, or NWs crawling out of the holes onto the oxide surface. Many crystallites were also observed on the oxide surface. At 420 ˚C (Figure 5.1b), fewer crystallites grew in the oxide holes, and were replaced with more vertical NWs. Crystallites no longer formed on the oxide surface and instead small (~30 nm) droplets remained. At 440 ˚C (Figure 5.1c), no crystallites or droplets nucleated directly on the oxide surface and the vertical NW yield was highest. Finally, at 460 ˚C (Figure 5.1d), In droplets formed in the holes and no NWs grew.

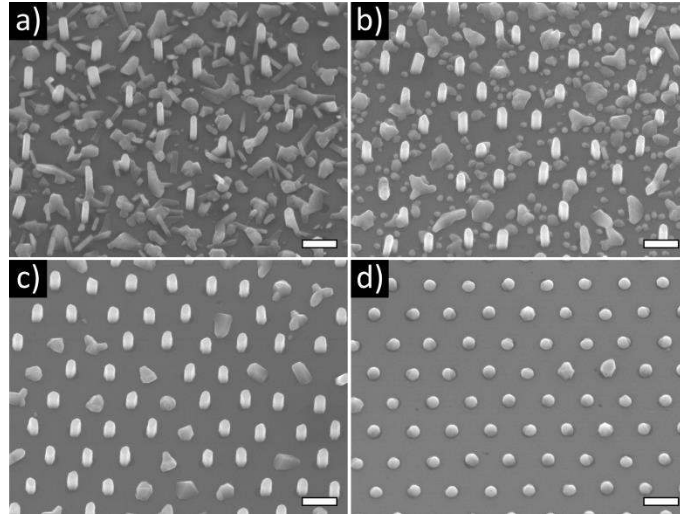

Figure 5.1: SEM images for SAE NWs with a V/III flux ratio of 4 and a growth temperature of (a) 400 ˚C, (b) 420 ˚C, (c) 440 ˚C and (d) 460 ˚C. Scale bars are 300 nm. Reproduced with permission from [101].

The effect of V/III flux ratio was investigated at a constant temperature of 440 ˚C where the yield of vertical NWs was greatest. The V/III flux ratio was varied by adjusting the As_2 flux, keeping the In impingement rate fixed at 0.125 µm/h. SEM images of the SAE growths in Figure 5.2a-e show the results for V/III flux ratios of 2, 3, 4, 6, and 10 at a period of 360 nm and a hole diameter of 83 nm where the yield of vertical NWs was 1, 10, 63, 37 and 28%, respectively. The results were similar for different hole diameter or period. At a V/III flux ratio of 2, the holes were filled with In droplets. At a V/III flux ratio of 3, crystallites appeared to form in the holes. Finally, at V/III flux ratios above 4, NWs appeared with a length that increased and a diameter that decreased with V/III flux ratio.

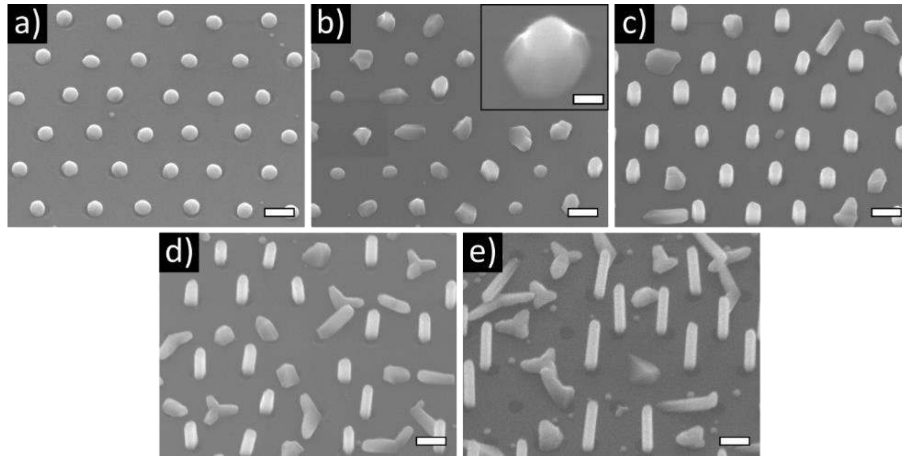

Figure 5.2: SEM images for SAE InAs NWs grown at 440 ˚C with V/III flux ratio of (a) 2, (b) 3, (c) 4, (d) 6 and (e) 10. Scale bars are 200 nm. Inset in (b) shows an SEM image of a crystallite with a droplet remaining on top. Scale bar is 50 nm.

We note that there were no droplets observed on the NW tips after growth, verified in TEM but not shown here, similar to Ref. [142]. In our samples, no As flux was impinging during the cool-down procedure after NW growth. Any In droplet that may have been present at the tip of the NWs during growth would have remained there without As present during cool down to consume the droplet [170]. Instead, the absence of an In droplet indicated that none was present in the later stages of growth. On the other hand, SEM images of the NWs at the very beginning of growth, such as the inset in Figure 5.2b, showed an In droplet on top. These results indicate that NW nucleation started from the formation of In droplets in the holes, but that growth quickly transitioned to the VS mode, similar to Ref. [146].

5.5 Model and Discussion

The system considered is a regular array of cylindrical holes in a SiO_x layer with a given period A, radius R_0 and height H_0, as shown in Figure 5.3. Deposition starts at the growth temperature T by simultaneously turning on the group V and III fluxes. These are characterized by the atomic arrival rates $\chi_5 I_5$ and $\chi_3 I_3$ per unit surface area per unit time, with I_5 and I_3 as the atomic fluxes, and χ_5 and χ_3 as the coefficients accounting for the beam geometry in MBE (or the precursor cracking efficiency in MOCVD) for the group V and III growth species, respectively. Desorption of group III atoms and surface diffusion of group V atoms can be neglected [8,41,170–172] as well as secondary fluxes of group V atoms due to desorption from the oxide [171]. In this case, the number of group V (labeled “5”) and group III (labeled “3”) atoms in each hole changes with time according to:

$$\frac{dN_5}{dt} = \pi R_0^2\left(\chi_5 I_5 - I_5^{des}\right); \ \frac{dN_3}{dt} = \pi (R_0 + \lambda_3)^2 \, \chi_3 I_3 \qquad (5.1)$$

where $I_5^{des}(T)$ is the temperature-dependent desorption rate of group V atoms from the hole and $\lambda_3(I_5, T)$ is the effective collection length of group III atoms which depends on the group V flux and growth temperature. Whatever is the λ_3 value on bare SiO_x, the pattern period A fixes the maximum collection length for the array of the holes, which equals $\frac{A}{2} - R_0$ if the array is a square grid. We also note that the I_5^{des} in Equation 5.1 relates to surface adatoms of a group V element which is of course relevant in the initial stage of filling the holes. However, in a later stage the arsenic desorption could depend on the state of an In-As alloy in

the hole (i.e., arsenic atoms dissolved in liquid indium, stoichiometric solid InAs or even a mixture of liquid indium and solid InAs). In the first approximation, here we use a uniform model parameter I_5^{des} regardless of the state of an InAs alloy to quantitatively explain the data, while the corresponding refinement of the model will be presented elsewhere.

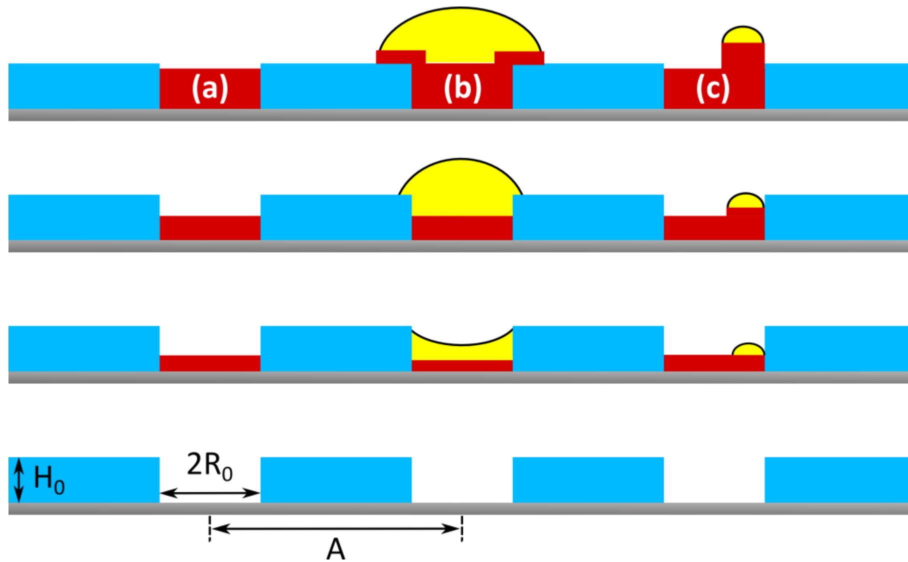

Figure 5.3: Illustration of possible scenarios of filling the holes: (a) excessive group V flux producing III-V crystallite; (b) excessive group III flux producing large metal droplet and irregular crystallites at the periphery of the hole, and (c) balanced group V and III fluxes producing a small droplet and one NW per hole.

We now consider three possible scenarios of filling the holes, as shown in Figure 5.3. If more group V than group III atoms arrive to the hole, it will be filled with stoichiometric III-V crystal and no liquid droplets can be produced (case (a) in Figure 5.3). In these conditions, no VLS nucleation of NWs is possible and their nucleation can only occur by the Volmer-Weber growth mode without a droplet.

Most likely these conditions result in irregular crystallite growth above the oxide such as those seen in Figure 5.1a and Figure 5.2e.

When the group III flux into the hole is too high, the initial droplet with a fixed contact angle $\beta_0 \leq \frac{\pi}{2}$ will spread over the entire width of the hole and form a flat or meniscus interface with the vapor. This inequality seems relevant in view of a low surface energy of liquid group III metals [173] and of the liquid-solid interface between group III metals and III-V crystals [172]. As the III-V crystal and the group III liquid volumes keep increasing, the liquid will be pushed away from the hole and irregular crystallites or multiple NWs may emerge at the periphery of the hole on the oxide surface (case (b) in Figure 5.3). This process is definitely not expected to yield one straight NW per hole because the droplet is too large, and the liquid-solid interface may not be planar. Figure 5.1d and Figure 5.2a best exemplify the case where the group III flux into the hole is too large.

The best scenario for a high yield of straight NWs is therefore given by case (c) in Figure 5.3 in which the droplet base radius remains smaller than the radius of the hole by the moment of time at which the hole is filled by the III-V crystal. In this situation, the NW growth beneath the droplet most probably starts before filling the hole.

Based on these simple considerations, we formulate the following two conditions for NW nucleation:

(i) The group III flux into the hole must be larger than the group V flux to enable the formation of a metal droplet:

$$\frac{dN_3}{dt} > \frac{dN_5}{dt} \tag{5.2}$$

(ii) The droplet radius $R_* = R(t_0)$ should be smaller than R_0 by the time t_0 when the hole is filled with III-V crystal so that the droplet rests on III-V surface but not on SiO_x surface:

$$R_* = R(t_0) < R_0 \tag{5.3}$$

Relating the number of group III atoms or III-V pairs to the liquid or crystal volumes through the droplet shape and the corresponding elementary volumes as in Ref. [142], Equation 5.1 can easily be solved and the conditions given by Equation 5.2 and 5.3 can be quantified in terms of the V/III flux ratio, $F = I_5/I_3$, versus the temperature-dependent parameters and geometry. The solutions for the incubation time t_0 and the size of initial droplet R_* are given by:

$$t_0 = \frac{H_0}{\Omega_{35}(\chi_5 I_5 - I_5^{des})};$$
$$R_*^3 = \frac{R_0^2 H_0}{c}\left[\min\left\{\frac{A^2}{4R_0^2};\left(1+\frac{\lambda_3}{R_0}\right)^2\right\}\frac{\chi_3 I_3}{\chi_5 I_5 - I_5^{des}} - 1\right] \tag{5.4}$$

Here, Ω_{35} is the elementary volume of a III-V pair in solid and $c = \left(\frac{\Omega_{35}}{3\Omega_3}\right) f(\beta_0)$ is the effective aspect ratio of group III droplet, with Ω_3 as the elementary volume in liquid and $f(\beta_0) = (1 - \cos\beta_0)(2 + \cos\beta_0)/(1 + \cos\beta_0)\sin\beta_0$ as the geometrical function relating the volume of a spherical cap droplet V_d to the cube

of its base R through the contact angle β_0 as $V_d = (\pi/3)f(\beta_0)R^3$. The minimum of the two values in Equation 5.4 for R_* arises due to the fact that the collection of group III adatoms is limited either by the diffusion length or the distance between the holes.

The NW nucleation conditions can be expressed as the inequality for the V/III flux ratio:

$$F_{min} < F < F_{max} \tag{5.5}$$

The lower limit corresponds to a very large droplet, and the upper limit corresponds to no droplet in the hole. The temperature and geometry-dependent limits for the V/III flux ratio are given by:

$$\begin{gathered} F_{min} = \frac{p}{1+a} + q; F_{max} = p + q; \\ p = \min\left\{\frac{A^2}{4R_0^2}; \left(1 + \frac{\lambda_3}{R_0}\right)^2\right\}\frac{\chi_3}{\chi_5}; q = \frac{I_5^{des}}{\chi_5 I_3}; a = c\frac{R_0}{H_0} \end{gathered} \tag{5.6}$$

where p is determined by geometry and/or the diffusion length of indium adatoms and q gives the effective V/III flux ratio. The q parameter can also be presented as $q = I_5^{des}F_0/\chi_5 I_{5,0}$, where $I_{5,0}$ corresponds to the reference group V flux and $F_0 = I_{5,0}/I_{3,0}$ to the reference V/III flux ratio if the latter is changed by varying the group V flux at a constant group III flux $I_{3,0}$. The temperature dependence of the group V desorption rate should be of the Arrhenius type: $I_5^{des} \propto \exp(-E_{des}/k_B T)$, where E_{des} is the activation energy for In desorption and k_B is the Boltzmann constant. The effective diffusion length of group III adatoms on SiO_x is taken in the

form $\lambda_3 \propto (1/I_5)\exp(-E_\lambda/k_B T)$. Here, we assume the Arrhenius temperature dependence of thermally activated diffusion with the activation energy E_λ and the indium diffusivity decreasing inversely proportional to the group V flux [174]. The latter dependence is valid if the surface concentration of arsenic atoms is proportional to I_5 and InAs crystallites emerge irreversibly whenever two indium and arsenic adatoms meet on the oxide surface [162]. Alternatively, one can consider the macroscopic nucleation scenario for InAs crystallites in which the indium diffusion length decreases exponentially with increasing group V flux [175]. This would not affect qualitative conclusions drawn below.

Equations 5.6 allow one to construct the $F - T$ maps of relevant growth parameters for a given geometry (A, R_0, H_0) and material (described in this model by the contact angle β_0, the group V desorption rate $I_5(T)$ and the group III diffusion length $\lambda_3(I_5, T)$). The example for our experimental geometrical parameters ($A = 360\ \mathrm{nm}, R_0 = 41.5\ \mathrm{nm}, H_0 = 20\ \mathrm{nm}, \chi_5 = 0.82$ relating to 35° incident angle of As$_2$ beam, $\chi_3/\chi_5 = 1$) and with $\lambda_{3,0} = 140\ \mathrm{nm}$ at $F_0 = 4$ and $T_0 = 440\ °\mathrm{C}$, $I_5^{des}/I_{5,0} = 0.4$ at 440 °C, $E_\lambda = 0.52$ eV and $E_{des} = 2.6$ eV are shown in Figure 5.4. With these plausible parameters, our model reproduces quite well the experimental data. In particular, at low temperatures the nucleation region is limited by low In diffusivity so that at $F = 4$, InAs NWs can be obtained only above ~ 390 °C, while at high temperatures (larger than 450 - 460 °C depending on the period for $F = 4$) the In-assisted nucleation is limited by desorption of As. At a fixed temperature of 440 °C, the NW growth is possible only

above a critical $F \cong 3$ and continues up to $F \cong 10$. Other factors (oxide uniformity and substrate preparation) not described here could further define the yield within these boundary regions. We note that the shape of the nucleation domain on the map is general for all III-V materials while the actual boundary values will depend on the NW and substrate material.

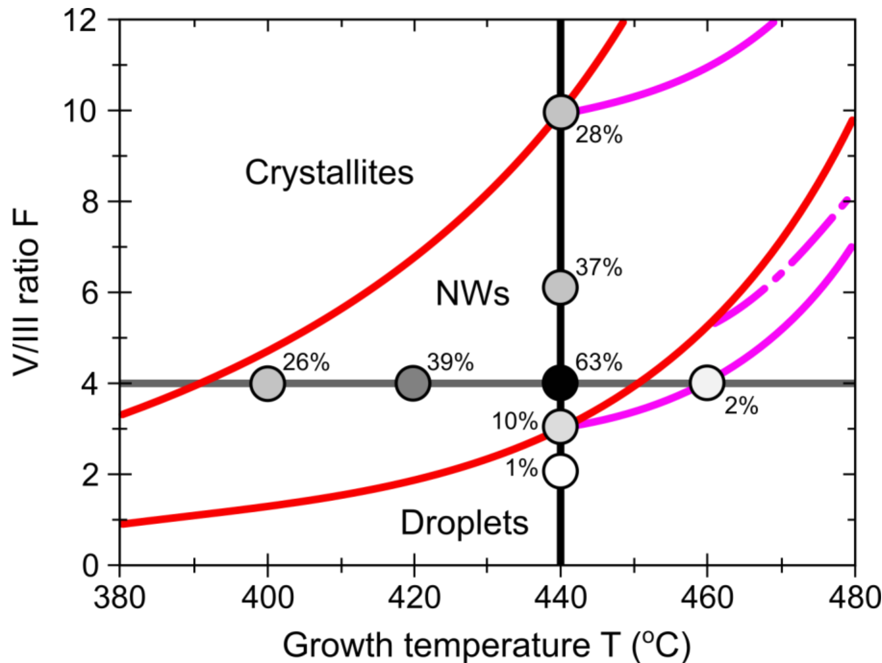

Figure 5.4: Growth temperature – V/III flux ratio map for the experimental geometry of MBE-grown SAE InAs NWs on Si. Red lines correspond to the In collection limited by the diffusion length of In adatoms and magenta lines show the period limitation (solid line: A = 360 nm, dash-dotted line: A = 440 nm; for larger periods this limitation becomes ineffective). NW (NW) nucleation region is within the domain restricted by the curves. Symbols show the experimental points with the measured yields of vertical InAs NWs.

We emphasis that the above considerations apply only to the case where the NW nucleation is assisted by In droplets which are subsequently consumed by an excess As flux to the NW tops. Even though crystallites may nucleate at the

beginning of SAE growth of III-V NWs, they may well develop into NWs. In such a mode, which obviously does not require a foreign metal droplet, the NW growth may take place spontaneously as in GaN NWs [165–168] or by "twin-defect induced" mechanism as in GaAs NWs [176]. Under such growth modes the vertical yield is not expected to follow the described dependence on the growth conditions. In Ref. [161], the authors did not find a strong dependence of the vertical yield of Ga-catalyzed GaAs NWs on the V/III ratio; however, our process is different because no In pre-deposition is used prior to SAE growth. Rather, the In-assisted nucleation of SAE InAs NWs is closer to the Ga-assisted nucleation of GaAs NWs on unpatterned Si(111) substrates covered with a native oxide layer [162]. In this case, the nucleation of Ga droplets occurs in the holes that form spontaneously due to thermal evaporation of the oxide layer and competes with parasitic GaAs growth. In Ref. [162], the yield of GaAs NWs versus parasitic crystallites was found to be strongly dependent on the V/III ratio, as in our case.

Finally we note that the best vertical yield obtained here (63%) is noticeably lower than in the case of Ga-catalyzed GaAs NWs on SiO_x/Si(111) substrates (e.g., more than 90% in Ref. [43]). In Ref. [43] the yield of GaAs NWs on silicon decreased below 60% with a gallium pre-deposition flux of 1 ML s^{-1} for less than 30 seconds. None of our growths included an In pre-deposition step. It is likely that our yield was relatively low as a result of unoptimized etching and pre-deposition steps. However, this does not affect the main conclusions of this chapter.

5.6 Conclusion

In conclusion, a nucleation model has been presented that may be applied to many SAE III-V NWs grown by either MBE or MOCVD if their nucleation is assisted by group III droplets. The model describes a region in which vertical yield is achievable depending on temperature and V/III flux ratio. Some model parameters can be further refined for a particular material system or growth conditions. The model agrees well with experimental results obtained through the SAE growth of InAs NWs on silicon substrates by MBE. We have shown that a high yield of vertically oriented SAE NWs is expected when the growth starts in the VLS mode with a group III droplet whose size is smaller than that of the hole. After this nucleation step, the droplet is consumed due to a reduced supply of In and the growth acquires a purely SAE character. Non-monotonic dependences of the vertical NW yield on both temperature and V/III flux ratio in this growth mode allows one to select the optimum growth conditions resulting in the highest yield for a given epitaxy technique, material and geometry.

6 Multispectral Absorptance in InAsSb Arrays

6.1 Summary

This chapter contains work from our publication in Nano Futures titled "Multispectral absorptance from large-diameter InAsSb NW arrays in a single epitaxial growth on silicon" (DOI: 10.1088/2399-1984/aa9015) [103]. New work has been added since the original publication in Section 6.4 to better explain the fractional flux study, and to include Raman analysis and IV measurements. In this study, multiple InAsSb NW arrays were grown simultaneously on silicon by MBE with NW diameter controlled by the NW period (spacing between NWs). This is the first such study of patterned InAsSb NWs where control of NW diameter and multispectral absorption are demonstrated. The antimony flux was used to control axial and radial growth rates using a selective-area catalyst-free growth method, achieving large diameters, spanning 440–520 nm, which are necessary for optimum IR absorption. Fourier transform IR spectroscopy revealed IR absorptance peaks due to the HE_{11} resonance of the NW arrays in agreement with optical simulations. Due to the dependence of the HE_{11} resonance absorption on NW diameter, multispectral absorption was demonstrated in a single material system and a single epitaxial growth step without the need for bandgap tuning. This work demonstrates the potential of InAsSb NWs for multispectral photodetectors and sensor arrays in the short-wavelength IR region.

6.2 Introduction

At present, the most widely used material system for high performance infrared (IR) photodetection is $Hg_{1-x}Cd_xTe$ (MCT) [83,86,177]. MCT has a composition-dependent, tunable and direct energy bandgap that spans the IR spectrum from short-wavelength infrared (SWIR) to very-long-wavelength infrared (VLWIR) [83]. The change in lattice constant with composition is also negligible, allowing for the fabrication of high quality graded and layered MCT thin film heterostructures with negligible lattice-mismatch defects [177]. However, MCT suffers from bulk, surface, and interface instabilities due to weak Hg-Te bonds [83]. The commonly used CdZnTe substrate, while lattice-matched to MCT, is expensive, and suffers from integration issues with Si readout integrated circuits (ROICs) [82,177]. Si substrates were investigated as an alternative, using a CdTe/ZnTe buffer layer; however, the resulting MCT thin film quality is poor compared to MCT thin films grown on CdZnTe substrate [82]. The above drawbacks have stimulated the investigation of alternative material systems for IR photodetection [83,177].

III-V NWs are a potential alternative to MCT or other material systems for IR photodetection. III-V NWs can accommodate lattice-mismatch strain by elastic relaxation at the NW sidewalls, allowing for epitaxial growth on lattice-mismatched substrates and therefore monolithic integration with Si ROICs [49]. III-V NWs can incorporate radial and axial homo- and hetero-junctions for efficient collection of photogenerated carriers. Due to the presence of radial resonant

waveguide modes, NWs also have the capability of producing absorption bands with narrow spectral ranges by tuning the NW geometrical parameters [45,46,80]. Peaks in the resonant absorption bands can exceed absorption from a thin film of the same material and thickness. These advantages eliminate the need for additional spectral filters above the photodetector, or vertical stacking of heterostructures of different bandgaps, for a multispectral detector [80].

Recently, absorptance in vertical NW arrays were simulated for GaAs, InP, InAs [45], and InSb [46] and found to be dominated by guided mode resonances. Guided modes arise in the NW because of its radially symmetric boundary conditions imposed on the electromagnetic wave solutions. Incident light near a resonant wavelength couples efficiently to an HE_{1n} mode in the NW, significantly increasing the absorption in the material [74]. This unique phenomenon results in a high absorptance peak with a narrow full-width at half-maximum (FWHM) and a spectral position controlled primarily by the NW diameter [45,46,80]. The study of optimized InSb NW geometrical properties indicated the need for NW diameters from 200 – 550 nm to achieve sharp resonance absorptance spectra in the SWIR region [46]. Svensson et al. [99] demonstrated the diameter-dependence of photocurrent from InAsSb NWs grown on InAs substrates by metal-organic vapor phase epitaxy (MOVPE). They found a red-shift in photocurrent measurements corresponding to an increase in average NW diameters for randomly dispersed arrays. Compositional changes were found to

affect only the magnitude of the absorptance, while it had negligible influence on the peak position.

In this study, we present large diameter catalyst-free InAsSb NWs grown on a Si substrate by selective-area MBE. This is the first study of patterned InAsSb NWs where control of NW diameter and multispectral absorption are demonstrated. NWs were grown simultaneously in four separate arrays on the same Si substrate, each with a different diameter (440, 475, 505 or 520 nm) and period (1000, 1500, 2000 or 3000 nm). NWs are shown to have consistent core-shell compositions, and diameters that are controlled by the NW array period. Spectroscopy measurements reveal absorptance peaks in the SWIR region due to HE_{11} guided mode resonances and are confirmed by theoretical simulations. Fabrication of the four arrays occurred in a single epitaxial growth; thus, we have achieved multispectral absorptance without the need for bandgap tuning, paving the way towards NW-based multispectral IR photodetectors and sensors.

6.3 Experimental Details

InAsSb core-shell NWs were fabricated in a gas source MBE system in which Sb_2 was supplied by a 3-stage effusion cell operating at 565 ˚C, 800 ˚C and 930 ˚C for the crucible, valve and cracker, respectively. Indium was supplied by a standard effusion cell and As_2 was supplied from a hydride (AsH_3) gas cracker operating at 950 ˚C. Growth was performed in three stages; a short (50 nm) InAs

stem for optimized yield and epitaxy [101], an InAsSb core with a Sb beam equivalent pressure (BEP) of 1 x 10^{-7} Torr, and an InAsSb shell with an Sb BEP of 2.84 x 10^{-7} Torr to achieve 5% and 14% fractional flux (flux of Sb relative to the total group V flux), respectively. In the fractional flux (FF) study described below, 5% FF produced InAsSb NWs with 23% Sb, and a 14% FF resulted in 33% Sb. The lower Sb composition core, which was in an axial growth regime, achieved a NW length more than 1 μm. The higher Sb composition shell was in a radial growth regime to enlarge the diameter of the NWs to the desired value (440 nm to 520 nm, depending on the NW period) for strong IR absorptance. InAs stems were grown for 5 minutes at a V/III flux ratio of 4 while the InAsSb core and shell were each grown for 2 hours at a V/III flux ratio of 10. All growth stages had an In impingement rate of 0.125 μm/hr and a substrate temperature of 440 ˚C. NWs were grown on a low boron-doped (<1.33 x 10^{14} cm^{-3}) Si (111) substrate following the catalyst-free selective-area epitaxy (SAE) growth method [101]. Electron beam lithography (EBL) and etching precisely defined the position of holes in a 20 nm SiO_x layer deposited by chemical vapor deposition (CVD). The EBL pattern was comprised of four 100 μm x 100 μm arrays each with a different triangular lattice period (1000, 1500, 2000 and 3000 nm; Figure 6.1a) but the same oxide hole diameter (90 nm; Figure 6.1b).

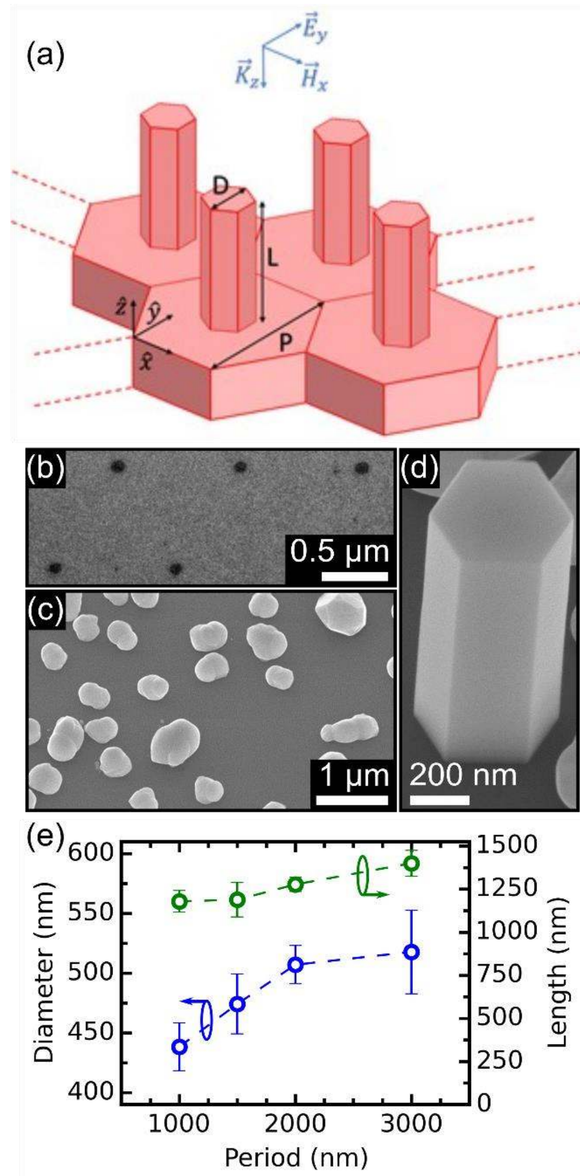

Figure 6.1: Morphological aspects of NW arrays. (a) Schematic of NWs in a triangular lattice with hexagonal cross-sections and the diameter (D), period (P), and length (L) indicated, (b) plan view SEM of 1000 nm period array of holes in the Si oxide, (c) droplets and crystallites on the oxide away from the NW arrays, (d) 30° tilted SEM of a core-shell NW from 1000 nm period array, and (e) trends of diameter and length versus array period. Error bars represent standard deviations.

FIB lamellas were prepared on a Zeiss NVision40 instrument. This FIB uses a focused beam of gallium atoms to extract a lamella and thin it to ~100 nm for

TEM analysis. Ultramicrotome was also performed using a diamond blade to cut ~100 nm slices perpendicular to the growth axis. NW morphology was characterized using a JEOL 7000F SEM. NW structure and composition were characterized by a JEOL 2010F scanning transmission electron microscope (TEM) with energy-dispersive X-ray spectroscopy (EDX). Optical characterization was performed by Fourier transform infrared spectroscopy (FTIR) using a BRUKER Hyperion 3000 system with a halogen source and an MCT detector with an operating wavelength range of 1.25 – 16 µm. Infrared light was incident and collected through a 15x objective lens with a numerical aperture (NA) of 0.4. A knife-edge aperture was set to an area just less than 100 µm x 100 µm to ensure that absorptance data only included the NW array. The same aperture setting was used for all background measurements. All FTIR measurements were performed with the source normally incident on the NW array (front-side illuminated) and at room temperature. The FTIR spectra were smoothed using a Savitzky-Golay filter to remove high frequency noise.

Optical simulations of the NW absorptance were performed using the finite element method (FEM) in COMSOL 3.5a RF Module. Periodic 2D triangular lattice NW arrays on a Si substrate were simulated using the measured average diameter, average length, and period of the NWs within a given array. The NW cross-sectional area was hexagonal, representative of the grown NWs. A schematic of this array is presented in Figure 6.1a. The real part ($n(\lambda)$) of the complex refractive index of the $InAs_{1-x}Sb_x$ NWs was acquired from Paskov [178].

The imaginary part (k(λ)) of the complex refractive index of the $InAs_{1-x}Sb_x$ NWs was acquired from Stringfellow and Greene [179] and is like that of InAs and InSb below λ=3 μm as acquired from Palik [179]. The complex refractive index for Si was acquired from Palik [180]. The medium surrounding the NWs was air with n=1. A perfectly matched layer (PML) subdomain was used above the NW geometry and below the substrate to simulate an infinitely extending air medium above the NW array and an infinitely extending Si substrate below the NW array. A port was set on an "assembly pair" constructed above the NW array to generate Y-polarized incident waves at normal incidence to the NWs (parallel to the NW axis). The absorptance spectra of the NW array showed negligible dependence on polarization since the NW cross-section is nearly rotationally symmetric. Wavelength-dependent absorptance was calculated using Equation 2.11 where reflectance was at the top of the NW array and transmittance was found at the array-substrate interface.

6.4 Results and Discussion

6.4.1 Fractional Flux Study

Several growths were performed before the full core-shell structure to gain an understanding of the underlying growth mechanisms. First, an Sb fractional flux (FF) study was completed to identify the effects of increasing Sb on the SAE InAsSb

NW morphology. Fractional flux was defined as the flux of Sb relative to the total group V flux during MBE growth:

$$\mathrm{FF} = \frac{\Phi_{\mathrm{Sb}}}{\Phi_{\mathrm{Sb}} + \Phi_{\mathrm{As}}} \quad (6.1)$$

where Φ_{Sb} and Φ_{As} are the fluxes of antimony and arsenic respectively. All growths had an In impingement rate of 0.125 µm/hr, a substrate temperature of 440 ˚C, and a growth time of 1 hour. The substrates were p-type Si(111) with a resistivity less than 0.005 Ω-cm ($N_A > 2 \times 10^{19}$ cm^{-3}). All growths were initiated with an InAs stem for improved yield conditions. The overall V/III flux ratio was kept constant at 10 by proportionally decreasing the flux of As as the flux of Sb increased (see Section 9.2 of Appendix for calculations). Table 6.1 gives the BEP for Sb in the four FF growths, which are the only differing parameters in this study.

Table 6.1: Parameter variation in the four FF growths shown in Figure 6.2.

Figure 6.2	**FF (%)**	**BEP_{Sb} (10^{-7} Torr)**
a)	5	0.96
b)	10	1.91
c)	14	2.84
d)	23	4.68

As FF was increased, the NWs decreased in length and increased in diameter. In Figure 6.2a (FF = 5%) the NWs are longer than they are wide but in Figure 6.2d (FF = 23%) the diameter is approximately 3x larger than the length. Thus, increasing Sb flux had the effect of reducing axial growth rate of the NWs and increasing the radial growth rate.

Anyebe et al [181] found a similar inverse proportionality between Sb flux and the resulting NW lengths. They grew InAsSb NWs on Si(111) substrates using the self-assisted VLS method and varied FF from 0% - 5%. At 0% FF (InAs), the NWs were 3 µm tall and 70 nm in diameter. At 5% FF, the NWs were 100 nm tall and roughly 200 nm in diameter although they were mostly coalesced into a film. They attribute such large change in morphology to the Sb surfactant effect. In these droplet-nucleated NWs the segregated (floating) Sb changed the wetting, expanding the initial droplet, and nucleating larger diameter NWs. During growth the axial growth rate was further reduced by segregated Sb on the droplet since this is expected to induce lattice site blocking on the growth front [182]. Radial growth was attributed to two main factors. First, the lengths and diameters of diffusion-limited NWs are inversely proportional. This relationship dictates that as the axial growth rate is suppressed the radial growth rate will be increased. Second, Sb segregation on the sidewalls could increase the sidewall nucleation, thereby increasing radial growth rate.

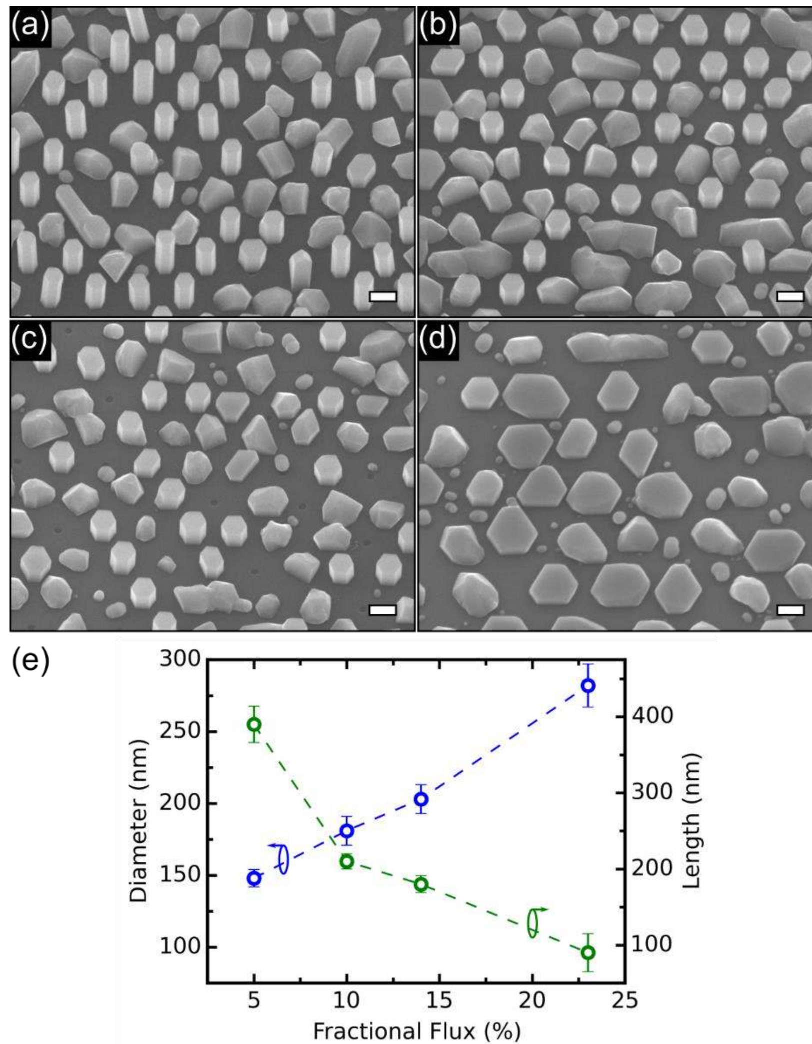

Figure 6.2: Fractional flux growths. 30-degree tilted SEM images of InAsSb NWs with a fractional flux of (a) 5%, (b) 10%, (c) 14%, and (d) 23%. Scale bars are 200 nm. (e) Length and diameter versus fractional flux. (a) – (c) are shown with a period of 360 nm and (d) is shown with a period of 520 nm.

Although our growths were performed without a droplet, it is still likely that Sb is site blocking on the top (111) surface of the NWs [183]. Otherwise, the very large top [111] facet in Figure 6.2d would capture a significant amount of direct flux regardless of any adatom diffusion length limitations. Recent simulations by Vladimir Dubrovskii from ITMO University in Russia (unpublished

results) indicate that the increased radial growth rate with increasing FF is related to difficult nucleation of adatoms on the top facet of the NW. The concentration of In adatoms on the top facet increases because they are unable to nucleate, which leads to an increased diffusive flux away from the top and increased nucleation on the side facets. These simulations were based on our FF growth study and there is a publication in progress for the results. It should be noted that although our growths were all droplet nucleated and therefore Sb could affect the wetting conditions, Sb is not introduced into the MBE until after the InAs stem growth and extinction of the nucleating droplet. Furthermore, a larger nucleation droplet would not explain the radial growth of the shell in the core-shell structure described below.

FF of 5% and 14% had Sb compositions of 23 and 33 atomic percent (at %), respectively, as discussed below. This indicates a high incorporation rate of Sb into the growing NW facets, which is also reflected in the literature for similar MBE growths [63,95,181]. Thin film antimonide growths have also demonstrated an Sb incorporation dominance over As, which is attributed to the temperature-dependent desorption rate of As [184]. It is also interesting to note that the average volume of each NW for FF = 5% is nearly double that of FF = 23%. Given that these growths are identical other than their group V fluxes, a decrease in volume indicates that Sb is hindering the incorporation of other growth species.

EDX measurements in TEM were used to measure the compositions of Sb in $InAs_{1-x}Sb_x$ NWs. Owing to the destructive nature of TEM preparations, only two

of the four FF NW arrays were analyzed in TEM. Compositions for FF = 5% and 14% were found to be x = 0.23 and 0.33 respectively. Raman analysis was performed on the remaining FF growths (FF = 10% and 23%) to estimate their compositions. EDX measured compositions were used to create a predictive trendline that correlated Raman peak positions and NW compositions. Pure InAs NWs (x = 0) were also used. The Renishaw micro-Raman system described in Section 2.5 was used to extract Raman shifts for all NW arrays.

Figure 6.3 shows the experimental Raman data for InAs and InAsSb NWs. Each set of data was fit with multiple Lorentzian peaks, indicated by the three solid curves. LO (blue) and TO (red) peaks for InAs NWs match closely with other reported values, and show a TO downshift corresponding to WZ stacking [63,185–187]. Two-mode behaviour can be seen in all the ternaries with the InSb-like TO+LO (green) mode near 180 cm^{-1}. All InAs and InSb modes shifted according to composition but the clearest was the downshift of the InAs LO mode. This mode shifts from ~240 cm^{-1} for InAs to ~225 cm^{-1} for the highest FF, and therefore is the most sensitive to changes in composition.

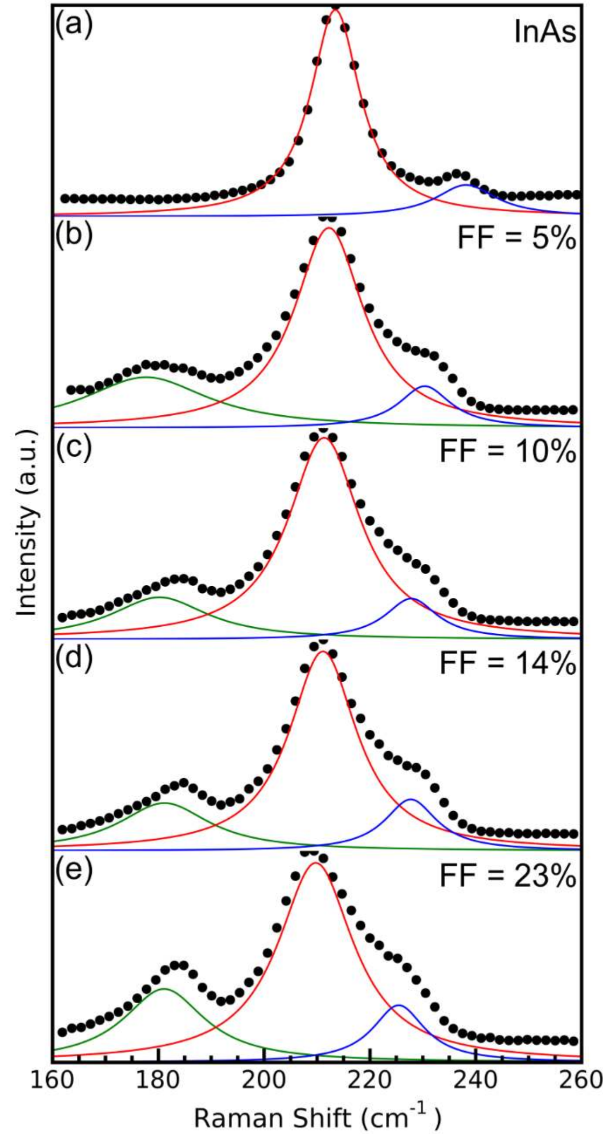

Figure 6.3: Raman shifts for NW arrays of (a) InAs, and InAsSb with FF of (b) 5%, (c) 10%, (d) 14%, and (e) 23%. Experimental Raman data is given by black dots, and the solid curves are fitted Lorentzian profiles such that the three (or two) peaks add up to match the experimental data. Green curve is the InSb-like TO+LO mode, red is InAs TO mode, and blue is InAs LO mode.

Raman compositional analysis of thin film InAsSb (100) has been reported previously [187]. Li et al [187] identified a linear LO and TO correlation with increasing Sb content given by Equations 6.2 and 6.3.

$$\nu_{LO} = 238 - 32 * x \quad (6.2)$$

$$\nu_{TO} = 219 - 27 * x \quad (6.3)$$

where ν_{LO} and ν_{TO} are the LO and TO Raman peaks, respectively. These equations are compared to our data in Figure 6.4. InAs-LO peaks match the reference equation well, but InAs-TO peak shifts do not. Specifically, the InAs NW TO peak (Sb composition, x=0) does not match the trendline. Likely, this is due to the TO downshift from WZ NW stacking since our InAs NWs have many stacking faults (alternating WZ and ZB structure) while the InAsSb NWs are predominantly twinned zincblende [185].

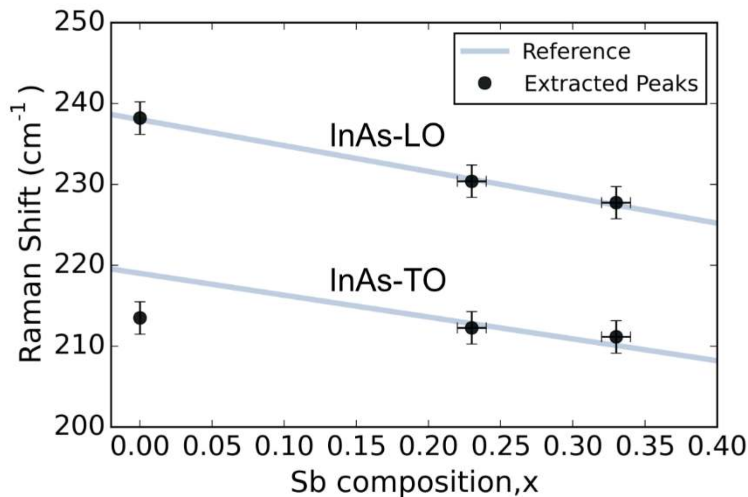

Figure 6.4: LO and TO peak position shifts with Sb content in InAsSb NW arrays. Equations from reference [187] are shown in light grey, experimental data from this study are shown in black. Error bars for composition are from the EDX measurement error (1%). Raman shift error bars are estimated from the fits.

The above analysis indicates that we can use the InAs-LO mode and Equation 6.2 to predict the remaining FF compositions (see Table 6.2). The

relationship between FF and NW composition suggests there is a saturating incorporation rate of Sb, possibly due to the VS NW growth mode in these conditions.

Table 6.2: Quantified Raman analysis of InAsSb NWs with all TO and LO shifts and their corresponding compositions.

NWs	**FF (%)**	**InSb TO+LO (cm^{-1})**	**InAs TO (cm^{-1})**	**InAs LO (cm^{-1})**	**EDX Sb (x)**	**Raman Sb (x)**
InAs	0	-	213.5	238.2	0	0
InAsSb	5	177.7	212.3	230.4	0.23	0.238
InAsSb	10	180.2	211.4	227.8	-	0.318
InAsSb	14	181.1	211.1	227.7	0.33	0.321
InAsSb	23	181.1	209.8	225.5	-	0.392

6.4.2 Core-Shell Growths

Next, the FF = 5% growth was repeated for a two-hour growth time. This will later make up the core of the core-shell NW. Figure 6.5a shows an array of core NWs with average lengths of 850 nm and average diameters of 160 nm. Comparing to the one-hour FF = 5% growth (L = 390 nm, D = 150 nm) the axial growth rate over the additional one-hour period is 7.8 nm/min while the radial growth rate is 0.2 nm/min. For reference, the indium flux is set at a two-dimensional equivalent growth rate of 2 nm/min. Thus, we found an axial growth regime that has minimal radial expansion.

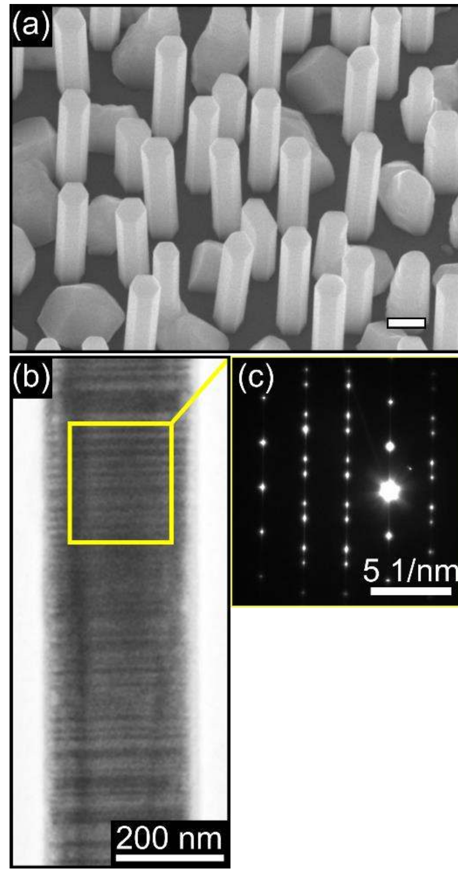

Figure 6.5: Core growth of InAsSb without subsequent shell growth. (a) 30-degree tilted SEM image of the core NW array at a period of 360 nm (scale bar is 200 nm), (b) BF-TEM of a NW from the 1000 nm period emphasizing the stacking faults (twins) in the crystal structure, and (c) accompanying selective area electron diffraction (SAD) pattern.

Finally, the full core-shell structure was grown according to the details outlined in Section 6.3. Scanning electron microscopy (SEM) images, such as that shown in Figure 6.1d, confirmed that the NWs were droplet-free with a flat top facet, smooth sidewall facets, negligible tapering, and a hexagonal cross-section. Figure 6.1b shows the EBL patterned oxide holes in SEM with a consistent diameter of 90 nm and a period written with a positioning accuracy of 0.6 nm and a field stitching accuracy of 20 nm. For periods of 1000, 1500, 2000 and 3000 nm,

NWs had average diameters of 440, 475, 505 and 520 nm and average lengths of 1180, 1190, 1280 and 1400 nm, respectively. We can find growth rates for the shell growth by considering the core dimensions of the 1000 nm period NWs (L = 1100 nm, D = 230 nm) and final core-shell NW dimensions of the 1000 nm period NWs (L = 1180 nm, D = 440 nm). Over the two-hour shell growth time, the axial growth rate was 0.7 nm/min while the radial growth rate was 1.8 nm/min.

Both diameter and length increased with period (Figure 6.1e), although an inverse relationship between diameter and length has been observed in other studies of InAsSb NWs [63,96,100,188]. Often this trend is attributed to declining In adatom competition, occurring when NW spacing is less than twice the In diffusion length [35]. However, the In diffusion length is believed to be ~750 nm for nominal InAs on Si growth conditions [35], and reduced under Sb flux in the MBE [5]. Since the smallest period of 1000 nm in our study is likely beyond this competitive growth regime, which is evidenced by the In/Sb droplets between the NWs, it cannot explain our diameter trend with period. Instead, vapor-solid growth can show a proportional relationship, as in our study, since it does not rely on the supersaturation of a catalyst particle for axial growth [101]. In this case, the diameter difference between the arrays can be attributed to an increased adatom re-emission flux from the oxide surface between neighboring NWs [8,41]. Saturation at 3000 nm period occurs as the maximum capture of the re-emission flux is approached. The saturation limits the ability to control the diameter with the period for larger diameter NWs. However, larger NW diameters can be

achieved by increasing the growth duration, which is beyond the scope of the present study. NWs within the 3000 nm period had a higher radial growth rate than those in the 1000 nm period. It follows that longer growth times will further spread the diameters among the arrays under the same growth conditions, while increasing the diameters of all arrays.

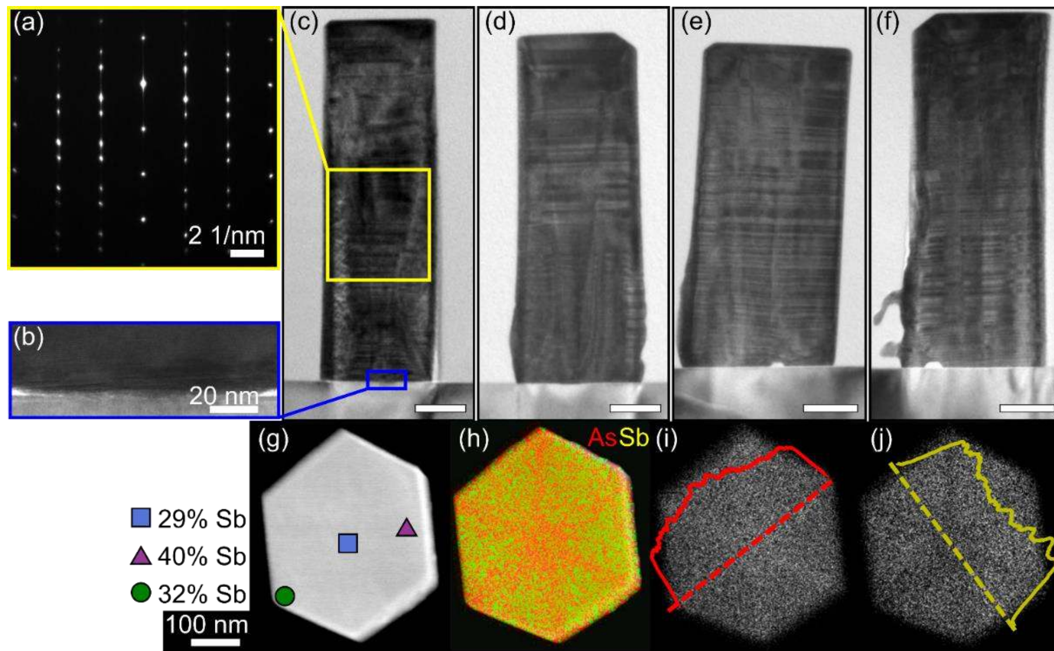

Figure 6.6: TEM analysis of NW arrays. (a) – (f) Vertical FIB-cut NWs from each of the 1000, 1500, 2000, and 3000 nm arrays with indicated selected area electron diffraction (SAD) pattern and high-resolution TEM of the substrate-NW interface. Scale bars indicate 200 nm. (g) – (j) HAADF-STEM from microtome horizontal cross-section of a NW from the 1000 nm array with point scans, EDX area map of As and Sb, line scan section of As area map, and line scan section of Sb area map, respectively.

Focused ion beam (FIB) vertical cross-sections along the NW length, and ultramicrotome horizontal cross-sections, were performed on each of the four NW arrays. The resulting FIB lamellas were approximately 100 nm thick, less than one

quarter of the smallest NW diameters, and cut through the center of a row of NWs. Figure 6.6c-f show the bright field TEM images for FIB-prepared NWs cut in the growth direction. SAD patterns (Figure 6.6a) revealed a twinned zincblende (ZB) crystal structure, as observed previously for similar NWs [95,178,189]. These twins, identified as contrast stripes in the TEM images, propagate across the whole NW diameter suggesting epitaxial growth of the shell on the core. A separate growth of the core without a shell found a similar twinned ZB crystal structure (Figure 6.5). High resolution TEM identified epitaxial contact between the NWs and the silicon substrate across the entire ~90 nm hole (Figure 6.6b).

Horizontal ultramicrotome cuts were also created to further investigate the composition of the core and shell. The high-angle annular dark field scanning TEM (HAADF-STEM) image of a NW from the 1000 nm period array is shown in Figure 6.6g. A separately grown core without a shell revealed that the core diameter was 200 nm for the 1000 nm period (Figure 6.5). Accompanying energy dispersive x-ray (EDX) area, line, and point measurements are indicated in Figure 6.6g-j. The EDX area maps reveal segregation of As and Sb atoms at the corners of each <110> side facet. The segregation forms a high As content along <112> directions extending from the core to the corners of the shell. Previous reports of segregation in ternary shells (GaAs-AlInP [190] and GaAs-AlGaAs [191,192]) found this was a result of differences in diffusion lengths at the corners of the shell. In the AlGaAs shells, Ga diffused away from the corners more readily than Al leading to higher Al concentrations along the <112> directions. Presumably, segregation

of As and Sb in our NWs is a result of a similar effect. Due to the growth temperatures used in our study, it is more likely that Sb more readily diffuses from the <112> facets, while As is governed by a desorption process [34]. The line scan for As content in Figure 6.6i shows a gradient decreasing radially out from the core along one of the As-rich ridges. Other reports [193] indicate a constant composition along the ridges and sharp heterojunctions at the core and shell interfaces. The radial gradient in our study may be a result of an Sb surfactant effect [181]. A line scan for Sb content through the Sb-rich shell is shown in Figure 6.6j. Point scans in Figure 6.6g quantify the Sb content of three major regions: core (29%), Sb-enriched shell (40%), and As-enriched corners (32%). All four NW arrays were compositionally consistent, within 2%, for each of the point scans.

Further FIB analysis was performed on the NW array in Figure 6.2c (FF = 14%). High resolution TEM images are shown in Figure 6.7 with highlighted stacking faults (SF) and twin planes (TP). The density of planar defects (SF+TP) was 223 μm^{-1}, which is similar to other reports of InAsSb NWs at this composition [63]. Figure 6.7b also shows a SAD that is dominated by twin planes. Specifically, the stacking fault density was 77 μm^{-1} and the twin plane density was 146 μm^{-1}. Our previous fault density for InAs NWs was 350 μm^{-1}, where all the interfaces were stacking faults because the NWs were mostly WZ. Thus, Sb has changed the crystal structure of the NW from predominantly WZ to ZB, as several other groups have reported previously [63,97,189,194,195]. Most of the InAsSb NW is ZB, but near

the nucleation site there are a few ordered segments of WZ. Likely these are due to the InAs stem that we use to nucleate a high yield of NWs.

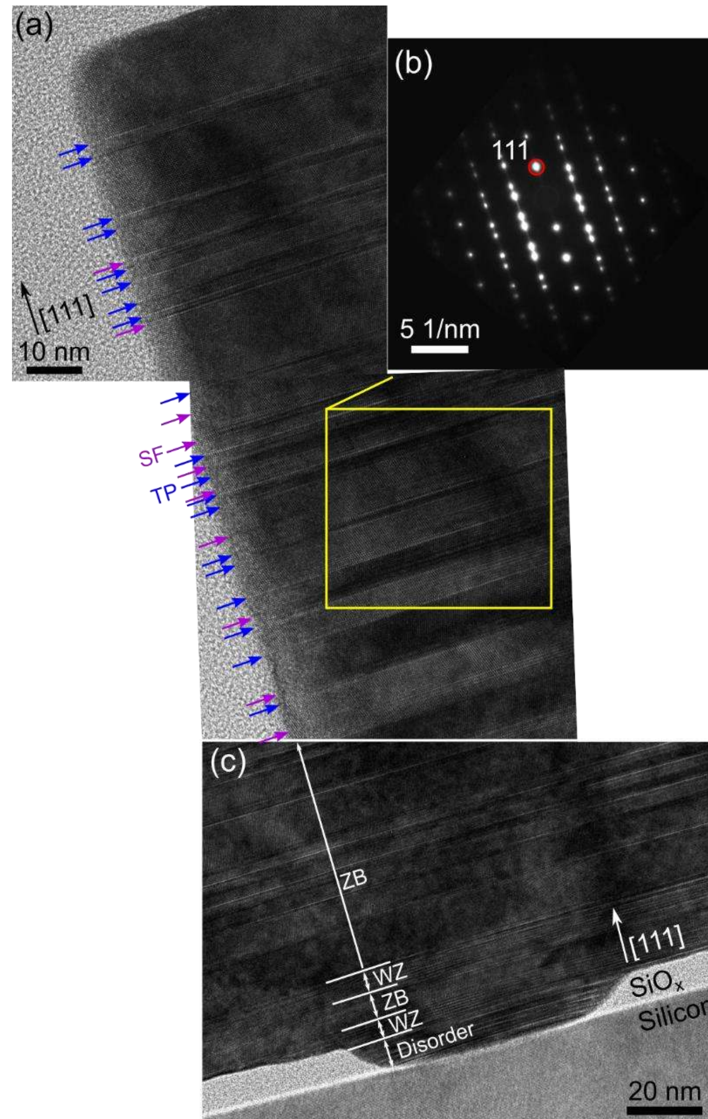

Figure 6.7: High resolution TEM images of an InAsSb NW (FF = 14%). (a) along the top 150 nm of the NW, (b) SAD of the indicated region, and (c) higher magnification at the base of the NW. Twin planes (TP) and stacking faults (SF) are identified in (a) by blue and purple arrows respectively. Ordered regions are shown in (c).

6.4.3 Absorptance

FTIR measurements were used to obtain the diameter-dependent infrared absorptance from each of our four core-shell NW arrays. A background absorptance measurement was performed on a clean Si substrate without any oxide mask or III-V growth. The resulting absorptance from the Si (grey curves in Figure 6.8) was negligible, as expected for low doped silicon in the infrared region. Another background measurement was taken for an area just outside each of the four arrays (dash-dotted lines in Figure 6.8), which included some droplets and crystallites on the oxide but did not include any NWs (Figure 6.1c). This measurement was included as a reference for the NW absorptance. It represents the absorptance of several droplets and crystallites on the substrate surface near the NW array but does not quantitatively match the droplet or crystallite density inside the array and cannot be used to normalize the experimental NW data. However, the background measurement confirms that the peak in the NW absorptance spectra are indeed due to the NW array, and the background absorptance surrounding the peaks is due to the crystallites and droplets on the oxide between the NWs. Experimental NW absorptance peaks in Figure 6.8 red-shift with NW diameter with peaks appearing at approximately 2100, 2400, 2500 and 2700 nm for the period of 1000, 1500, 2000 and 3000 nm, respectively.

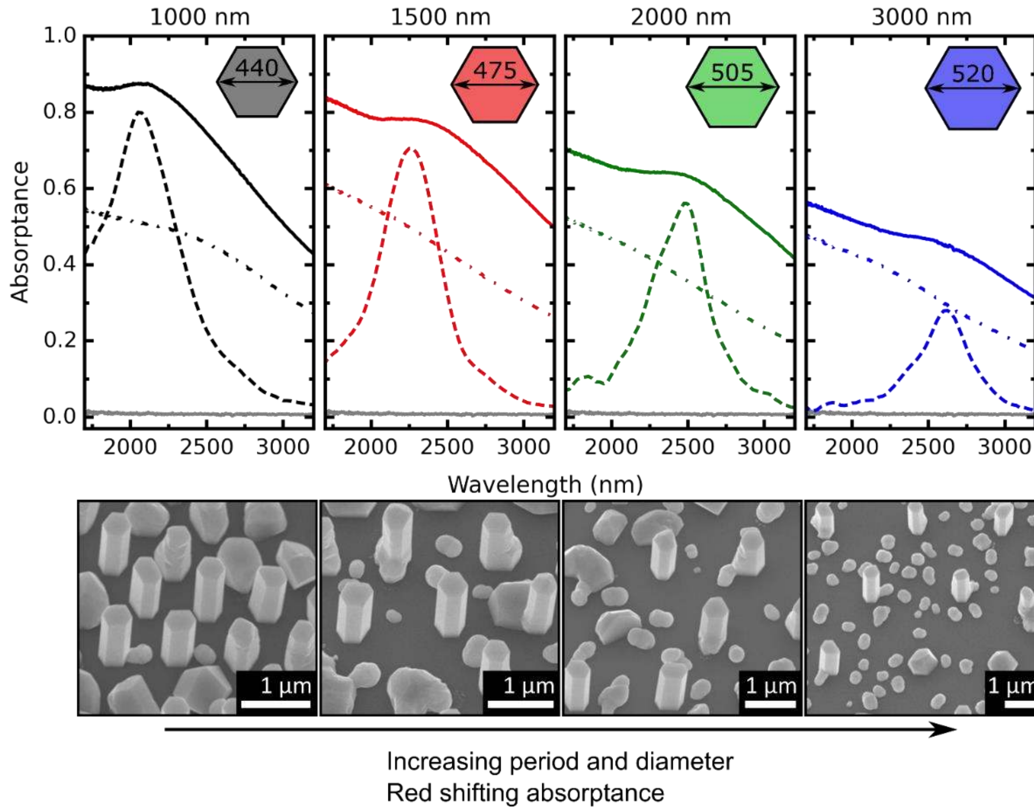

Figure 6.8: Absorptance spectra of InAsSb NW arrays for the indicated periods (black: 1000 nm, red: 1500 nm, green: 2000 nm, blue: 3000 nm). Solid lines are experimental data, dashed lines are simulated results, and dash-dot lines are experimentally measured background absorptance near the NW arrays, which includes the effect of droplets, crystallites, and the silicon substrate. Experimentally measured silicon substrate absorptance (grey curve in each plot) shows negligible absorptance. Insets are hexagonal NW cross-sections with indicated diameters in nm. Corresponding tilted SEM images are shown below each absorptance curve.

Optical simulations in COMSOL Multiphysics were performed to further investigate the characteristics of the experimental absorptance peaks and their dependence on NW diameter. Simulations used the same average geometric parameters as the experimental NW arrays while excluding the stacking faults and the composition segregation in the shell. They revealed absorptance peaks in the

SWIR (dashed lines in Figure 6.8), closely matched in magnitude and wavelength to the experimentally observed peaks. Furthermore, E- and H- field component profiles (Figure 6.9) for the 1000 nm period and 440 nm diameter array at λ=2050 nm incident wavelength identified that the peak absorptance is due to the HE_{11} guided mode resonance [45,46,80]. Previous reports [45,46,74,80] found that the dominant effect on HE_{11} peak position is the NW diameter. Additionally, period and length were shown to have a negligible effect on peak position, although NW length increases the magnitude of the absorptance. Changes in NW composition are also not expected to affect the peak position [45,46,80]. For example, simulations have shown that the red-shift of the HE_{11} absorptance peak wavelength with unit change in NW diameter (nm of red-shift per nm increase in diameter) is similar for different materials (GaAs, InP, InAs, InSb) and is not strongly dependent on composition or period [45,46,80]. Furthermore, compositional changes between NW arrays are small (<2%) and cannot account for changes in the absorptance peaks [99]. Instead, the red-shift in absorptance peaks is primarily due to an increasing NW diameter, associated with the HE_{11} guided mode resonance.

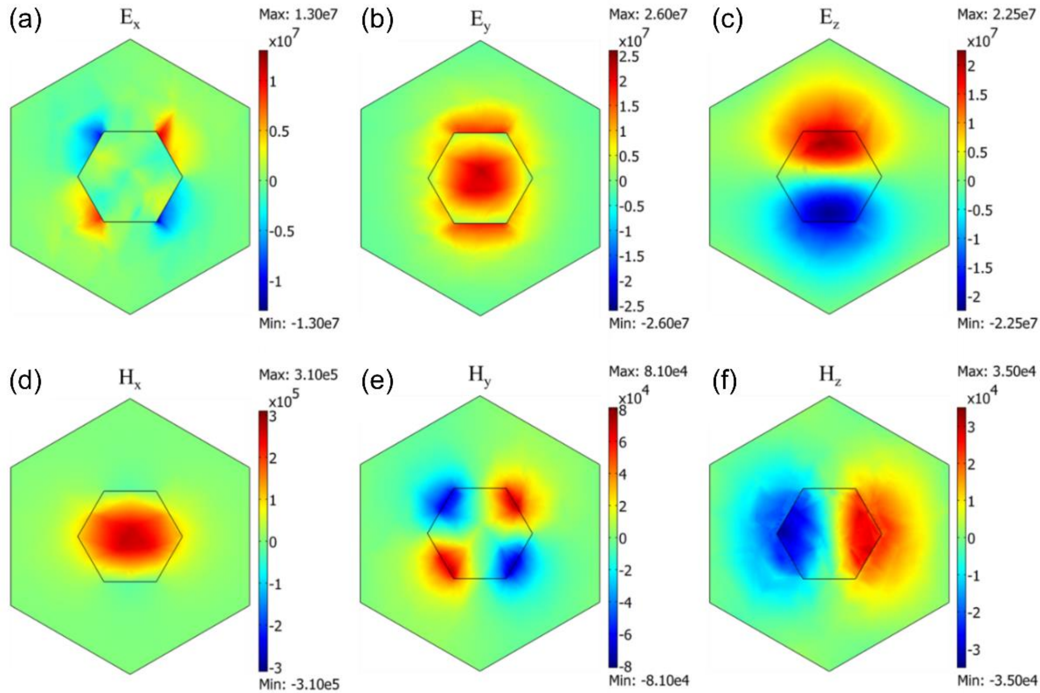

Figure 6.9: (a) E_x, (b) E_y, (c) E_z, (d) H_x, (e) H_y, and (f) H_z field components in simulated semi-infinite InAsSb NW array at a wavelength of 2050 nm for period of 1000 nm and diameter of 440 nm. The E- and H-field patterns correspond to that of the HE_{11} mode. The E- and H-field component magnitudes are in units of V/m and A/m.

The absorptance magnitude for both simulated and experimental peaks decline with increasing period due to a decreasing fill factor (or diameter/period ratio) of the NW array. The NW arrays have an optimal fill factor at which maximum absorptance is achieved [46]. For sparse NW arrays, when NW diameter is less than 1/3 of the period ($D/P < 1/3$), a large fraction of the incident light passes through the array to the substrate instead of being absorbed in the NWs. Absorptance increases to a maximum between $1/3 < D/P < 1/2$ and then begins to decrease as the reflectance from the top of the NWs approaches thin film conditions ($D/P > 1/2$) and the near-field coupling between NWs increases [196].

Fill factors for our 1000, 1500, 2000, and 3000 nm period arrays are D/P = 0.44, 0.32, 0.25 and 0.17, respectively. Optimal fill factor conditions are met with the 1000 nm array while the larger period arrays move into the sparse regime and a corresponding magnitude decrease for the absorptance peak is observed. Thus, increasing the NW diameter via increasing period is not viable indefinitely without a significant loss in absorptance. However, future growths may simultaneously employ other techniques, such as longer growth duration, to increase NW diameter and help maintain an optimal fill factor.

The distribution in the diameter of the fabricated NWs, which was in the range of ±16 to 36 nm, leads to a range of spectrally unresolved HE_{11} resonance peaks, closely spaced in wavelength, which broadens the FWHM of the HE_{11} peak. FWHM of the simulated HE_{11} peaks were found to be 640, 470, 430, 400 nm for the 1000, 1500, 2000, 3000 nm periods respectively. The red-shift of the HE_{11} absorptance peak wavelength (in nm) per unit change in NW diameter (in nm) can be extracted from simulations [45,46,80,99,197]. For example, in Ref. [46] the red-shift for the 1000 nm period array near a NW diameter of 440 nm (P=1000 nm, D=440 nm) is 4.13 nm/nm. The measured NW diameter for this NW array varied by ±20 nm. Hence, the contribution of the NW diameter variation to the broadening of the absorptance peak can be estimated as 2*20 nm*4.14 nm/nm = 165 nm.

6.4.4 Current-Voltage

IV analysis was performed on the $InAs_{0.77}Sb_{0.23}$ core shown in Figure 6.5. Average diameters for the arrays were from 160 nm to 190 nm and average lengths were from 440 nm to 540 nm. Diameters and lengths increased with dose label and period, meaning D1 500 nm were the smallest NWs (diameter and length), while D5 3000 nm were the largest. Device fabrication followed the steps in Section 3.3 of this thesis, where the NWs were planarized with BCB and the transparent conductor was 250 nm of ITO, instead of the recently defined thin nickel layer. Opaque contacts were e-beam deposited Ni/Ge/Au 25/50/225 nm. IV response was taken in a four-point configuration in the dark, and under solar illumination at one sun. No response was measured for IR illuminated samples, likely due to the optically thick ITO layer. As a result, no multispectral IR analysis could be performed. This is left as a topic for future study.

Figure 6.10 shows the IV semilog plots for all 25 NW arrays on the sample. Period and diameter labels are indicated for the rows and columns. Current density was calculated using the total cross-sectional area of the NWs in an array (considering the yield); i.e., $\text{current density} = \frac{\text{current}}{\text{n x A(D)}}$ where n is the number of NWs in the pad, and A(D) is the hexagonal cross-sectional area of NWs in the array as a function of average diameter. This calculation is used instead of the conventional definition (considering the whole device area) since it allows for a more direct comparison between the arrays, especially when yield varies device to device. Upon measuring the arrays, two distinct responses were unveiled. In

some pads, marked by a blue square, the V_{oc} shift due to solar illumination was negligible and the IV curves were linear. These pads are presumed to be shorted, likely through the BCB isolation layer. Other pads, marked by a red square, show some response under solar illumination.

From the plots in Figure 6.10, all red-square arrays have the same magnitude current density around 10 mA/cm^2 at a bias of -0.1 V. This is only one order of magnitude larger than an axial p-i-n InAsSb NW structure by Thompson et al [100]. Average open circuit voltage (V_{oc}) for these arrays was 14 mV, which is much lower than the room temperature bandgap of the InAsSb NW (about 200 meV). Thus, there is likely recombination at the heterojunction interface of the device, reducing the V_{oc} [23,198].

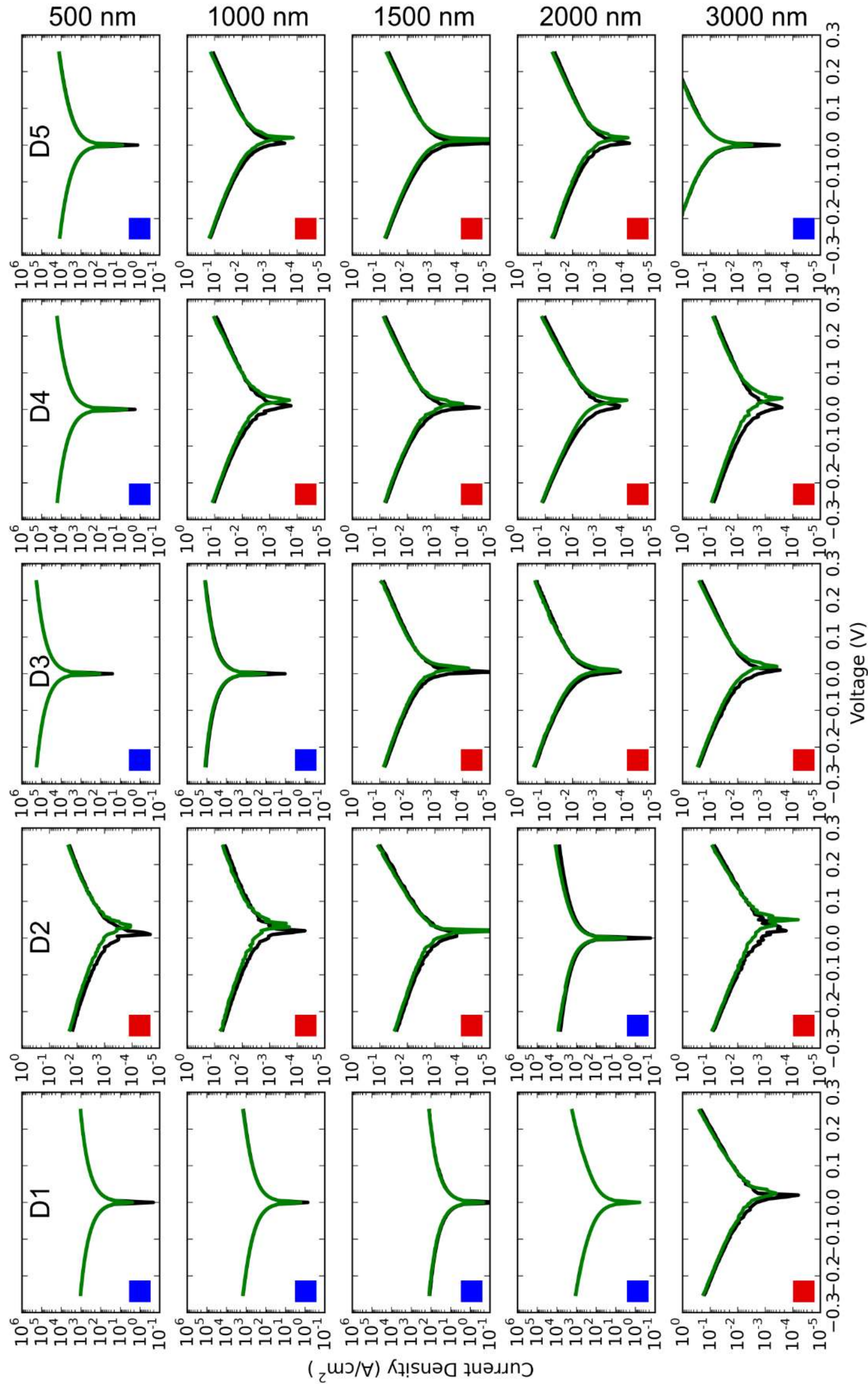

Figure 6.10: Solar photoresponse (green) of each NW pad relative to dark (black). Dose labels for the arrays are giving by D1, D2, D3, D4, and D5. The period is indicated at the top. Blue squares signify a shorted device and red squares signify a responsive device.

Two collaborative projects have also worked to explore the photoresponse of our NWs. The first project is with the Jonathan Baugh Group at the University of Waterloo. It attempts to measure photoresponses of IR-sensitive single InAs NWs. Single NW and array devices were fabricated following the steps outlined in Chapter 3 of this thesis. NWs were grown on p-Si(111) ($N_A > 2 \times 10^{19}$ cm^{-3}) with a unique EBL pattern. This pattern defined a few regions of arrayed NWs, and other regions of single NWs that were spatially isolated. Once planarized, NW arrays and single NWs could be contacted individually with photolithographically defined transparent contacts (sputtered ITO, 140 nm) and opaque contacts (e-beam deposited Ti/Au, 30/70 nm). Samples were illuminated with a Thorlabs SLS203L globar source through a monochromator.

Currently, two InAs NW arrays have been measured, with single NW measurements ongoing. The first array had 1000 nm period on a 35 µm x 35 µm pad, which produced NWs with an average hexagonal diameter of 120 nm and an average length of 1.2 µm. The second array had 360 nm period on a 20 µm x 20 µm pad, which produced NWs with an average hexagonal diameter of 90 nm and an average length of 1 µm. Figure 6.11a shows the IV measurements for several wavelengths on the first array. The V_{oc} shifts according to the illuminating wavelength since the light-generated current in the NWs is dependent on wavelength. The V_{oc} shifts in Figure 6.11b have been normalized to the power of the source and plotted against wavelength. Both 120 nm diameter and 90 nm diameter responses are shown. From this plot we can see there is a slight red-shift

with increasing diameter (at wavelengths from 450 to 470 nm), which is the first evidence of the multispectral effect from electrical measurements. From K. M. Azizur-Rahman and R. R. LaPierre [45], the peak absorptance wavelengths of a 90 nm and 120 nm hexagonal diameter (82 nm and 110 nm circular diameter) InAs array should be approximately 500 nm and 550 nm. More investigation is necessary to identify the cause of this divergence.

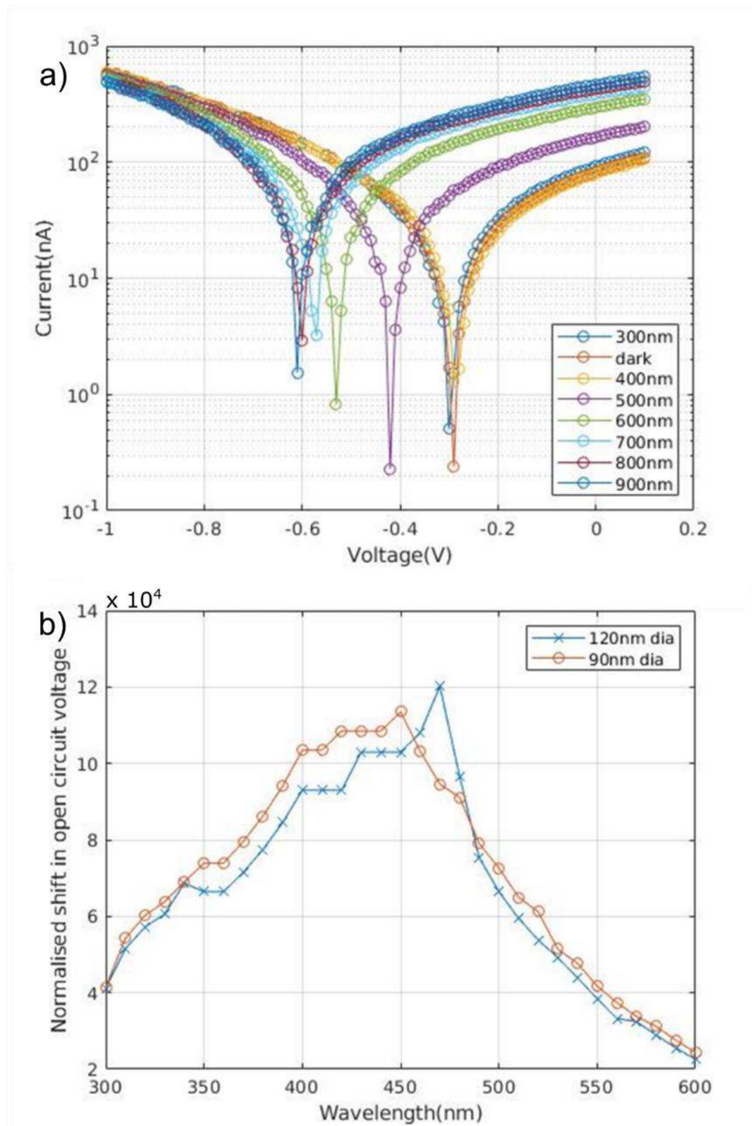

Figure 6.11: Photoresponse of InAs NW arrays. a) IV measurements for a NW with average diameter of 120 nm, illuminated with the indicated wavelength. b) V_{oc} shift vs wavelength for 90 nm and 120 nm diameter NW arrays. Plots courtesy of Baugh Group.

The second project is with the Simon Watkins Group at Simon Fraser University. It attempts to measure single NW photoresponses using nanoprobe contacting in an SEM [199,200]. Single NWs were contacted in an SEM with a tungsten nanoprobe without planarization (Figure 6.12a). The purpose of this

project was to look at the effect of BCB on the photoresponse of single NWs and to measure diameter-dependent photocurrent under IR illumination. Simulations indicate there should be an absorptance decrease due to reduced radial mode confinement in the NWs when encapsulated by BCB compared to air [46]. These NWs were $InAs_{0.77}Sb_{0.23}$ grown on p-Si(111) ($N_A > 2 \times 10^{19}$ cm^{-3}), as described previously.

Thus far, dark current measurements have been performed on several NWs with various diameters (Figure 6.12b). Most NWs show similar rectification across the -1 V to 1 V range, although some are ohmic, likely due to poor contact between the nanoprobe and the NW. The four largest diameter NWs were from an array with 95 nm oxide holes, while the remaining NWs were from an array with 55 nm oxide holes. The four large diameter NWs saturate at a reverse bias current about 3x larger than the smaller diameter NWs. Since the area of a 95 nm diameter hole is about 3x larger than a 55 nm hole we have likely observed the proportional relationship between I_s and cross-sectional area of a diode junction. Next, as an ongoing project, broadband IR light will be fibre-coupled into the SEM for IV measurements, followed later by monochromatic illumination.

Calculating the current density in the same way as Figure 6.10 gives 7 A/cm^2 for a 145 nm diameter NW at ± 0.3 V bias. This is within an order of magnitude of the dark IV measurements for the InAsSb arrays in Figure 6.10. As expected, there is no significant difference between these dark curves and the previous ones (Figure 6.10) due to the BCB planarization layer.

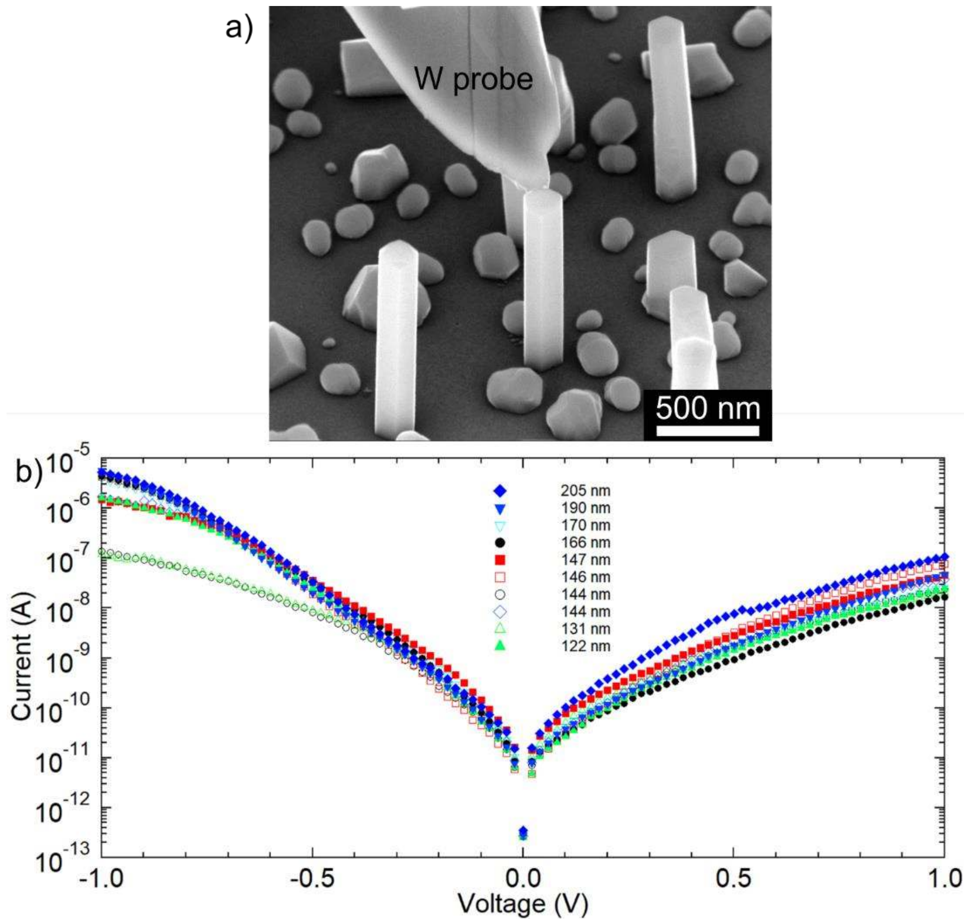

Figure 6.12: Single InAsSb NW contacting in SEM. a) 52° tilted SEM (view of a single NW contacted by a tungsten nanoprobe. b) IV measurements of NWs with indicated diameters. Image courtesy of Watkins Group.

6.5 Conclusions

In summary, patterned arrays of large diameter (440 – 520 nm) InAsSb NWs were grown on Si, demonstrating the potential for future integration with Si ROICs. Four distinct absorptance peaks were produced in the SWIR region by fabricating arrays of different diameters in a single epitaxial growth controlled by the array period. Some electrical characterization also demonstrated the multispectral effect. In future work, we will be able to create absorptance peaks

at longer wavelengths (e.g., in the MWIR region) by changing growth conditions, increasing growth time, and increasing hole diameters.

7 Conclusions and Future Work

7.1 Thesis Summary

The ultimate goal of antimonide-based multispectral IR photodetection began with GS-MBE growths of InAs NWs on Si(111). Several growth modes and growth conditions were explored to create high-yield NW arrays:

I. Au-assisted VLS and positioned Au-assisted-VLS had low yield for all V/III ratios and temperatures in the study, which was attributed to material competition with thin film.

II. Catalyst-free VS NWs increased in length and diameter with temperature as the thin film coverage decreased. V/III ratio had little effect on the NWs indicating that they grew in As-rich conditions.

III. Au-assisted VLS-SAE mode reduced the parasitic film growth between the NWs and allowed for up to 10% vertical yield at 440 °C. A secondary desorption flux of As was responsible for NW elongation at larger periods. This was verified in the V/III ratio study in which axial growth rate increased with increasing As flux, thereby demonstrating that the growths were in an As-limited regime.

IV. A high yield (72%) of SAE NWs was found at 440 °C and a V/III ratio of 4. SAE NWs were also found to be As-limited with axial growth rates of 10 and 22 nm/min for V/III ratios of 4 and 10, respectively.

A model was created to describe the optimal yield window in our SAE InAs NWs with the following conclusions:

I. Non-vertical crystallites were formed when the number of group V atoms arriving to the oxide holes exceeded the number of group III atoms, since a nucleating droplet could not be produced in these conditions.
II. Droplets were formed when the group III flux to the oxide hole was higher than the group V flux. No NWs grew when the size of the droplet exceeded the size of the oxide hole.
III. The highest yield was found when droplets were formed and remained smaller than the hole. After nucleation the droplet is consumed due to a decreased supply of indium.
IV. The optimal yield conditions were further delineated by considering shadowing effects from neighbouring NWs on the arrival rates of growth species.

From these findings it was possible to begin fabricating antimonide-based NWs using InAs NWs as a high-yield stem. Recent absorptance simulations indicated that multispectral IR absorptance could be achieved with large diameter NWs. The following primary results were found in pursuit of large-diameter antimonide NWs for multispectral IR photodetection:

I. In a study of fractional flux in InAsSb NWs, increasing Sb was found to reduce the axial growth rate and increase the radial growth rate. Through

EDX in TEM the Sb content, x, in $InAs_{1-x}Sb_x$ was 0.23 for a FF of 5% and 0.33 for a FF of 14%. Raman analysis was used to extract the remaining compositions, which were 0.32 for a FF of 10%, and 0.39 for a FF of 23%.

II. Using an InAs stem and the InAsSb FF results, a large diameter core-shell structure was grown on silicon. The core, initialized with an InAs stem and grown at a FF of 5%, was used to achieve >1 µm lengths. The shell, grown at a FF of 14%, was used to enlarge the diameters of the NWs to absorb in the SWIR region. Diameters also had a period dependence, allowing for arrays with different diameters to be created in a single growth.

III. Four absorptance peaks (2100, 2400, 2500, 2700) were measured in FTIR that corresponded to the four different diameters (440, 475, 505, 520 nm). Absorptance simulations agreed with the experimental peak positions and verified that absorptance was occurring through the HE_{11} waveguiding mode.

IV. In a project with the University of Waterloo, InAs arrays with different diameters had photocurrent peaks that shifted with average NW diameter. This was the first evidence of the multispectral effect from electrical measurements.

7.2 Future Work

Although the InAs study provided a reproducible high yield greater than 50%, high absorptance arrays with a small peak FWHM and minimal background absorptance require higher NW yield and better uniformity. This may be achieved by a combination of RIE, wet etching, cleaning, In pre-deposition, or high temperature annealing steps [31,32,43,44]. Nearly 100% yield of InAs on Si is achievable in either MOCVD [146] or MBE [35]. A high yield should also improve the morphological uniformity of the NW arrays by minimizing local material flux variations.

With improved uniformity comes sharper photoresponse peaks. The next step would be to measure the IR multispectral photoresponses of several InAsSb arrays grown in a single growth, such as in Chapter 6. Although some measurements have been demonstrated for InAs NWs in Section 6.4.4 as a proof of concept, large diameter InAsSb NWs with IR absorptances have not yet been measured. A small illumination setup has already been built for this purpose. The setup uses an SLS203L globar source from Thorlabs and a series of narrow bandpass filters with center wavelengths aligned to the absorptance peaks from Chapter 6.

Our initial IV measurements indicated that there is recombination in the device at the heterojunction interface. Thompson et al [100] have also achieved a lower reverse saturation current using an axial p-i-n junction in InAsSb NWs. To

improve our device performance, we would likely need to explore improved doping in the radial direction. Typically, Be is used as a p-type dopant in III-V semiconductors, and Te is used as an n-type dopant [201]. Further improvements could be made by passivating the NWs with a larger bandgap semiconductor, such as $Al_xIn_{1-x}Sb$, to reduce the surface recombination velocity [202].

Chapter 6 described NWs with absorptances in the SWIR region. To access the MWIR region and expand the usefulness of these multispectral detectors, larger diameter NWs need to be grown. This can be accomplished by increasing the growth time or incorporating a higher FF shell to increase the radial growth rate. Higher Sb content in the NWs may also improve the electrical properties by reducing stacking faults. The maximum absorptance wavelength due to the bandgap of core (23% Sb) and shell (33% Sb) are 6.2 µm and 8.3 µm, respectively. Thus, the entire MWIR region can be absorbed in the shell and most of it can be absorbed in the core. The bandgap would need to be decreased to absorb in the LWIR region. This is possible by increasing the Sb content in the NWs to a maximum of 63% where the bandgap reaches a minimum of 84 meV (14.7 µm). Of course, this would require very large diameter NWs to exploit the HE_{11} resonances (1.5 - 3 µm for the LWIR range).

All NWs in this thesis were fabricated by bottom-up growth, but it is also possible to top-down etch NWs from a thin film. It is much easier to achieve large diameter NWs (“microwires”) using the top-down method since the diameter is directly defined by a lithographic mask. A short project is presented here as a

future work for reaching the very large diameters required in LWIR detection and as an alternative for SWIR and MWIR NWs. This project explored a few etch recipes for an InSb (100) wafer to check roughness and undercutting. NW positions were masked by 120 nm thick EBL patterned titanium disks. The EBL pattern consisted of several 300 µm x 300 µm pads of circular disks with diameters from 300 nm to 1500 nm and square periods from 1000 nm to 4000 nm. Diameters and periods were chosen to mimic the dimensions of simulations performed by K. M. Azizur-Rahman and R. R. LaPierre to later compare absorptance [46]. Etching was completed on an Oxford ICP380 system at the University of Waterloo Quantum NanoFab Facility by a summer student, Daniel Parent, under my supervision.

Zhang et al [203] explored ICP-RIE etching of InSb (111) using CH_4, H_2, and Ar. They varied RF bias power, gas ratios, and system pressure to find high etch rates with low undercutting and low roughness. A balance between etch rate and roughness was found with 600 W ICP Power, 150 W RF Power, and $CH_4/H_2/Ar$ flow rates of 15/50/5 SCCM. Their mesa structures also had sidewall angles of 80° for pressures of 1.0 – 2.0 Pa. There was noticeable undercutting at 4.0 Pa. Etching parameters for our NWs were selected based on the above results and are shown in Table 7.1.

Table 7.1: Recipes for ICP-RIE etching InSb (100) NWs

Parameter	Recipe 1	Recipe 2
ICP Power (W)	600	600
RF Power (W)	150	150
Pressure (Pa)	2.0	1.0
$CH_4/H_2/Ar$ (SCCM)	15/50/5	15/50/5

Recipe 1 produced the NWs shown in Figure 7.1a with visible undercutting and minimal roughness. They had lengths of 1600 nm, top diameters of 660 nm, and middle diameters of 560 nm indicating a 50 nm undercut. In recipe 2 the pressure was decreased by half in order to decrease the undercutting. Figure 7.1b shows NWs etched with recipe 2 where the undercutting was decreased but roughness was visibly increased. They had lengths of 1400 nm, top diameters of 630 nm, and middle diameters of 580 nm indicating a 25 nm undercut. Therefore, recipe 1 provides a faster etch with less roughness, but the higher pressure also leads to less anisotropic etching and more undercutting.

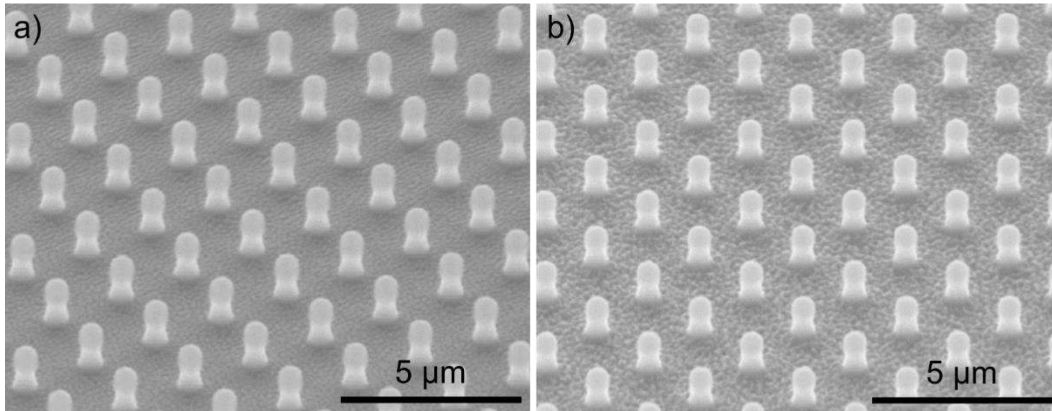

Figure 7.1: RIE etched InSb (100) wafers with 600 nm diameters and 2000 nm period using a) recipe 1 and b) recipe 2.

Next steps for this project would have included titanium disk removal by hydrofluoric acid, absorptance characterization in FTIR, and then repeating the process with InSb film grown on Si (100) using an AlSb buffer layer to reduce defect formation [89,204,205]. However, the project has been adopted as a full Masters

thesis by another student due to its initial success. This is likely the optimal method for achieving very large diameter NWs for LWIR detection.

8 References

[1] Wagner R S, Ellis W C, Jackson K A and Arnold S M 1964 Study of the filamentary growth of silicon crystals from the vapor J. Appl. Phys. **35** 2993–3000

[2] Hasegawa H, Fujikura H and Okada H 1999 Molecular-Beam Epitaxy and Device Applications of III-V Semiconductor Nanowires MRS Bull. **24** 25–30

[3] Patsha A, Pandian R, Dhara S and Tyagi A K 2015 Nonpolar p -GaN/ n -Si heterojunction diode characteristics: a comparison between ensemble and single nanowire devices J. Phys. D. Appl. Phys. **48** 395102

[4] Vogel A T, Boor J de, Becker M, Wittemann J V., Mensah S L, Werner P and Schmidt V 2011 Ag-assisted CBE growth of ordered InSb nanowire arrays Nanotechnology **22** 015605

[5] Guimard D, Nishioka M, Tsukamoto S and Arakawa Y 2007 Effect of antimony on the density of InAs/Sb:GaAs(100) quantum dots grown by metalorganic chemical-vapor deposition J. Cryst. Growth **298** 548–52

[6] Schmidt V, Wittemann J V., Senz S and Goesele U 2009 Silicon Nanowires: A Review on Aspects of their Growth and their Electrical Properties. Adv Mater **21** 2681–702

[7] Park H D and Prokes S M 2007 Study of the initial nucleation and growth of catalyst-free InAs and Ge nanowires Appl. Phys. Lett. **90** 203104

[8] Ramdani M R, Harmand J C, Glas F, Patriarche G and Travers L 2013 Arsenic pathways in self-catalyzed growth of GaAs nanowires Cryst. Growth Des. **13** 91–6

[9] Gomes U P, Ercolani D, Zannier V, David J, Gemmi M, Beltram F and Sorba L 2016 Nucleation and growth mechanism of self-catalyzed InAs nanowires on silicon Nanotechnology **27** 255601

[10] Boulanger J P and LaPierre R R 2012 Patterned gold-assisted growth of GaP nanowires on Si Semicond. Sci. Technol. **27** 035002

[11] Tornberg M, Mårtensson E K and Zamani R R Demonstration of Sn-seeded GaSb homo- and GaAs – GaSb heterostructural nanowires Nanotechnology **27** 0

[12] Yee R J, Gibson S J, Dubrovskii V G and LaPierre R R 2012 Effects of Be doping on InP nanowire growth mechanisms Appl. Phys. Lett. **101** 263106

[13] Lugani L, Ercolani D, Rossi F, Salviati G, Beltram F and Sorba L 2010 Faceting of InAs−InSb Heterostructured Nanowires Cryst. Growth Des. **10** 4038–42

[14] Kroemer H 2004 The 6.1A family (InAs, GaSb, AlSb) and its heterostructures: a selective review Phys. E Low-dimensional Syst. Nanostructures **20** 196–203

[15] Wagner J B, Sköld N, Reine Wallenberg L and Samuelson L 2010 Growth and segregation of GaAs-AlxIn1-xP core-shell nanowires J. Cryst. Growth **312** 1755–60

[16] Hobbs R G, Petkov N and Holmes J D 2012 Semiconductor nanowire fabrication by bottom-up and top-down paradigms Chem. Mater. **24** 1975–91

[17] Pettersson H, Tragårdh J, Persson A I, Landln L, Hessman D and Samuelson L 2006 Infrared photodetectors in heterostructure nanowires Nano Lett. **6** 229–32

[18] Boulanger J P, Chia A C E, Wood B, Yazdi S, Kasama T, Aagesen M and LaPierre R R 2016 Characterization of a Ga-Assisted GaAs Nanowire Array Solar Cell on Si Substrate IEEE J. Photovoltaics **6** 661–7

[19] Rehnstedt C, Mårtensson T, Thelander C, Samuelson L and Wernersson L E 2008 Vertical InAs nanowire wrap gate transistors on Si substrates IEEE Trans. Electron Devices **55** 3037–41

[20] Yan R, Gargas D and Yang P 2009 Nanowire photonics Nat. Photonics **3** 569–76

[21] Dey A W, Svensson J, Ek M, Lind E, Thelander C and Wernersson L-E 2013 Combining Axial and Radial Nanowire Heterostructures: Radial Esaki Diodes and Tunnel Field-Effect Transistors Nano Lett. **13** 5919–24

[22] Lee D S, Wang H, Hsu A, Azize M, Laboutin O, Cao Y, Johnson J W, Beam E, Ketterson A, Schuette M L, Saunier P and Palacios T 2013 Nanowire channel InAlN/GaN HEMTs with high linearity of gm and fT IEEE Electron Device Lett. **34** 969–71

[23] Holm J V 2013 Nanowire Growth for Photovoltaics (University of Copenhagen)

[24] Dolbak A E, Zhachuk R a. and Olshanetsky B Z 2004 Surface diffusion of Pb on clean Si surfaces Cent. Eur. J. Phys. **2** 254–65

[25] Dolbak A E and Olshanetsky B Z 2010 Diffusion of tin over clean silicon surfaces Phys. Solid State **52** 1293–7

[26] Yamaguchi K, Yujobo K and Kaizu T 2000 Stranski-Krastanov Growth of InAs Quantum Dots with Narrow Size Distribution Jpn. J. Appl. Phys. **39** 1245–8

[27] Harmand J-C, Glas F and Patriarche G 2010 Growth kinetics of a single

InP_{1−x}As_{x} nanowire Phys. Rev. B **81** 235436

[28] Dimakis E, Lähnemann J, Jahn U, Breuer S, Hilse M, Geelhaar L and Riechert H 2011 Self-assisted nucleation and vapor-solid growth of InAs nanowires on bare Si(111) Cryst. Growth Des. **11** 4001–8

[29] Gomes U P, Ercolani D, Zannier V, Battiato S, Ubyivovk E, Mikhailovskii V, Murata Y, Heun S, Beltram F and Sorba L 2017 Heterogeneous nucleation of catalyst-free InAs nanowires on silicon Nanotechnology **28** 065603

[30] Li S, Xiang Q, Wang D and Wang K L 1996 Investigation of facet formation and competition in MBE growth J. Cryst. Growth **164** 235–40

[31] Jing Y, Bao X, Wei W, Li C, Sun K, Aplin D P R, Ding Y, Wang Z-L L, Bando Y and Wang D 2014 Catalyst-free heteroepitaxial MOCVD growth of InAs nanowires on si substrates J. Phys. Chem. C **118** 1696–705

[32] Russo-Averchi E, Tütüncüoglu G, Dalmau-Mallorqui a., Canales Mundet I, de la Mata M, Rüffer D, Arbiol J, Conesa-Boj S and Fontcuberta i Morral a. 2015 Bottom-up engineering of InAs at the nanoscale: From V-shaped nanomembranes to nanowires J. Cryst. Growth **420** 47–56

[33] Tomioka K, Motohisa J, Hara S and Fukui T 2008 Control of InAs nanowire growth directions on Si. Nano Lett. **8** 3475–80

[34] Tomioka K, Mohan P, Noborisaka J, Hara S, Motohisa J and Fukui T 2007 Growth of highly uniform InAs nanowire arrays by selective-area MOVPE J. Cryst. Growth **298** 644–7

[35] Hertenberger S, Rudolph D, Bichler M, Finley J J, Abstreiter G, Koblmüller G and Koblm?ller G 2010 Growth kinetics in position-controlled and catalyst-free InAs nanowire arrays on Si(111) grown by selective area molecular beam epitaxy J. Appl. Phys. **108** 114316

[36] Mandl B, Stangl J, Mårtensson T, Mikkelsen A, Eriksson J, Karlsson L S, Bauer G, Samuelson L and Seifert W 2006 Au-free epitaxial growth of InAs nanowires Nano Lett. **6** 1817–21

[37] Jeon N, Ruhstorfer D, Döblinger M, Matich S, Loitsch B, Koblmüller G and Lauhon L 2018 Connecting Composition-Driven Faceting with Facet-Driven Composition Modulation in GaAs–AlGaAs Core–Shell Nanowires Nano Lett. **18** 5179–85

[38] Royo M, De Luca M, Rurali R and Zardo I 2017 A review on III–V core–multishell nanowires: growth, properties, and applications J. Phys. D. Appl. Phys. **50** 143001

[39] Xu T, Dick K a, Plissard S, Nguyen T H, Makoudi Y, Berthe M, Nys J-P, Wallart X, Grandidier B and Caroff P 2012 Faceting, composition and

crystal phase evolution in III–V antimonide nanowire heterostructures revealed by combining microscopy techniques Nanotechnology **23** 095702

[40] Tomioka K, Ikejiri K, Tanaka T, Motohisa J, Hara S, Hiruma K and Fukui T 2011 Selective-area growth of III-V nanowires and their applications J. Mater. Res. **26** 2127–41

[41] Gibson S J and LaPierre R R 2014 Model of patterned self-assisted nanowire growth Nanotechnology **25** 415304

[42] Küpers H, Tahraoui A, Lewis R B, Rauwerdink S, Matalla M, Krüger O, Bastiman F, Riechert H and Geelhaar L 2017 Surface preparation and patterning by nano imprint lithography for the selective area growth of GaAs nanowires on Si(111) Semicond. Sci. Technol. **32** 115003

[43] Plissard S, Larrieu G, Wallart X and Caroff P 2011 High yield of self-catalyzed GaAs nanowire arrays grown on silicon via gallium droplet positioning. Nanotechnology **22** 275602

[44] Madsen M H, Aagesen M, Krogstrup P, Sørensen C and Nygård J 2011 Influence of the oxide layer for growth of self-assisted InAs nanowires on Si(111). Nanoscale Res. Lett. **6** 516

[45] Azizur-Rahman K M and LaPierre R R 2015 Wavelength-selective absorptance in GaAs, InP and InAs nanowire arrays Nanotechnology **26** 295202

[46] Azizur-Rahman K M and LaPierre R R 2016 Optical design of a mid-wavelength infrared InSb nanowire photodetector Nanotechnology **27** 1–8

[47] Tomioka K and Fukui T 2014 Recent progress in integration of III–V nanowire transistors on Si substrate by selective-area growth J. Phys. D. Appl. Phys. **47** 394001

[48] Chia A C E and LaPierre R R 2011 Contact planarization of ensemble nanowires Nanotechnology **22** 245304

[49] LaPierre R R, Chia a. C E, Gibson S J, Haapamaki C M, Boulanger J, Yee R, Kuyanov P, Zhang J, Tajik N, Jewell N and Rahman K M a. 2013 III-V nanowire photovoltaics: Review of design for high efficiency Phys. status solidi - Rapid Res. Lett. **7** 815–30

[50] Law M, Goldberger J and Yang P 2004 Semiconductor Nanowires and Nanotubes Annu. Rev. Mater. Res. **34** 83–122

[51] Dahl M, Namazi L, Zamani R R and Dick K A 2018 Sb Incorporation in Wurtzite and Zinc Blende InAs1−xSbxBranches on InAs Template Nanowires Small **14** 1–12

[52] Dubois S, Palais O, Pasquinelli M, Martinuzzi S and Jaussaud C 2006

Influence of substitutional metallic impurities on the performances of p-type crystalline silicon solar cells: The case of gold J. Appl. Phys. **100** 123502

[53] Sui M, Li M-Y, Kim E-S and Lee J 2013 Annealing temperature effect on self-assembled Au droplets on Si (111). Nanoscale Res. Lett. **8** 525

[54] Joyce H J, Wong-Leung J, Gao Q, Hoe Tan H and Jagadish C 2010 Phase perfection in zinc blende and wurtzite III- V nanowires using basic growth parameters Nano Lett. **10** 908–15

[55] Dick K A, Caroff P, Bolinsson J, Messing M E, Johansson J, Deppert K, Wallenberg L R and Samuelson L 2010 Control of III–V nanowire crystal structure by growth parameter tuning Semicond. Sci. Technol. **25** 024009

[56] Yamashita T, Sano K, Akiyama T, Nakamura K and Ito T 2008 Theoretical investigations on the formation of wurtzite segments in group III-V semiconductor nanowires Appl. Surf. Sci. **254** 7668–71

[57] Bao J, Bell D C, Capasso F, Wagner J B, Mårtensson T, Trägårdh J, Samuelson L, Bao J, Bell D C, Capasso F, Wagner J B, Mårtensson T, Trägårdh J and Samuelson L 2008 Optical Properties of Rotationally Twinned Nanowire Superlattices Nano Lett. **8** 836–41

[58] Thelander C, Caroff P, Plissard S, Dey A W and Dick K A 2011 Effects of crystal phase mixing on the electrical properties of InAs nanowires Nano Lett. **11** 2424–9

[59] Russo-Averchi E, Heiss M, Michelet L, Krogstrup P, Nygard J, Magen C, Morante J R, Uccelli E, Arbiol J and Fontcuberta i Morral a 2012 Suppression of three dimensional twinning for a 100% yield of vertical GaAs nanowires on silicon. Nanoscale **4** 1486–90

[60] Fortuna S a and Li X 2010 Metal-catalyzed semiconductor nanowires: a review on the control of growth directions Semicond. Sci. Technol. **25** 024005

[61] Glas F 2006 Critical dimensions for the plastic relaxation of strained axial heterostructures in free-standing nanowires Phys. Rev. B - Condens. Matter Mater. Phys. **74** 2–5

[62] Gorji Ghalamestani S, Ek M, Ganjipour B, Thelander C, Johansson J, Caroff P and Dick K a. 2012 Demonstration of defect-free and composition tunable Ga xIn 1-xSb nanowires Nano Lett. **12** 4914–9

[63] Potts H, Friedl M, Amaduzzi F, Tang K, Tütüncüoglu G, Matteini F, Alarcon Lladó E, McIntyre P C and Fontcuberta I Morral A 2016 From Twinning to Pure Zincblende Catalyst-Free InAs(Sb) Nanowires Nano Lett. **16** 637–43

[64] Bastiman F, Küpers H, Somaschini C and Geelhaar L 2016 Growth map for Ga-assisted growth of GaAs nanowires on Si(111) substrates by molecular beam epitaxy Nanotechnology **27** 095601

[65] Uccelli E, Arbiol J, Magen C, Krogstrup P, Russo-Averchi E, Heiss M, Mugny G, Morier-Genoud F, Nygård J, Morante J R and Fontcuberta I Morral A 2011 Three-dimensional multiple-order twinning of self-catalyzed GaAs nanowires on Si substrates Nano Lett. **11** 3827–32

[66] Li T, Gao L, Lei W, Guo L, Pan H, Yang T, Chen Y and Wang Z 2013 InAs-mediated growth of vertical InSb nanowires on Si substrates. Nanoscale Res. Lett. **8** 333

[67] Ghalamestani S G, Johansson S, Borg B M, Dick K a. and Wernersson L-E 2012 Highly controlled InAs nanowires on Si(111) wafers by MOVPE Phys. Status Solidi **9** 206–9

[68] Biermanns A, Dimakis E, Davydok A, Sasaki T, Geelhaar L, Takahasi M and Pietsch U 2014 Role of Liquid Indium in the Structural Purity of Wurtzite InAs Nanowires That Grow on Si(111). Nano Lett. **14** 6878–83

[69] Haapamaki C M, Baugh J and LaPierre R R 2012 Critical shell thickness for InAs-Al x In 1− x As(P) core-shell nanowires J. Appl. Phys. **112** 124305

[70] Lisak A and Fitzner K 1994 Vapor pressure measurements of arsenic and arsenic trioxide over condensed phases J. Phase Equilibria **15** 151–4

[71] Rosenblatt G M and Ernest Birchenall C 1961 Vapor pressure of antimony by the torsion-effusion method J. Chem. Phys. **35** 788–94

[72] Copel M, Reuter M C, Horn von Hoegen M and Tromp R M 1990 Influence of surfactants in Ge and Si epitaxy on Si(001) Phys. Rev. B **42** 11682–9

[73] Portavoce A, Berbezier I and Ronda A 2003 Effect of Sb on Si/Si and Ge/Si growth process Mater. Sci. Eng. B Solid-State Mater. Adv. Technol. **101** 181–5

[74] Anttu N and Xu H Q 2010 Coupling of light into nanowire arrays and subsequent absorption J. Nanosci. Nanotechnol. **10** 7183–7

[75] Wu P M, Anttu N, Xu H Q, Samuelson L and Pistol M-E 2012 Colorful InAs Nanowire Arrays: From Strong to Weak Absorption with Geometrical Tuning Nano Lett. **12** 1990–5

[76] Park H, Dan Y, Seo K, Yu Y J, Duane P K, Wober M and Crozier K B 2014 Filter-free image sensor pixels comprising silicon nanowires with selective color absorption Nano Lett. **14** 1804–9

[77] Park H and Crozier K B 2013 Multispectral imaging with vertical silicon nanowires Sci. Rep. **3** 1–6

[78] Anttu N and Xu H Q 2013 Efficient light management in vertical nanowire arrays for photovoltaics Opt. Express **21** A558

[79] Wang B and Leu P W 2012 Tunable and selective resonant absorption in vertical nanowires Opt. Lett. **37** 3756

[80] Azizur-Rahman K M 2016 Simulation of III-V Nanowires for Infrared Photodetection (McMaster University)

[81] Mahlke S, Rösler D, Seifert K, Krems J F and Thüring M 2007 Evaluation of Six Night Vision Enhancement Systems: Qualitative and Quantitative Support for Intelligent Image Processing Hum. Factors J. Hum. Factors Ergon. Soc. **49** 518–31

[82] Rogalski A, Antoszewski J and Faraone L 2009 Third-generation infrared photodetector arrays J. Appl. Phys. **105** 1–44

[83] Martyniuk P, Antoszewski J, Martyniuk M, Faraone L and Rogalski A 2014 New concepts in infrared photodetector designs Appl. Phys. Rev. **1** 041102

[84] Piotrowski J, Brzozowski P and Jozwikowski K 2003 Stacked multijunction photodetectors of long-wavelength radiation J. Electron. Mater. **32** 672–6

[85] Kimukin I, Biyikli N, Kartaloğlu T, Aytür O and Ozbay E 2004 High-Speed InSb photodetectors on GaAs for mid-IR applications IEEE J. Sel. Top. Quantum Electron. **10** 766–70

[86] Rogalski A 2005 HgCdTe infrared detector material: history, status and outlook Reports Prog. Phys. **68** 2267–336

[87] Mori M, Fujimoto N, Akae N, Uotani K, Tambo T and Tatsuyama C 2006 Heteroepitaxy of InSb films grown on a Si(001) substrate with AlSb buffer layer J. Cryst. Growth **286** 218–22

[88] Kim Y H, Lee J Y, Noh Y G, Kim M D, Kwon Y J, Oh J E and Gronsky R 2006 Effect of two-step growth on the heteroepitaxial growth of InSb thin film on Si (001) substrate: A transmission electron microscopy study Appl. Phys. Lett. **89** 1–4

[89] Mori M, Murata K, Fujimoto N, Tatsuyama C and Tambo T 2007 Effect of AlSb buffer layer thickness on heteroepitaxial growth of InSb films on a Si(001) substrate Thin Solid Films **515** 7861–5

[90] Rogalski A, Martyniuk P and Kopytko M 2016 Challenges of small-pixel infrared detectors: a review Reports Prog. Phys. **79** 046501

[91] Soci C, Zhang A, Bao X-Y, Kim H, Lo Y and Wang D 2010 Nanowire Photodetectors J. Nanosci. Nanotechnol. **10** 1430–49

[92] Wook Shin H, Jun Lee S, Gun Kim D, Bae M-H, Heo J, Jin Choi K, Jun Choi

W, Choe J and Cheol Shin J 2015 Short-wavelength infrared photodetector on Si employing strain-induced growth of very tall InAs nanowire arrays Sci. Rep. **5** 10764

[93] Kuo C-H, Wu J-M, Lin S-J and Chang W-C 2013 High sensitivity of middle-wavelength infrared photodetectors based on an individual InSb nanowire. Nanoscale Res. Lett. **8** 327

[94] Anyebe E A and Zhuang Q 2014 Self-catalysed InAs1-xSbx nanowires grown directly on bare Si substrates Mater. Res. Bull. **60** 572–5

[95] Sourribes M J L, Isakov I, Panfilova M, Liu H and Warburton P A 2014 Mobility enhancement by Sb-mediated minimisation of stacking fault density in InAs nanowires grown on silicon Nano Lett. **14** 1643–50

[96] Du W, Yang X, Pan H, Wang X, Ji H, Luo S, Ji X, Wang Z and Yang T 2015 Two Different Growth Mechanisms for Au-Free InAsSb Nanowires Growth on Si Substrate Cryst. Growth Des. **15** 2413–8

[97] Ercolani D, Gemmi M, Nasi L, Rossi F, Pea M, Li A, Salviati G, Beltram F and Sorba L 2012 Growth of InAs/InAsSb heterostructured nanowires Nanotechnology **23** 115606

[98] Thelander C, Caroff P, Plissard S and Dick K a. 2012 Electrical properties of InAs1−xSbx and InSb nanowires grown by molecular beam epitaxy Appl. Phys. Lett. **100** 232105

[99] Svensson J, Anttu N, Vainorius N, Borg B M and Wernersson L-E E 2013 Diameter-Dependent Photocurrent in InAsSb Nanowire Infrared Photodetectors Nano Lett. **13** 1380–5

[100] Thompson M D, Alhodaib A, Craig A P, Robson A, Aziz A, Krier A, Svensson J, Wernersson L, Sanchez A M and Marshall A R J 2016 Low Leakage-Current InAsSb Nanowire Photodetectors on Silicon Nano Lett. **16** 182–7

[101] Robson M T and LaPierre R R 2016 InAs nanowire growth modes on Si (111) by gas source molecular beam epitaxy J. Cryst. Growth **436** 1–11

[102] Robson M T, Dubrovskii V G and LaPierre R R 2015 Conditions for high yield of selective-area epitaxy InAs nanowires on SiO x /Si(111) substrates Nanotechnology **26** 465301

[103] Robson M, Azizur-Rahman K M, Parent D, Wojdylo P, Thompson D A and LaPierre R R 2017 Multispectral absorptance from large-diameter InAsSb nanowire arrays in a single epitaxial growth on silicon Nano Futur. **1** 035001

[104] Williams D B and Carter C B 2009 Transmission Electron Microscopy (New York: Springer Science)

[105] Bogner A, Jouneau P H, Thollet G, Basset D and Gauthier C 2007 A history of scanning electron microscopy developments: Towards "wet-STEM" imaging Micron **38** 390–401

[106] Postek M T, Vladár A E and Purushotham K P 2014 Does your SEM really tell the truth? How would you know? Part 2 Scanning **36** 347–55

[107] Saarbrücken D- An Elementary Introduction to Atomic Force Microscopy and Related Methods (U . Hartmann Institute of Experimental Physics)

[108] Gadelmawla E S, Koura M M, Maksoud T M A, Elewa I M and Soliman H H 2002 Roughness parameters **123** 133–45

[109] Sardela M 2014 Practical Materials Characterization (New York: Springer)

[110] Tullin C J The Theory Behind FTIR analysis

[111] Amaduzzi F 2017 Functional Properties of III-V nanowires addressed by Raman Spectroscopy (ÉCOLE POLYTECHNIQUE FÉDÉRALE DE LAUSANNE)

[112] Viana C E, da Silva a N R, Morimoto N I and Bonnaud O 2001 Analysis of SiO2 thin films deposited by PECVD using an oxygen-TEOS-argon mixture Brazilian J. Phys. **31** 299–303

[113] Jugessur A S, Yagnyukova M and Aitchison J S 2011 Nanofabrication of photonic crystal-based devices using electron beam spot lithography J. Vac. Sci. Technol. B, Nanotechnol. Microelectron. Mater. Process. Meas. Phenom. **29** 06FF06

[114] Layadi N, Colonell J I and Lee J T-C 1999 An introduction to plasma etching for VLSI circuit technology Bell Labs Tech. J. **4** 155–71

[115] Zhang D and Kushner M J 2001 Investigations of surface reactions during C2F6 plasma etching of SiO2 with equipment and feature scale models J. Vac. Sci. Technol. A Vacuum, Surfaces, Film. **19** 524–38

[116] Hedlund C, Blom H -O. and Berg S 1994 Microloading effect in reactive ion etching J. Vac. Sci. Technol. A Vacuum, Surfaces, Film. **12** 1962–5

[117] Sunada T, Yasaka T, Kumagai Y, Fujii K, Konishi T and Uesugi K 1991 Chemical Stability of HF-Treated Si (111) Surfaces Jpn. J. Appl. Phys. **30** 3567–9

[118] Chemical D 2008 Processing Procedures for CYCLOTENE 3000 Series Dry Etch Resins

[119] Chinoy P B 1997 Reactive ion etching of benzocyclobutene polymer films IEEE Trans. Components, Packag. Manuf. Technol. Part C **20** 199–206

[120] Zhang J 2014 ELECTRICAL AND OPTICAL CHARACTERIZATION OF GaAs NANOWIRE ARRAYS (McMaster University)

[121] Kim G S and Steinbrüchel C 2006 Plasma etching of benzocyclobutene in CF4⁄O2 and SF6⁄O2 plasmas J. Vac. Sci. Technol. A Vacuum, Surfaces, Film. **24** 424–30

[122] Oehrlein G S 1990 Study of sidewall passivation and microscopic silicon roughness phenomena in chlorine-based reactive ion etching of silicon trenches J. Vac. Sci. Technol. B Microelectron. Nanom. Struct. **8** 1199

[123] Matsuo P J 1997 Role of N2 addition on CF4/O2 Remote Plasma Chemical Dry Etching of Polycrystalline Silicon J. Vac. Sci. Technol. A **15** 1801

[124] Ghosh D S, Martinez L, Giurgola S, Vergani P and Pruneri V 2009 Widely transparent electrodes based on ultrathin metals Opt. Lett. **34** 325

[125] Schier M 1995 Reactive Ion Etching of Benzocyclobutene Using a Silicon Nitride Dielectric Etch Mask J. Electrochem. Soc. **142** 3238

[126] Mischke H, Gruetzner G and Shaw M 2003 Plasma etching of polymers like SU8 and BCB Proceedings of SPIE vol 4979, ed J A Yasaitis, M A Perez-Maher and J M Karam p 372

[127] Wei W, Bao X Y, Soci C, Ding Y, Wang Z L and Wang D 2009 Direct heteroepitaxy of vertical InAs nanowires on si substrates for broad band photovoltaics and photodetection Nano Lett. **9** 2926–34

[128] Tomioka K and Fukui T 2011 Tunnel field-effect transistor using InAs nanowire/Si heterojunction Appl. Phys. Lett. **98** 083114

[129] Kavanagh K L 2010 Misfit dislocations in nanowire heterostructures Semicond. Sci. Technol. **25** 024006

[130] Khmissi H, Naji K, Hadj Alouane M H, Chauvin N, Bru-Chevallier C, Ilahi B, Patriarche G and Gendry M 2012 InAs/InP nanowires grown by catalyst assisted molecular beam epitaxy on silicon substrates J. Cryst. Growth **344** 45–50

[131] Zhang Z, Lu Z Y, Chen P P, Xu H Y, Guo Y N, Liao Z M, Shi S X, Lu W and Zou J 2013 Quality of epitaxial InAs nanowires controlled by catalyst size in molecular beam epitaxy Appl. Phys. Lett. **103** 073109

[132] Tchernycheva M, Travers L, Patriarche G, Glas F, Harmand J C, Cirlin G E and Dubrovskii V G 2007 Au-assisted molecular beam epitaxy of InAs nanowires: Growth and theoretical analysis J. Appl. Phys. **102** 094313

[133] Dick K A, Deppert K, Karlsson L S, Wallenberg L R, Samuelson L and Seifert W 2005 A new understanding of au-assisted growth of III-V semiconductor nanowires Adv. Funct. Mater. **15** 1603–10

[134] Bar-Sadan M, Barthel J, Shtrikman H and Houben L 2012 Direct imaging of single Au atoms within GaAs nanowires Nano Lett. **12** 2352–6

[135] Breuer S, Pfüller C, Flissikowski T, Brandt O, Grahn H T, Geelhaar L and Riechert H 2011 Suitability of Au- and self-assisted GaAs nanowires for optoelectronic applications Nano Lett. **11** 1276–9

[136] Forbes D, Hubbard S, Raffaelle R and McNatt J S 2010 Au-catalyst-free epitaxy of InAs nanowires J. Cryst. Growth **312** 1391–5

[137] Grap T, Rieger T, Blömers C, Schäpers T, Grützmacher D and Lepsa M I 2013 Self-catalyzed VLS grown InAs nanowires with twinning superlattices. Nanotechnology **24** 335601

[138] Koblmüller G, Hertenberger S, Vizbaras K, Bichler M, Bao F, Zhang J-P and Abstreiter G 2010 Self-induced growth of vertical free-standing InAs nanowires on Si(111) by molecular beam epitaxy. Nanotechnology **21** 365602

[139] Zhang G, Sasaki S, Tateno K, Gotoh H and Sogawa T 2013 Au-free InAs nanowires grown in In-particle-assisted vapor-liquid-solid mode: Growth, structure, and electrical property AIP Adv. **3** 0–12

[140] Zhang G, Tateno K, Birowosuto M D, Notomi M, Sogawa T and Gotoh H 2015 Controlled 1.1–1.6 μm luminescence in gold-free multi-stacked InAs/InP heterostructure nanowires Nanotechnology **26** 115704

[141] Ikejiri K, Noborisaka J, Hara S, Motohisa J and Fukui T 2007 Mechanism of catalyst-free growth of GaAs nanowires by selective area MOVPE J. Cryst. Growth **298** 616–9

[142] Hertenberger S, Rudolph D, Bolte S, Döblinger M, Bichler M, Spirkoska D, Finley J J, Abstreiter G and Koblmüller G 2011 Absence of vapor-liquid-solid growth during molecular beam epitaxy of self-induced InAs nanowires on Si Appl. Phys. Lett. **98** 123114

[143] Mandl B, Dey A W, Stangl J, Cantoro M, Wernersson L E, Bauer G, Samuelson L, Deppert K and Thelander C 2011 Self-seeded, position-controlled InAs nanowire growth on Si: A growth parameter study J. Cryst. Growth **334** 51–6

[144] Mårtensson T, Wagner J B, Hilner E, Mikkelsen A, Thelander C, Stangl J, Ohlsson B J, Gustafsson A, Lundgren E, Samuelson L and Seifert W 2007 Epitaxial growth of indium arsenide nanowires on silicon using nucleation templates formed by self-assembled organic coatings Adv. Mater. **19** 1801–6

[145] Sartel C, Dheeraj D L, Jabeen F and Harmand J C 2010 Effect of arsenic species on the kinetics of GaAs nanowires growth by molecular beam epitaxy J. Cryst. Growth **312** 2073–7

[146] Björk M T, Schmid H, Breslin C M, Gignac L and Riel H 2012 InAs nanowire

growth on oxide-masked 〈111〉 silicon J. Cryst. Growth **344** 31–7

[147] Dubrovskii V G, Cirlin G E and Ustinov V M 2009 Semiconductor nanowhiskers: Synthesis, properties, and applications Semiconductors **43** 1539–84

[148] Kalache B, Roca i Cabarrocas P and Fontcuberta i Morral A 2006 Observation of incubation times in the nucleation of silicon nanowires obtained by the vapor-liquid-solid method Japanese J. Appl. Physics, Part 2 Lett. **45** 190–3

[149] Plante M C and Lapierre R R 2008 Control of GaAs nanowire morphology and crystal structure. Nanotechnology **19** 495603

[150] Jung K, Mohseni P K and Li X 2014 Ultrathin InAs nanowire growth by spontaneous Au nanoparticle spreading on indium-rich surfaces Nanoscale **6** 15293–300

[151] Cirlin G E, Dubrovskii V G, Soshnikov I P, Sibirev N V., Samsonenko Y B, Bouravleuv a. D, Harmand J C and Glas F 2009 Critical diameters and temperature domains for MBE growth of III-V nanowires on lattice mismatched substrates Phys. status solidi - Rapid Res. Lett. **3** 112–4

[152] Sun M H, Leong E S P, Chin a H, Ning C Z, Cirlin G E, Samsonenko Y B, Dubrovskii V G, Chuang L and Chang-Hasnain C 2010 Photoluminescence properties of InAs nanowires grown on GaAs and Si substrates. Nanotechnology **21** 335705

[153] Babu J B and Yoh K 2011 Effect of As/In-flux on the growth of InAs nanowire by molecular beam epitaxy J. Cryst. Growth **323** 301–3

[154] Krogstrup P, Scheu C, Sørensen C B, Nyg J, Madsen M H, Krogstrup P, Johnson E, Venkatesan S, Mühlbauer E, Scheu C, Sørensen C B and Nygård J 2013 Experimental determination of adatom diffusion lengths for growth of InAs nanowires J. Cryst. Growth **364** 16–22

[155] Zhang Z, Lu Z, Xu H, Chen P, Lu W and Zou J 2014 Structure and quality controlled growth of InAs nanowires through catalyst engineering Nano Res. **7** 1640–9

[156] Hertenberger S, Rudolph D, Becker J, Bichler M, Finley J J, Abstreiter G and Koblmüller G 2012 Rate-limiting mechanisms in high-temperature growth of catalyst-free InAs nanowires with large thermal stability Nanotechnology **23** 235602

[157] Tomioka K, Tanaka T, Hara S, Hiruma K and Fukui T 2011 III-V nanowires on Si substrate: Selective-area growth and device applications IEEE J. Sel. Top. Quantum Electron. **17** 1112–29

[158] Dick K a, Caroff P, Bolinsson J, Messing M E, Johansson J, Deppert K, Wallenberg L R and Samuelson L 2010 Control of III–V nanowire crystal structure by growth parameter tuning Semicond. Sci. Technol. **25** 024009

[159] VJ L, Oh J, Nayak A P, Katzenmeyer A M, Gilchrist K H, Grego S, Kobayashi N P, Wang S-Y, Talin a A, Dhar N K and Islam M S 2011 A Perspective on Nanowire Photodetectors: Current Status, Future Challenges, and Opportunities IEEE J. Sel. Top. Quantum Electron. **17** 1002–32

[160] Bauer B, Rudolph A, Soda M, Fontcuberta i Morral A, Zweck J, Schuh D and Reiger E 2010 Position controlled self-catalyzed growth of GaAs nanowires by molecular beam epitaxy Nanotechnology **21** 435601

[161] Munshi a M, Dheeraj D L, Fauske V T, Kim D C, Huh J, Reinertsen J F, Ahtapodov L, Lee K D, Heidari B, van Helvoort a T J, Fimland B O and Weman H 2014 Position-controlled uniform GaAs nanowires on silicon using nanoimprint lithography. Nano Lett. **14** 960–6

[162] Matteini F, Dubrovskii V G, Rüffer D, Tütüncüoğlu G, Fontana Y and Morral A F I 2015 Tailoring the diameter and density of self-catalyzed GaAs nanowires on silicon Nanotechnology **26** 105603

[163] Fontcuberta i Morral A, Colombo C, Abstreiter G, Arbiol J and Morante J R 2008 Nucleation mechanism of gallium-assisted molecular beam epitaxy growth of gallium arsenide nanowires Appl. Phys. Lett. **92** 063112

[164] Plissard S, Dick K A, Larrieu G, Godey S, Addad A, Wallart X and Caroff P 2010 Gold-free growth of GaAs nanowires on silicon: arrays and polytypism Nanotechnology **21** 385602

[165] Consonni V, Knelangen M, Geelhaar L, Trampert A and Riechert H 2010 Nucleation mechanisms of epitaxial GaN nanowires: Origin of their self-induced formation and initial radius Phys. Rev. B - Condens. Matter Mater. Phys. **81** 1–10

[166] Dubrovskii V G, Consonni V, Trampert A, Geelhaar L and Riechert H 2012 Scaling thermodynamic model for the self-induced nucleation of GaN nanowires Phys. Rev. B - Condens. Matter Mater. Phys. **85** 1–6

[167] Dubrovskii V G, Consonni V, Geelhaar L, Trampert A and Riechert H 2012 Scaling growth kinetics of self-induced GaN nanowires Appl. Phys. Lett. **100** 153101

[168] Consonni V, Dubrovskii V G, Trampert A, Geelhaar L and Riechert H 2012 Quantitative description for the growth rate of self-induced GaN nanowires Phys. Rev. B - Condens. Matter Mater. Phys. **85** 1–7

[169] Gao Q, Saxena D, Wang F, Fu L, Mokkapati S, Guo Y, Li L, Wong-Leung J, Caroff P, Tan H H and Jagadish C 2014 Selective-Area Epitaxy of Pure

Wurtzite InP Nanowires: High Quantum Efficiency and Room-Temperature Lasing. Nano Lett. **14** 5206–11

[170] Priante G, Ambrosini S, Dubrovskii V G, Franciosi a. and Rubini S 2013 Stopping and resuming at will the growth of GaAs nanowires Cryst. Growth Des. **13** 3976–84

[171] Dubrovskii V G 2014 Influence of the group V element on the chemical potential and crystal structure of Au-catalyzed III-V nanowires Appl. Phys. Lett. **104** 053110

[172] Glas F, Ramdani M R, Patriarche G and Harmand J-C C 2013 Predictive modeling of self-catalyzed III-V nanowire growth Phys. Rev. B **88** 195304

[173] Jasper J J 1972 The Surface Tension of Pure Liquid Compounds J. Phys. Chem. Ref. Data **1** 841

[174] Dubrovskii V G 2014 Nucleation Theory and Growth of Nanostructures (Heidelberg - New York - Dordrecht - London: Springer)

[175] Shen X-Q, Kishimoto D and Nishinaga T 1994 Arsenic Pressure Dependence of Surface Diffusion of Ga on Nonplanar GaAs Substrates Jpn. J. Appl. Phys. **33** 11–7

[176] Ikejiri K, Sato T, Yoshida H, Hiruma K, Motohisa J, Hara S and Fukui T 2008 Growth characteristics of GaAs nanowires obtained by selective area metal–organic vapour-phase epitaxy Nanotechnology **19** 265604

[177] Rogalski A 2009 Infrared Detectors for the Future Acta Phys. Pol. A **116** 389–406

[178] Paskov P 1997 Refractive indices of InSb, InAs, GaSb, InAs[x]Sb[1-x], and In[1-x]Ga[x]Sb: Effects of free carriers J. Appl. Phys. **81** 1890–8

[179] Stringfellow G B and Greene P E 1971 Liquid Phase Epitaxial Growth of InAs[sub 1−x] Sb[sub x] J. Electrochem. Soc. **118** 805–10

[180] Palik E D 1985 Handbook of Optical Constants of Solids (Washington: Academic Press, INC.)

[181] Anyebe E A, Rajpalke M K, Veal T D, Jin C J, Wang Z M and Zhuang Q D 2015 Surfactant effect of antimony addition to the morphology of self-catalyzed InAs1−x Sb x nanowires Nano Res. **8** 1309–19

[182] Nimmatoori P, Zhang Q, Dickey E C and Redwing J M 2009 Suppression of the vapor–liquid–solid growth of silicon nanowires by antimony addition Nanotechnology **20** 025607

[183] Sanchez A M, Beltran A M, Beanland R, Ben T, Gass M H, de la Peña F, Walls M, Taboada A G, Ripalda J M and Molina S I 2010 Blocking of indium

incorporation by antimony in III–V-Sb nanostructures Nanotechnology **21** 145606

[184] Wilk A, Genty F, Fraisse B, Boissier G, Grech P, El Gazouli M, Christol P, Oswald J, Simecek T, Hulicius E and Joullié A 2001 MBE growth of InAs/InAsSb/AlAsSb structures for mid-infrared lasers J. Cryst. Growth **223** 341–8

[185] Hörmann N G, Zardo I, Hertenberger S, Funk S, Bolte S, Döblinger M, Koblmüller G and Abstreiter G 2011 Effects of stacking variations on the lattice dynamics of InAs nanowires Phys. Rev. B - Condens. Matter Mater. Phys. **84** 1–7

[186] Li T, Chen Y, Lei W, Zhou X, Luo S, Hu Y, Wang L, Yang T and Wang Z 2011 Effect of growth temperature on the morphology and phonon properties of InAs nanowires on Si substrates Nanoscale Res. Lett. **6** 1–7

[187] Science S 1992 Raman scattering in InAsSb alloys grown on GaAs by MBE Semicond. Sci. Technol. **7** 567–70

[188] Du W N, Yang X G, Wang X Y, Pan H Y, Ji H M, Luo S, Yang T and Wang Z G 2014 The self-seeded growth of InAsSb nanowires on silicon by metal-organic vapor phase epitaxy J. Cryst. Growth **396** 33–7

[189] Zhuang Q D, Anyebe E A, Chen R, Liu H, Sanchez A M, Rajpalke M K, Veal T D, Wang Z M, Huang Y Z and Sun H D 2015 Sb-Induced phase control of InAsSb nanowires grown by molecular beam epitaxy Nano Lett. **15** 1109–16

[190] Sköld N, Wagner J B, Karlsson G, Hernán T, Seifert W, Pistol M-E and Samuelson L 2006 Phase Segregation in AlInP Shells on GaAs Nanowires Nano Lett. **6** 2743–7

[191] Rudolph D, Funk S, Döblinger M, Morkötter S, Hertenberger S, Schweickert L, Becker J, Matich S, Bichler M, Spirkoska D, Zardo I, Finley J J, Abstreiter G and Koblmüller G 2013 Spontaneous alloy composition ordering in GaAs-AlGaAs core-shell nanowires Nano Lett. **13** 1522–7

[192] Heiss M, Fontana Y, Gustafsson A, Wüst G, Magen C, O'Regan D D, Luo J W, Ketterer B, Conesa-Boj S, Kuhlmann A V., Houel J, Russo-Averchi E, Morante J R, Cantoni M, Marzari N, Arbiol J, Zunger A, Warburton R J and Fontcuberta i Morral A 2013 Self-assembled quantum dots in a nanowire system for quantum photonics Nat. Mater. **12** 439–44

[193] Berg A, Yazdi S, Nowzari A, Storm K, Jain V, Vainorius N, Samuelson L, Wagner J B and Borgstrom M T 2016 Radial Nanowire Light-Emitting Diodes in the (AlxGa1-x)yIn1-yP Material System Nano Lett. **16** 656–62

[194] Potts H, Morgan N P, Tütüncüoglu G, Friedl M and Morral A F i 2017

Tuning growth direction of catalyst-free InAs(Sb) nanowires with indium droplets Nanotechnology **28** 054001

[195] Farrell A C, Lee W J, Senanayake P, Haddad M A, Prikhodko S V. and Huffaker D L 2015 High-Quality InAsSb Nanowires Grown by Catalyst-Free Selective-Area Metal-Organic Chemical Vapor Deposition Nano Lett. **15** 6614–9

[196] Khorasaninejad M, Abedzadeh N, Walia J, Patchett S and Saini S S 2012 Color matrix refractive index sensors using coupled vertical silicon nanowire arrays Nano Lett. **12** 4228–34

[197] Fountaine K T, Kendall C G and Atwater H A 2014 Near-unity broadband absorption designs for semiconducting nanowire arrays via localized radial mode excitation Opt. Express **22** A930

[198] Brandt R E, Mangan N M, Li J V., Lee Y S and Buonassisi T 2017 Determining interface properties limiting open-circuit voltage in heterojunction solar cells J. Appl. Phys. **121** 185301

[199] Alagha S, Zhao S, Mi Z, Watkins S P and Kavanagh K L 2018 Electrical characterization of Si/InN nanowire heterojunctions Semicond. Sci. Technol. **33** 015008

[200] Alagha S, Heedt S, Vakulov D, Mohammadbeigi F, Kumar E S, Schäpers T, Isheim D, Watkins S P and Kavanagh K L 2017 Electrical properties of lightly Ga-doped ZnO nanowires Semicond. Sci. Technol. **32** 125010

[201] Goktas N I, Fiordaliso E M and LaPierre R R 2018 Doping assessment in GaAs nanowires Nanotechnology **29** 234001

[202] Holloway G W, Song Y, Haapamaki C M, LaPierre R R and Baugh J 2013 Electron transport in InAs-InAlAs core-shell nanowires Appl. Phys. Lett. **102** 043115

[203] Zhang G, Sun W, Xu S, Zhao H, Su H and Wang H 2009 Inductively coupled plasma-reactive ion etching of InSb using CH[sub 4]∕H[sub 2]∕Ar plasma J. Vac. Sci. Technol. A Vacuum, Surfaces, Film. **27** 681

[204] Mori M, Akae N, Uotani K, Fujimoto N, Tambo T and Tatsuyama C 2003 Heteroepitaxial growth of InSb films on a Si(0 0 1) substrate via AlSb buffer layer Appl. Surf. Sci. **216** 569–74

[205] Vajargah S H, Couillard M, Cui K, Tavakoli S G, Robinson B, Kleiman R N, Preston J S and Botton G A 2011 Strain relief and AlSb buffer layer morphology in GaSb heteroepitaxial films grown on Si as revealed by high-angle annular dark-field scanning transmission electron microscopy Appl. Phys. Lett. **98** 082113

9 Appendix

9.1 VASE BCB Model

Figure 9.1 shows common parameters used when fitting a BCB layer in the VASE software CompleteEASE. Fits work well in the 400 – 800 nm wavelength range, producing an MSE as low as 10. Model accuracy was verified by measuring cross-sectional thickness in SEM.

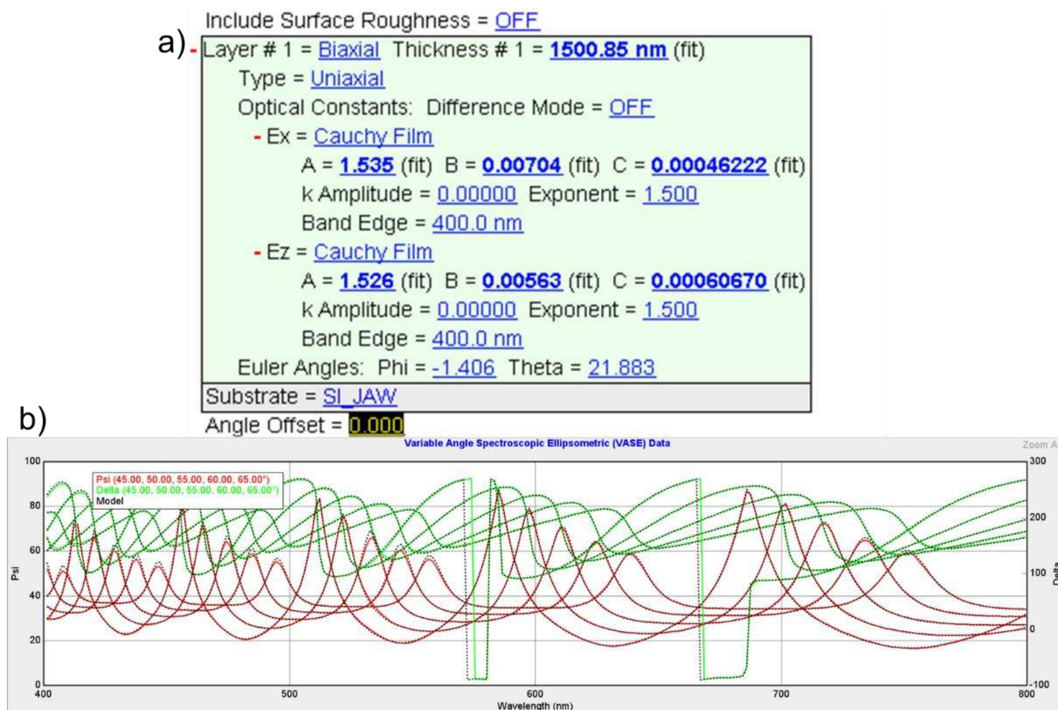

Figure 9.1: Nominal parameters for modeling BCB thickness in VASE. a) parameters for the biaxial Cauchy film and b) Psi and Delta for a thick (1.5 µm) BCB layer in the 400 – 800 nm wavelength range.

9.2 FF Calculations

FF calculations were performed to create a series of systematic FF variations in the MBE. The idea was to trickle a small amount of Sb into an

otherwise pure InAs growth since we had a strong understanding of InAs. We also wanted to maintain a constant V/III ratio since there is a growth rate dependence on V/III ratio. The V/III ratio was kept high (at 10) to maintain the highest verified growth rate. In order to maintain a constant V/III ratio, the flux of As needed to be decreased as the flux of Sb was increased. Also, conversion factors between atomic flux and the appropriate MBE-controlled parameter (BEP for Sb, flow rate for As) were needed for Python.

Beginning with As, we took the flow rate of As from a previous growth at a V/III ratio of 10 and converted to a Molar rate using the conversion for an ideal volume.

$$\mathrm{M_{As}} = \frac{1\ \mathrm{Mole}}{22.4\ \mathrm{L}} \times \mathrm{V_{As}} \qquad (9.1)$$

where $\mathrm{M_{As}}$ is the Molar rate and $\mathrm{V_{As}}$ is the flow rate of As in SCCM. Atomic flux is found by considering the geometries of our MBE system. If the atoms leaving the cracker orifice cover a hemisphere in space, then the atomic flux is given as

$$\mathrm{F_{As}} = \frac{\mathrm{M_{As}}}{\pi \mathrm{r}^2} \qquad (9.2)$$

where r is the distance between the cracker cell and the substrate (8 inches in our system). From these calculations, if a linear relationship between atomic flux and the flow rate of As is assumed, a conversion factor (β) was found.

$$\beta = \frac{\mathrm{F_{As}}}{\mathrm{V_{As}}} \qquad (9.3)$$

Similarly, a conversion factor (α) between BEP of Sb and atomic flux of Sb can be found using the known values of growth rate, BEP, and InSb film density of an InSb growth.

$$\alpha = \frac{F_{Sb}}{BEP_{Sb}} \qquad (9.4)$$

Armed with these two quick conversion factors, a python script was built to solve the following two equations for several values of FF.

$$F_{Sb} + F_{As} = \text{Constant} \qquad (9.5)$$

$$\frac{F_{Sb}}{F_{Sb} + F_{As}} = FF \qquad (9.6)$$

Equation 9.5 is the condition set at the start of the study where the atomic fluxes must always add up to the same constant in order to maintain a V/III ratio of 10. This constant was equal to the atomic flux of As in the pure InAs growth. Equation 9.6 is the definition of fractional flux and allowed us to input several values of FF for extracting atomic fluxes. Finally, the atomic fluxes were converted to BEP and flow rate for relevant MBE control. The python script and a plot of important MBE parameters for Sb and As (Figure 9.2) are included below.

```
1.  #assumptions:
2.  #   - using ideal gas conversion for Mole -> Litre
3.  #   - using Shahrams calculations for As2 flux with no adjustments
4.  #   - only works for constant GR of 0.125um/hr (ie constant In flux)
5.  #   - no re-evaporation of Sb upon contact with the substrate
6.  #   - all Sb incorporates into the film
7.  #   - starting BEP of Sb of 1.44E-7 torr for previous InSb growth (1724)
8.  #   - Half of the flux required to sustain the InSb film is Sb if V/III is 1
```

```
9.  #  - linear relationship between BEPsb and Fluxsb for this temp and GR
10. #  - using InSb atomic film density for BEP->
    flux conversion but using InAs film density for all other calcs including the InAsSb (ie Sb content lo
    w)
11.
12. #imports
13. import numpy as np
14. import matplotlib.pyplot as plt
15. import csv
16.
17. #constants
18. SCCM_As = 2.1 # found from Torr on growth records. Converted with shahrams chart V/III 10 = 2.1
    , 4 = 0.844, 2 = 0.413, 14 = 2.976
19. alpha = 3.542E20 # lots of units, used to convert Sb BEP to atomic flux in Sb/cm^2/s
20. SbMin = 7E-8  #torr, the min amount of Sb that we can trickle in (ish)
21. SbMax = 8.2E-
    7 #torr, not actually the maximum but the highest I've seen used (54% closed valve)
22.
23. #convert SCCM to As/cm2/s
24. Mf_As = (SCCM_As*1E-
    3/22.4*6.022E23/60.0)/1297.17 # flux of As in As/cm^2/s for a V/III ratio of 10
25.
26. #12" gives geo factor of 2918.63
27. #10" gives geo factor of 2026.82
28. #8" gives geo factor of 1297.17
29. #7" gives geo factor of 993.15
30.
31. beta =  Mf_As/SCCM_As# lots of units, used to convert As SCCM to atomic flux in As/cm^2/s
32. TargetV = Mf_As # flux of atoms to maintain a V/III ratio of 10
33.
34. # working range
35. FF = np.linspace(0,50,51) #in %, FFvalues as x values
36.
37. #model for values
38. Fsb = TargetV*FF/100.0 # use formula for FF to find values, convert FF to percent
39. BEPsb = Fsb/alpha # convert to BEP, account for sb2 flux
40. Fas = TargetV-Fsb # reduce the As flux to compensate for the antimony flux
41. Flowas = Fas/beta # convert to sccm
42.
43. with open ('FFdata.csv','w') as csvfile:
44.     someData = csv.writer(csvfile, delimiter=';')
45.     someData.writerow(np.transpose(FF))
46.     someData.writerow(np.transpose(BEPsb))
47.     someData.writerow(np.transpose(Flowas))
48.
49. print TargetV
50.
51.
52. #plot
53. fig = plt.figure()
54. fig.set_size_inches(12,8)
55. ax = fig.add_subplot(111)
56. ax.plot(FF,BEPsb, '-b')
57. ax2 = ax.twinx()
58. ax2.plot(FF, Flowas, '-r')
59.
60. ax.grid()
61. ax.set_xlabel("Fractional Flux (%)")
62. ax.set_ylabel(r"BEP of Anitmony (Torr)")
```

```
63. ax.ticklabel_format(style = 'sci', scilimits = (0,0), axis = 'y')
64. ax2.set_ylabel(r"Flow of Arsenic (SCCM)")
65. #ax2.set_ylim(0, 35)
66. #ax.set_ylim(-20,100)
67. plt.show()
68.
69. #fig.savefig('FF_modelSb.png', dpi = 600)
```

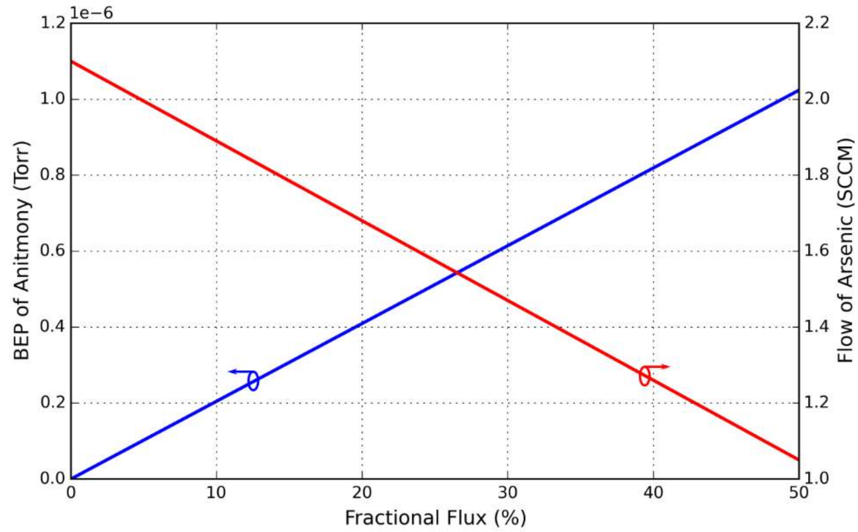

Figure 9.2: Plot of BEP and flow rate vs FF for extracting parameters for InAsSb growth in MBE.